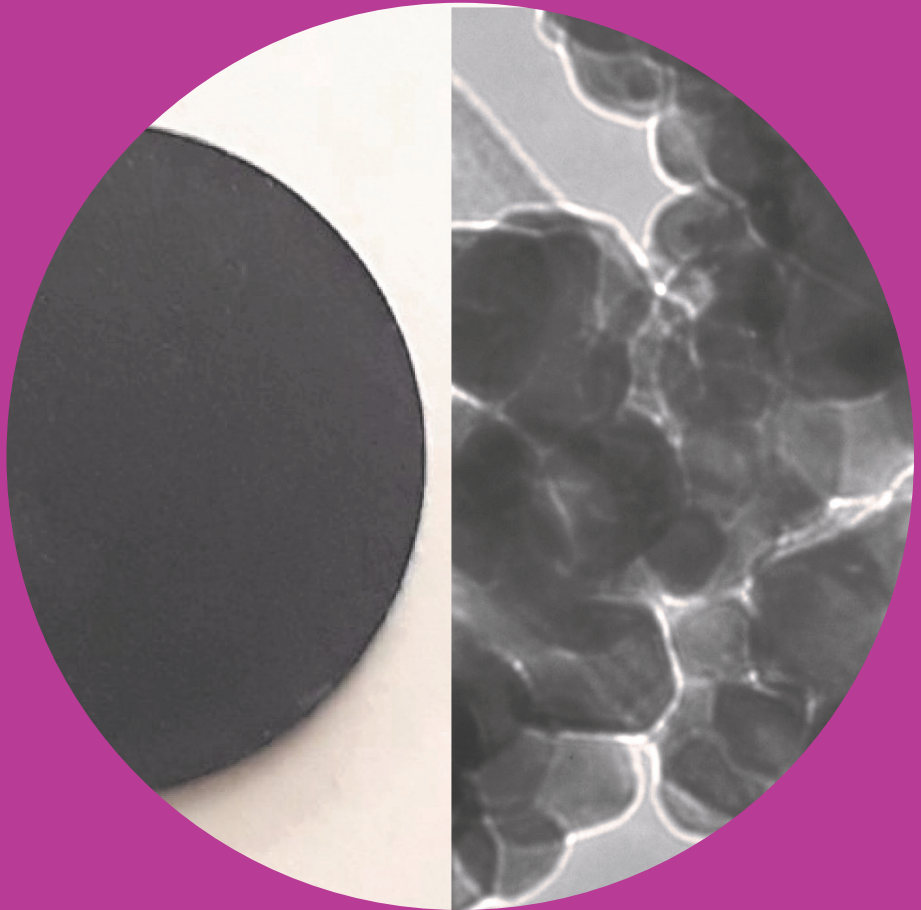


Analysis of single-layer and three-layer nanocomposite fuel cells

Sami Jouttijärvi



Analysis of single-layer and three-layer nanocomposite fuel cells

Sami Jouttijärvi

The public defense will be organized via remote technology.

Link: <https://aalto.zoom.us/j/729014568>

Zoom Quick Guide: <https://www.aalto.fi/en/services/zoom-quick-guide>

A doctoral dissertation completed for the degree of Doctor of Science (Technology) to be defended, with the permission of the Aalto University School of Science, at a public examination held at the lecture hall R008/216 of the school on 3 April 2020 at 12:00.

**Aalto University
School of Science
Department of Applied Physics
New Energy Technologies**

Supervising professor

Professor Peter D. Lund, Aalto University, Finland

Thesis advisor

Professor Muhammad Imran Asghar, Aalto University, Finland, Hubei University, China

Preliminary examiners

Professor Fernando Marques, University of Aveiro, Portugal

Dr. Olli Himanen, VTT, Finland

Opponent

Dr. Mikael Syväjärvi, Linköping University, Sweden

Aalto University publication series

DOCTORAL DISSERTATIONS 46/2020

© 2020 Sami Jouttijärvi

ISBN 978-952-60-3799-8 (printed)

ISBN 978-952-60-3800-1 (pdf)

ISSN 1799-4934 (printed)

ISSN 1799-4942 (pdf)

<http://urn.fi/URN:ISBN:978-952-60-3800-1>

Unigrafia Oy

Helsinki 2020

Finland



Printed matter
4041-0619

Author

Sami Jouttijärvi

Name of the doctoral dissertation

Analysis of single-layer and three-layer nanocomposite fuel cells

Publisher School of Science**Unit** Department of Applied Physics**Series** Aalto University publication series DOCTORAL DISSERTATIONS 46/2020**Field of research** Engineering Physics**Manuscript submitted** 14 February 2020**Date of the defence** 3 April 2020**Permission for public defence granted (date)** 27 February 2020**Language** English☐ **Monograph**☒ **Article dissertation**☐ **Essay dissertation****Abstract**

Fuel cells (FCs) convert the chemical energy of the fuel directly to electricity. FCs are potential candidates for clean electricity sources in the future, provided that the main challenges halting their commercialization can be solved. Several different FC subtypes exist. This Thesis is focused on ceramic nanocomposite FCs (CNFCs) and single-layer FCs (SLFCs). Both of these FCs operate at intermediate temperatures, at around 500-600 °C.

CNFC utilizes the traditional three-layer structure: anode, electrolyte, and cathode. The key component is the electrolyte, that consists of a composite of a solid oxide and a salt, here doped ceria and alkali carbonate mixture respectively. This composite electrolyte allows an efficient multi-ion conduction, reducing the ohmic losses in the cell. Excellent power densities, exceeding 1 W per square centimeter, were achieved with two different CNFCs in this Thesis.

SLFC is a ground-breaking innovation where all FC functions are compressed into one single layer, consisting of a mixture of a semiconductor (here lithium nickel zinc oxide or copper iron oxide) and an ionic conductor (here doped ceria or doped ceria – alkali carbonate mixture). The SLFC design allows to eliminate the challenges originating from the three-layer structure and to simplify the manufacturing procedure. In this Thesis, the working principle and performance-affecting factors of SLFCs were studied. The key findings include that the proton is dominating over the oxygen-ion in ionic conduction with the studied SLFC configuration and that applying the composite ionic conductor of CNFC to SLFC improves vastly the cell performance.

Since both CNFCs and SLFCs are complex nanoscale structures, studying the microstructure of these devices with electron microscopy and X-ray spectroscopy are identified as crucial procedures to understand the macroscopic output. Systematic studies combined with modern microscopic methods are suggested as a pathway to push both SLFCs and CNFCs towards commercialization.

Keywords Single-layer fuel cell, ceramic nanocomposite fuel cell, microscopic characterization**ISBN (printed)** 978-952-60-3799-8**ISBN (pdf)** 978-952-60-3800-1**ISSN (printed)** 1799-4934**ISSN (pdf)** 1799-4942**Location of publisher** Helsinki**Location of printing** Helsinki **Year** 2020**Pages** 182**urn** <http://urn.fi/URN:ISBN:978-952-60-3800-1>

Tekijä

Sami Jouttijärvi

Väitöskirjan nimi

Yksi- ja kolmikerroksisten nanokomposiittipolttokennojen analysointi

Julkaisija Perustieteiden korkeakoulu**Yksikkö** Teknillisen fysiikan laitos**Sarja** Aalto University publication series DOCTORAL DISSERTATIONS 46/2020**Tutkimusala** Teknillinen fysiikka**Käsikirjoituksen pvm** 14.02.2020**Väitöspäivä** 03.04.2020**Väittelyluvan myöntämispäivä** 27.02.2020**Kieli** Englanti☐ **Monografia**☒ **Artikkeliväitöskirja**☐ **Esseeväitöskirja****Tiivistelmä**

Polttokennot muuttavat polttoaineen kemiallisen energian suoraan sähköksi. Polttokennot ovat potentiaalisia ehdokkaita tulevaisuuden puhtaaseen sähköntuotantoon, mikäli niiden kaupallistamista rajoittavat keskeiset haasteet saadaan ratkaistua. Polttokennoja on useita eri tyyppisiä. Tämä väitöskirja käsittelee keraamisia nanokomposiittipolttokennoja (CNFC) ja yksikomponenttipolttokennoja (SLFC). Molemmat näistä operoivat keskialueen lämpötiloissa, noin 500-600 celsiusasteessa.

CNFC:t hyödyntävät perinteistä kolmikerroksista rakennetta: niissä on anodi, elektrolyytti ja katodi. Avainkomponentti on elektrolyytti, joka koostuu kiinteän oksidin ja suolan, tässä väitöskirjassa seostetun ceriumoksidin ja alkalikarbonaattiseoksen, muodostamasta komposiitista. Tällainen komposiittielektrolyytti mahdollistaa tehokkaan moni-ionijohtavuuden, mikä vähentää kennon ohmisia häviöitä. Erinomaiset tehotehdydet, yli 1 W neliösenttimetriä kohti, saavutettiin kahdella eri CNFC:llä tässä väitöskirjassa.

SLFC on uraauurtava innovaatio missä kaikki polttokennotoiminnot on tiivistetty yhteen kerrokseen, joka koostuu puolijohteen (tässä väitöskirjassa litium-nikkeli-sinkkioksidi tai kupari-rautaoksidi) ja ionijohteen (tässä väitöskirjassa seostettu ceriumoksidi tai seostettu ceriumoksidi – alkalikarbonaattisekoitus). SLFC:n rakenne eliminoi haasteet, jotka johtuvat kolmikerrosrakenteesta ja mahdollistaa valmistusmenetelmien yksinkertaistamisen. Tässä väitöskirjassa tutkittiin SLFC:n toimintaperiaatetta ja suorituskykyyn vaikuttavia tekijöitä. Avaintuloksiin sisältyy protonin dominointi happi-ionin suhteen ionijohtavuudessa tutkituissa SLFC-konfiguraatioissa sekä se, että CNFC:n komposiitti-ionijohteen soveltaminen SLFC:hen paransi huomattavasti suorituskykyä.

Koska sekä CNFC että SLFC ovat monimutkaisia nanotason rakenteita, niiden mikrorakenteen tutkiminen elektronimikroskopialla ja röntgensädespektroskopialla tunnistettiin kriittiseksi menetelmiksi makroskooppisen toiminnan ymmärtämiseksi. Systemaattisia tutkimuksia yhdistettynä moderneihin mikroskooppisiin metodeihin ehdotetaan keinoksi edistää sekä CNFC:n että SLFC:n kaupallistamista.

Avainsanat Yksikomponenttipolttokenno, keraaminen nanokomposiittipolttokenno, mikroskooppinen karakterisointi**ISBN (painettu)** 978-952-60-3799-8**ISBN (pdf)** 978-952-60-3800-1**ISSN (painettu)** 1799-4934**ISSN (pdf)** 1799-4942**Julkaisupaikka** Helsinki**Painopaikka** Helsinki**Vuosi** 2020**Sivumäärä** 182**urn** <http://urn.fi/URN:ISBN:978-952-60-3800-1>

Acknowledgements

This work was done in the New Energy Technologies research group at the Department of Applied Physics, Aalto University School of Science during 2016-2020, under supervision of Professor Peter D. Lund. The work was mainly funded by the Academy of Finland through grants No. 13282962, 13279204 and 13329016. The work utilized resources provided by OtaNano Nanomicroscopy Center.

While spending almost eight years as a member of the New Energy Technologies research group, from Bachelor's Thesis to Doctoral Dissertation, I have worked with many persons who are both brilliant researchers and kind colleagues. I would like to thank them all for their support, both in and out of office. Especially I would like to thank Professors Peter Lund and Imran Asghar, my Thesis supervisor and advisor respectively, for granting me the possibility to complete a Doctoral degree in this research group and for guiding me through the process during the past four years.

Of course, life requires content and activities outside work. For that, I would like to thank my family, other relatives and friends.

Thank you all.

Espoo, 3 March 2020
Sami Valtteri Jouttijärvi

Contents

Acknowledgements	i
List of Abbreviations and Symbols.....	v
List of Publications	ix
Author's Contribution	xi
1. Introduction	1
1.1 Overview	1
1.2 Objectives and scope.....	2
1.3 Structure of this Thesis	5
2. Fuel cells	6
2.1 Principle of fuel cells	6
2.2 Ceramic nanocomposite fuel cell	8
2.3 Single-layer fuel cell	10
3. Literature review.....	11
3.1 State-of-the-art of fuel cells.....	11
3.1.1 Ceramic nanocomposite fuel cell	11
3.1.2 Single-layer fuel cell	13
3.1.3 Summary.....	15
3.2 Microstructural analysis of fuel cells (Publication I, RQ1).....	15
3.2.1 X-ray diffraction spectroscopy	16
3.2.2 2D microscopy	17
3.2.3 3D microscopy	20
3.3 Challenges and gaps in fuel cell research	23
4. Materials and methods.....	25
4.1 Materials, synthesis and fuel cell manufacturing	25
4.1.1 Commercial chemicals	25
4.1.2 Material synthesis and mixing	25
4.1.3 Fuel cell fabrication.....	27
4.2 Characterization.....	28
4.2.1 Microstructural characterization	28

4.2.2	Electrochemical characterization	29
5.	Results	34
5.1	High-performance three-layer fuel cells with composite electrolyte (Publications II&III, RQ2).....	34
5.2	Single-layer fuel cells based on lithium nickel zinc oxide, copper iron oxide and doped ceria (Publications IV&V, RQ3).....	38
5.3	Factors affecting power output of LNZ-based single layer fuel cells (Publications VI&VII, RQ4)	42
6.	Discussion	51
6.1	Ceramic nanocomposite fuel cell	51
6.2	Single-layer fuel cell.....	52
6.3	Future of microstructural characterization of CNFCs and SLFCs 54	
6.4	Summary	55
7.	Conclusions	56
7.1	Recommendations for future work.....	57
	References	58

List of Abbreviations and Symbols

A note on Abbreviations

In this Thesis, Abbreviations are presented in a consistent and logical way. For example, all doped cerias are abbreviated with syntax 'ADC', where 'DC' stands for doped ceria and 'A' is the first letter of the chemical symbol of the dopant element (one for each if there are multiple dopant elements).

Special attention is paid to ensure that the same abbreviation is used for every abbreviated phrase throughout the Thesis. This is necessary to ensure the consistency and to improve the readability of this work. However, since some phrases are abbreviated in the literature in different ways, the abbreviations used in the compiling part of this Thesis may be different than the abbreviations used to represent the same phrases in the original works which are cited.

Abbreviations

AC	alternating current
AFC	alkaline fuel cell
BF	bright field
BSCF	barium strontium cobalt ferrite, $\text{Ba}_x\text{Sr}_{1-x}\text{Co}_y\text{Fe}_{1-y}\text{O}_{3-\delta}$
BSE	backscattered electron
CA	citric acid, $\text{CH}_2 - \text{COH} - \text{CH}_2$
CCB	copper carbonate basic, $\text{Cu}_2(\text{OH})_2\text{CO}_3$
CFO	copper iron oxide, CuFe_2O_4
CNFC	ceramic nanocomposite fuel cell
CNH	calcium nitrate hexahydrate, $\text{Ca}(\text{NO}_3)_2 \cdot 6\text{H}_2\text{O}$
CNT	cerium nitrate tetrahydrate, $\text{Ce}(\text{NO}_3)_3 \cdot 4\text{H}_2\text{O}$
CPE	constant phase element
CSDC	calcium-samarium co-doped ceria, $\text{Ca}_x\text{Sm}_y\text{Ce}_{1-x-y}\text{O}_{2-\delta}$
DC	direct current
DF	dark field
DRT	distribution of relaxation times
DSC	differential scanning calorimetry
EC	ethyl cellulose
EDX	energy-dispersive X-ray spectroscopy
EELS	electron energy loss spectroscopy
EFFC	electrolyte-free fuel cell
EIS	electrochemical impedance spectroscopy

FC	fuel cell
FIB	focused ion beam
GDC	gadolinium-doped cerium oxide, $Gd_xCe_{1-x}O_{2-\delta}$
GHG	greenhouse gas
GNH	gadolinium nitrate hexahydrate, $Gd(NO_3)_3 \cdot 6H_2O$
HT	high temperature
ICDD	International Crystalline Diffraction Database
IEA	International Energy agency
IPCC	Intergovernmental Panel on Climate Change
IP	current - power
IV	current - voltage
KAZ	potassium aluminium zinc oxide, $K_xAl_yZn_{1-x-y}O$
KC	potassium carbonate, K_2CO_3
KLC	potassium-lithium carbonate, $K_xLi_{2-x}CO_3$
LC	lithium carbonate, Li_2CO_3
LN	lithium nitrate, $LiNO_3$
LNCoS	lithium nickel cobalt strontium oxide, $Li_xNi_yCo_zSr_{1-x-y-z}O_{2-\delta}$
LNCS	lithium nickel copper strontium oxide, $Li_xNi_yCu_zSr_{1-x-y-z}O_{2-\delta}$
LNMS	lithium nickel manganese strontium oxide, $Li_xNi_yMn_zSr_{1-x-y-z}O_{2-\delta}$
LNCZ	lithium nickel copper zinc oxide, $Li_xNi_yCu_zZn_{1-x-y-z}O_{2-\delta}$
LNCZF	lithium nickel copper zinc iron oxide, $Li_xNi_yCu_zZn_aFe_{1-x-y-z-a}O_{2-\delta}$
LMZ	lithium magnesium zinc oxide, $Li_xMg_yZn_{1-x-y}O$
LNZ	lithium nickel zinc oxide, $Li_xNi_yZn_{1-x-y}O$
LPDC	lanthanum-praseodymium co-doped ceria, $La_xPr_yCe_{1-x-y}O_{2-\delta}$
LPNDC	lanthanum-praseodymium-neodymium co-doped ceria, $La_xPr_yNd_zCe_{1-x-y-z}O_{2-\delta}$
LSC	lanthanum strontium cobalt oxide, $La_xSr_{1-x}CoO_3$
LSCF	lanthanum strontium cobalt ferrite, $La_xSr_{1-x}Co_yFe_{1-y}O_{3-\delta}$
LSF	lanthanum strontium iron oxide, $La_xSr_{1-x}FeO_3$
LSGM	lanthanum strontium gadolinium magnesium oxide, $La_xSr_{1-x}Ga_yMg_{1-y}O_3$
LSM	lanthanum strontium manganese oxide, $La_xSr_{1-x}MnO_3$
MCFC	molten carbonate fuel cell
MZ	magnesium zinc oxide, $Mn_xZn_{1-x}O$
NC	sodium carbonate, Na_2CO_3
NCAL	lithium nickel cobalt aluminium oxide, $LiNi_xCo_yAl_{1-x-y}O_2$
NCBH	nickel carbonate basic hydrate, $NiCO_3 \cdot 2Ni(OH)_2 \cdot xH_2O$
NLC	sodium-lithium carbonate, $Na_xLi_{2-x}CO_3$
NLKC	sodium-lithium-potassium carbonate, $Na_xLi_yK_{2-x-y}CO_3$
NMC	nanomicroscopy center
NZ	nickel zinc oxide, $Ni_xZn_{1-x}O$
OC	open circuit
OCV	open circuit voltage
PAFC	phosphoric acid fuel cell
PE	primary electron
PEG	polyethylene glycol

PEMFC	polymer electrolyte membrane fuel cell, proton exchange membrane fuel cell
PSCFN	praseodymium strontium cobalt iron niobium oxide, $\text{Pr}_x\text{Sr}_{1-x}\text{Co}_y\text{Fe}_z\text{Nb}_{1-y-z}\text{O}_{3-\delta}$
PVA	polyvinyl alcohol
R	resistor
RPM	rounds per minute
RQ	research question
SC	short-circuit
SCFC	single-component fuel cell
SDC	samarium-doped cerium oxide, $\text{Sm}_x\text{Ce}_{1-x}\text{O}_{2-\delta}$
SE	secondary electron
SEM	scanning electron microscope, scanning electron microscopy
SNH	samarium nitrate hexahydrate, $\text{Sm}(\text{NO}_3)_3 \cdot 6\text{H}_2\text{O}$
SFM	strontium iron molybdenum oxide, $\text{Sr}_2\text{Fe}_x\text{Mo}_{2-x}\text{O}_{6-\delta}$
SSDC	strontium-samarium co-doped ceria, $\text{Sr}_x\text{Sm}_y\text{Ce}_{1-x-y}\text{O}_{2-\delta}$
SLFC	single-layer fuel cell
SOFC	solid oxide fuel cell
SSC	samarium strontium cobalt oxide, $\text{Sm}_x\text{Sr}_{1-x}\text{CoO}_3$
TEC	thermal expansion coefficient
TEM	transmission electron microscope, transmission electron microscopy
TPB	triple-phase boundary
TPES	total primary energy supply
VRE	variable renewable energy
XRD	X-ray diffraction spectroscopy
YGDC	yttria-gadolinium co-doped ceria, $\text{Y}_x\text{Gd}_y\text{Ce}_{1-x-y}\text{O}_{2-\delta}$
YSZ	yttria-stabilized zirconia, $\text{Y}_x\text{Zr}_{1-x}\text{O}_{2-\delta}$
ZCB	zinc carbonate basic, $(\text{ZnCO}_3)_2 \cdot (\text{Zn}(\text{OH})_2)_3$
ZNH	zinc nitrate hexahydrate, $\text{Zn}(\text{NO}_3)_2 \cdot 6\text{H}_2\text{O}$

Symbols

A	Ampere, area [m^2]
d	distance [m]
Hz	Hertz
I	current [A]
I_{SC}	short-circuit current [A]
L	inductance [H]
n	integer
P	power [W]
R	resistance [Ω]
T	temperature [K]
V	volt, voltage [V]
V_{AC}	alternating voltage [V]
V_{DC}	direct voltage [V]

V_{oc}	open circuit voltage [V]
W	watt
Wh	watt hour
Z	impedance [Ω]
λ	wavelength [m]
Ω	Ohm
θ	angle [$^\circ$]

Prefixes

T	tera, 10^{12}
G	giga, 10^9
M	mega, 10^6
k	kilo, 10^3
m	milli, 10^{-3}
μ	micro, 10^{-6}
n	nano, 10^{-9}

List of Publications

This doctoral dissertation consists of a compiling part and of the following publications which are referred to in the text by their Roman numerals.

I. Jouttijärvi, Sami; Asghar, Muhammad Imran; Lund, Peter D., Microscopic techniques for analysis of ceramic fuel cells, *WIREs Energy and Environment*, 7, e299 (2018), DOI: <https://doi.org/10.1002/wene.299>

II. Asghar, Muhammad Imran; Jouttijärvi, Sami; Jokiranta, Riina; Lund, Peter D., Remarkable ionic conductivity and catalytic activity in ceramic nano-composite fuel cells, *International Journal of Hydrogen Energy*, 43, 12892-12899 (2018), DOI: <https://doi.org/10.1016/j.ijhydene.2018.05.045>

III. Asghar, Muhammad Imran; Jouttijärvi, Sami; Lund, Peter D., High performance ceramic nanocomposite fuel cells utilizing LiNiCuZn-oxide anode based on slurry method, *International Journal of Hydrogen Energy*, 43, 12797-12802 (2018), DOI: <https://doi.org/10.1016/j.ijhydene.2018.03.232>

IV. Asghar, Muhammad Imran; Jouttijärvi, Sami; Jokiranta, Riina; Valtavirta, Anna-Maija; Lund, Peter D., Wide bandgap oxides for low-temperature single-layered nanocomposite fuel cell, *Nano Energy*, 53, 391-397 (2018), DOI: <https://doi.org/10.1016/j.nanoen.2018.08.070>

V. Asghar, Muhammad Imran; Yao, Xueli; Jouttijärvi, Sami; Hochreiner, Eli-onora; Virta, Riina; Lund, Peter D., Intriguing electrochemistry in low-temperature single layer ceramic fuel cells based on CuFe_2O_4 , *International Journal of Hydrogen Energy*, in press, published online 26 October 2019, 10 pages, DOI: <https://doi.org/10.1016/j.ijhydene.2019.09.175>

VI. Jouttijärvi, Sami; Yao, Xueli; Asghar, Muhammad Imran; Etula, Jarkko; Reinecke, A.-M.; Lippmann, W.; Lund, Peter D., Carbonate dual-phase improves the ionic conductivity and performance of mixed ionic and semiconductor single-layer fuel cell, revised version (second round) submitted to *BMC Energy* in December 2019, 24 pages¹.

VII. Jouttijärvi, Sami; Asghar, Muhammad Imran; Yao, Xueli; Lund, Peter D., Investigation of factors affecting the performance of a single-layer nanocomposite fuel cell, *Catalysis Today*, in press, published online 31 January 2020, 7 pages, DOI: <https://doi.org/10.1016/j.cattod.2020.01.048>

[†]The length of the manuscript in the format that was submitted for the journal and reprinted in this Thesis. The number of pages in the final form may differ significantly from the value shown here.

Author's Contribution

Publication I: Microscopic techniques for analysis of ceramic fuel cells

The author collected and analyzed the references, organized the structure of the Publication and had the lead role in the writing process.

Publication II: Remarkable ionic conductivity and catalytic activity in ceramic nanocomposite fuel cells

The author participated on cell manufacturing, characterization, data analysis and writing the Publication.

Publication III: High performance ceramic nanocomposite fuel cells utilizing LiNiCuZn-oxide anode based on slurry method

The author participated on cell manufacturing, characterization, data analysis and writing the Publication.

Publication IV: Wide bandgap oxides for low-temperature single-layered nanocomposite fuel cell

The author participated on cell manufacturing, characterization, data analysis and writing the Publication.

Publication V: Intriguing electrochemistry in low-temperature single layer ceramic fuel cells based on CuFe_2O_4

The author had a supporting role in performing the experiments and writing the Publication.

Publication VI: Carbonate dual-phase improves the ionic conductivity and performance of mixed ionic and semiconductor single-layer fuel cell

The author had a major role in material synthesis, cell manufacturing, planning and performing experiments, analysis of the data and writing the Publication.

Publication VII: Investigation of factors affecting the performance of a single-layer nanocomposite fuel cell

The author had a leading role in material synthesis, cell manufacturing, planning and performing experiments, analysis of the data and writing the Publication.

1. Introduction

1.1 Overview

The modern standard of living in the developed countries relies heavily on exploiting fossil fuels. However, burning fossil fuels causes greenhouse gas (GHG) emissions that affect the climate by increasing the global temperature. The most important GHG is carbon dioxide, CO₂. According to a recent report by Intergovernmental Panel on Climate Change (IPCC), halting the global warming to 1.5 °C requires cutting CO₂ emissions by 40 - 60 % (compared to 2010 level) by 2030 and reaching net zero emissions by 2045 – 2055 [1]. 10 – 30 % reduction by 2030 and reaching net zero emissions by 2065 – 2080 is likely to keep the global warming below 2 °C, but the consequences to the human population and the ecosystems worldwide are much more severe in this scenario compared to 1.5 °C warming [1]. Thus, a rapid reduction in CO₂ emissions is necessary.

The most important GHG emission source is energy production. According to International Energy Agency (IEA), over 80 % of the World's total primary energy supply (TPES) was satisfied by coal, oil or natural gas [2], all of which are fossil fuels. Several options are available for reducing the GHG emissions from energy production: decreasing energy demand, utilizing technologies to collect emitted CO₂ and replacing fossil fuels by new, carbon-free energy sources.

During the last 15 years renewable energy, especially electricity generation by wind power and solar photovoltaics, has been growing rapidly. In 2005, 104 TWh of electricity was generated with wind power and 4 TWh by solar photovoltaics, whereas in 2017 the respective values were 1127 and 444 TWh respectively, forming 6.1 % of the total World electricity generation (25 606 TWh) [2]. Although solar and wind as electricity sources have grown rapidly, they have some disadvantages, such as dependence on variable weather conditions. Thus they need either a backup power system or an efficient large-scale electricity storage to meet the power demand continuously.

Producing energy directly from hydrogen by using fuel cells is an intriguing concept for future energy systems. The concept of a fuel cell was first introduced over 180 years ago [3,4], but the large-scale commercial breakthrough has not yet occurred. Unlike with variable renewable energy (VRE) sources, electricity production with fuel cells can be adjusted according to the demand. Moreover, they can be combined with VRE: when excess solar and wind power is available, it can be used to produce hydrogen via electrolysis. This hydrogen can be consumed when needed. Energy system described above requires, beside fuel cells and electrolysis facilities, an advanced hydrogen storage solution.

The field of fuel cells include several different technologies with different requirements, working principles and operational temperatures. This allows a wide range of both static and mobile applications. A common factor for traditional fuel cells is their three-layer structure: two electrodes support the cell reactions whereas the electrolyte between them transports ions from one electrode to the other [3,4].

Solid oxide fuel cell (SOFC) is a fuel cell type operating at high temperature (traditionally 800 – 1000 °C, but recently lowered around 600 °C) [5-8]. SOFCs have several advantages, such as high efficiency and fuel flexibility. High temperature is required to achieve a suitable ionic conductivity, but it causes some disadvantages, such as strict requirements for the thermal expansion coefficients (TECs) of the cell components and other required structures. Moreover, high temperature can accelerate cell degradation [9,10].

Attempts to lower the operational temperature of SOFCs has led to the concept of ceramic nanocomposite fuel cells (CNFCs), where the ionic conductor is a composite material consisting of nanosized particles of a solid oxide and a salt. This innovation allows to improve the ion conduction by opening new channels for charge transfer through the electrolyte layer. The early work in CNFC field was published around year 2000 [11-14], and since then the CNFCs have been researched intensively [11,15-17].

A single-layer fuel cell (SLFC) is a recent FC technology, which breakthrough occurred in year 2011 [18]. In SLFCs, the traditional three-layer structure of a fuel cell is replaced by a single functional layer that acts as anode, electrolyte and cathode simultaneously. This allows to simplify the manufacturing procedures and to eliminate the need for matching TECs between different cell components. SLFCs have won the attraction of the fuel cell community and research is going on to study the fundamental working principles of these devices and to develop new, better-performing materials, as summarized in reviews [16,17]. This Thesis is focusing on CNFCs and SLFCs.

1.2 Objectives and scope

Although both CNFCs and SLFCs have shown great potential as future electricity generation technologies, they are not yet mature for commercial breakthrough. To be a commercially viable solution, fuel cells need to be compatible to traditional alternatives, such as diesel generators, in terms of power density and lifetime. CNFCs and SLFCs are relatively new, rapidly developing innovations, but a lot of both basic and applying research needs to be done before the requirements for commercial breakthrough can be met.

Both CNFCs and SLFCs are manufactured from nanocomposite materials and the nanostructures created have an important impact on the fuel cell performance and degradation. Thus, observing and understanding their working principles in nanoscale is the key to improve the performance and stability and to recognize the fundamental limitations of these technologies. In the SOFC field, a lot of efforts have been made to implement different microscopic and spectroscopic techniques to the characterization procedures. Since CNFCs and SLFCs

are more recent innovations, the amount of existing literature about microstructural analysis of these devices is more limited. Thus identifying the techniques that have been used successfully in the SOFC field and implementing them to the CNFC and SLFC fields is identified as a research gap. This leads to the first research question (RQ) addressed in this Thesis:

RQ1: “How different microscopic methods have been utilized in ceramic fuel cell field and how they can be used to boost CNFC and SLFC research?”

RQ1 is addressed in Publication I, a literature review presenting how electron and X-ray based microscopic techniques have been used to characterize fuel cell microstructure. The knowledge acquired through Publication I is utilized in other Publications and in the discussing parts of this Thesis. The summary originally reported in Publication I and its expansion are provided in Subchapters 3.2 & 3.3, as an answer to the RQ1.

A large variation of different materials has been applied as electrolyte for CNFCs. A composite consisting of doped cerium oxide, a typical electrolyte material for a modern SOFC, and an alkali carbonate mixture has shown great potential [15-17]. Understanding the properties and behaviour of such composites is necessary to optimize the CNFC materials and manufacturing procedure to improve the power output of the cell. This is the second research gap addressed in this Thesis. The second RQ is focusing on the doped ceria – alkali carbonate mixture:

RQ2: “How and why adding a mixture of alkali carbonates to doped ceria affects to the ionic conductivity and the total fuel cell performance?”

RQ2 is handled in Publications II&III, which are experimental studies about CNFCs based on doped ceria – alkali carbonate electrolytes. The aim of these studies is to manufacture CNFCs with high power density and to explain the high electrochemical performance by the microstructural properties of the cell components. The main results are presented in Subchapter 5.1.

SLFCs are an intriguing, new concept and even the basic working principles of the SLFCs are still under debate [16,17]. The SLFC technology has potential to reduce the fuel cell manufacturing process complexity and the respective costs significantly. However, before commercial breakthrough is possible, the understanding about the working principles of these devices has to be improved, the factors affecting to the fuel cell performance have to be analysed systematically to optimize the device and a systematic, repeatable manufacturing procedure is needed. This creates a need of fundamental research focusing on the SLFC working principles as well as systematic studies on analysing the engineering factors affecting their macroscopic performance. Addressing this gap is the third aim of this Thesis.

Typical SLFCs consists of a composite of a semiconductor and an ionic conductor [16,17]. In this Thesis, lithium nickel zinc oxide (LNZ) and copper iron

oxide (CFO) are used as semiconducting component and doped ceria, or its mixture with alkali carbonates, as ionic conductor. The third and fourth RQs are formed as follows:

RQ3: “Why do SLFCs work and how the charge transfer through the cell is divided between different ions?”

RQ4: “How the ionic conductor composition, the catalytic activity of the current collector and the porosity of the single-layer affect to the performance of LNZ-based SLFCs?”

RQs 3&4 are answered with Publications IV-VII. Publications IV&V are focusing on RQ3 and Publications IV&V to RQ4, although there exists some overlap between The Publications and the RQs. The focus of Publications IV&V is to study the working principles of two different SLFCs. The key findings are presented in Subchapter 5.2. Publications VI&VII apply the knowledge from ceria – carbonate ionic conductors (Publications II&III) to the SLFC field. In these Publications, a large number of LNZ-based SLFCs are fabricated, characterized and compared to each other, as presented in Subchapter 5.3.

The relations between different Publications are illustrated in Figure 1. The role of Publication I is to provide a literature review and tools for the research presented in other Publications. The Publications II-VII can be arranged into pairs. Publications II&III are focusing on CNFCs, whereas Publications IV&V focus on working principles of (non-carbonate containing) SLFCs. In Publications VI&VII, knowledge from both sides is utilized to fabricate SLFCs (both with and without carbonates) and to analyze them in a systematic way.

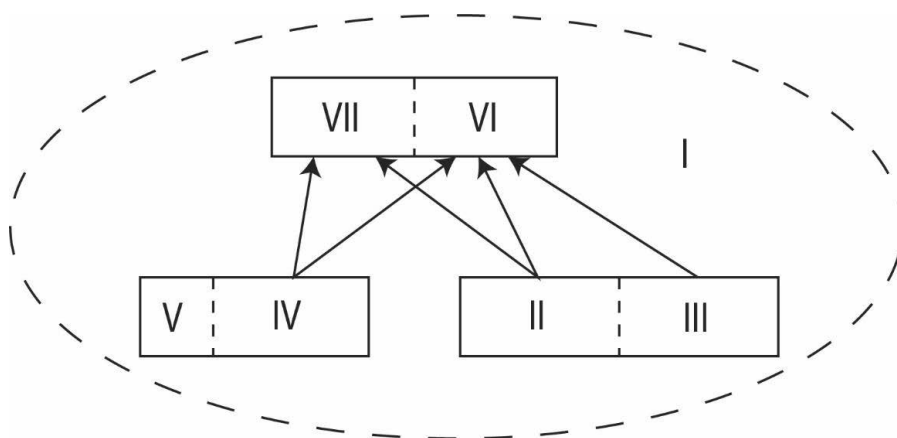


Figure 1. An illustration showing the relations between the Publications included in this Thesis.

1.3 Structure of this Thesis

This Thesis is divided into seven Chapters. Chapter 1 (Introduction) provides an overview to the broad context of the field, explains the motivation for this work and presents the RQs answered with this Thesis. Chapter 2 (Fuel cells) explains the basic working principles of a fuel cell and discusses about different fuel cell types. Chapter 3 (Literature review) presents a summary of existing scientific knowledge from the fields relevant for this Thesis. Together these Chapters show the current status of CNFC and SLFC research and provide the motivation to why these devices deserve more scientific research.

Chapter 4 (Materials and methods) and Chapter 5 (Results) are the core part of the experimental research reported in this Thesis. Together these Chapters show how CNFCs and SLFCs are fabricated starting from commercially available chemicals, characterized with both macroscopic and microscopic methods and what were the key results achieved experimentally in Publications II-VII.

Chapter 6 (Discussion) discusses about the results included in this Thesis and reported in literature as one entity. Chapter 7 (Conclusions) wraps up this Thesis, presents the main conclusions and gives recommendations for the future work. The purpose of these Chapters is to provide answers to the RQs and to explain the impact of this Thesis to the scientific community and the wider society.

2. Fuel cells

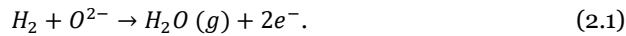
Fuel cells are devices that convert the chemical energy of the fuel directly to electricity, skipping completely the mechanical transformation part that is necessary in traditional combustion power plants [3,4]. This allows high-efficiency electricity generation from a suitable fuel. Fuel cells can be considered as a green energy source if e.g. pure H_2 is used as a fuel; in such a case the only byproduct of the electricity generation is water. Even when e.g. natural gas is used as a fuel, the high efficiency of the fuel cells allows to produce the required electricity from a smaller amount of the fuel, thus reducing fuel consumption and greenhouse gas emissions.

This Chapter presents the concept of a fuel cell. After general introduction to the topic and presentation of the traditional fuel cells, the Chapter focuses on ceramic nanocomposite fuel cells (CNFCs) and single-layer fuel cells (SLFCs) that were the two fuel cell types that were studied in this Thesis.

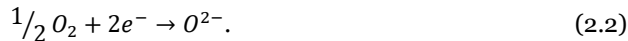
2.1 Principle of fuel cells

Traditional fuel cells consist of a three-layer structure: anode, electrolyte and cathode [3,4]. The fuel gas (e.g. H_2) is supplied to the anode (negative electrode) and the oxidant (e.g. air) to the cathode (positive electrode). The electrolyte is responsible for ion transportation through the cell and acts as a gas separator, preventing the direct mixing of the fuel and the oxidant. The working principle of a fuel cell is presented below by using a solid oxide fuel cell (SOFC) [5,6] utilizing pure H_2 as fuel as an example. A schematic is shown in Figure 2. For other fuel cell types, the exact reactions occurring during the operation and the ions responsible for the charge transfer may be different.

The fuel gas (here H_2) supplied to the anode reacts with O^{2-} ions from the electrolyte according to the following anodic half-reaction:



The water vapour is removed from the cell, whereas the released electrons are collected to the external circuit and driven to the cathode, where they react with the supplied oxygen according to the cathodic half-reaction:



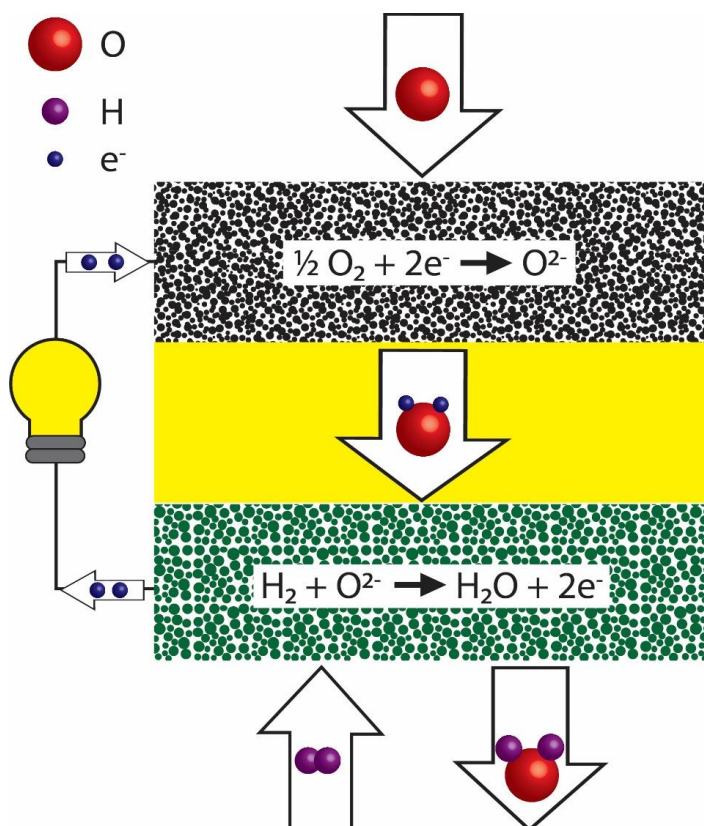


Figure 2. A schematic showing the working principle, charge transfer and gas flow in a solid oxide fuel cell. Reproduced with permission from Publication I, © Wiley.

The formed O^{2-} ions are transferred to the anode through the electrolyte and can be used as reactants for the anodic half reaction (Eq. 2.1). Thus the total fuel cell reaction is:



Supporting this working principle sets certain requirements for the materials that can be used in fuel cells. The electrodes need to be porous and have sufficient ionic and electronic conductivity to allow transportation of gases, ions and electrons respectively. Moreover, they should be able to catalyze the respective half-reactions and to be stable in the gas atmosphere and temperature that they are exposed during the fuel cell operation.

The electrolyte has to be gas tight and an electronic insulator to prevent direct gas mixing and short-circuiting through the cell. A good ionic conductivity for the ion responsible of the charge transfer through the cell is a crucial property. Since the electrolyte is exposed to both reducing and oxidizing atmospheres, it should be stable in both environments. Especially in high-temperature fuel cells, such as SOFCs, the thermal expansion coefficients (TECs) of the fuel cell components need to match to prevent breaking of the cell during heating or cooling.

The maximum voltage of a single fuel cell can be calculated theoretically based on thermodynamics [3,5]. The actual voltage during the operation is usually significantly lower due to internal losses of the fuel cell. Typical open-circuit voltage (OCV) of a FC is around 1 V [5] and it decreases further when current is drawn from the FC. Thus in real-world electricity production applications fuel cells are operated as stacks, where multiple fuel cells are placed in series and parallel connections to achieve the desired voltage and power output [5]. In this Thesis, the focus is on laboratory-scale single fuel cells and thus the stacking of the fuel cells and the components required for it are excluded.

Several types of fuel cells that are based on different materials and half-reactions exist. The fuel cells are typically categorized based on the electrolyte material. Polymer electrolyte membrane, a.k.a. proton exchange membrane, fuel cells (PEMFCs) are operating at low temperatures, typically around 100 °C [3,4,19]. Phosphoric acid fuel cells (PAFCs) operate at a bit higher temperature, near 200 °C [3,4]. Both PEMFCs and PAFCs are based on H^+ conduction. Alkaline fuel cells (AFCs) operate around 100 °C and the charge transfer through the KOH-electrolyte is done by OH^- ions [3,4,20]. Molten carbonate fuel cells (MCFCs) are using a mixture of alkali carbonate salts as electrolyte and operate above the melting point of the carbonate mixture (several hundreds of °C) [3,4,21]. A more detailed description of each FC type can be found from e.g. [3,4].

SOFC [3-8], which working principle is presented above, has drawn a lot of attention from the fuel cell research community during the last decades. Although SOFCs have been researched intensively, a large scale commercial breakthrough has not yet occurred. One of the major challenges for SOFC commercialization is the high operation temperature that is necessary to achieve a suitable ionic conductivity through the electrolyte. This sets strict limits for the materials used in cells and supporting structures (e.g. interconnects) and their thermal compatibility. Moreover, at least some of the degradation mechanisms occur faster at high temperature [9,10]. Although doped ceria (usually gadolinium- or samarium-doped, GDC or SDC respectively) has been researched as an alternative to the traditional yttria-stabilized zirconia (YSZ) electrolyte in the near past allowing to reduce the operational temperature down from 800 – 1000 °C [5-8] even with thick electrolytes, further reduction in operation temperature is still required.

2.2 Ceramic nanocomposite fuel cell

Lowering the operational temperature can help to solve several challenges in the SOFC field. The key to reduce the operational temperature of SOFCs is to reduce the ohmic losses resulting from the ion conduction through the electrolyte. Since the ohmic resistance due to the ionic conduction is the product of the resistivity and the thickness of the electrolyte layer, at least one of these parameters need to be reduced. Replacing the YSZ electrolyte by doped ceria that has superior (by an order of magnitude [5,6,8]) ionic conductivity (i.e. lower resis-

tivity towards ion conduction) at lower temperatures, allowing to reduce the operational temperature from 800 – 1000 °C to around 550 °C [5], but further development is required. This has led to developing of fuel cells based on composite electrolytes that have higher ionic conductivity. Such devices are referred as ceramic nanocomposite fuel cells (CNFCs) in this Thesis and discussed below.

In CNFCs, the ionic conductivity of the electrolyte is improved by using composite materials that consist of doped ceria and a salt [11-17]. In the early CNFC research, several options for the salt component has been studied, including e.g. fluorides, chlorides and hydroxides [11-14]. More recently, the research has focused on alkali carbonates and their mixtures, such as Na_2CO_3 (NC) [22-24], $(\text{Na}_x\text{Li}_{1-x})_2\text{CO}_3$ (NLC) [25-30] and $(\text{Na}_x\text{Li}_y\text{K}_{1-x-y})_2\text{CO}_3$ (NLKC) [31,32]. Typically the weight ratios between the different carbonates in NLC and NLKC are chosen to minimize the melting temperature. This weight ratio is known as the eutectic mixture.

Such composites can be considered as a fusion of traditional SOFC and MCFC materials. The electrode materials used in CNFCs and the requirements for different components (e.g. porosity of the electrodes and gas-tightness of the electrolyte) are mostly the same than the ones in low-temperature SOFCs. Thus CNFCs can be considered as an evolution step of low-temperature SOFCs.

In doped ceria, a typical solid oxide fuel cell (SOFC) electrolyte, the ion transportation is based on oxygen vacancies. Pure ceria forms a cubic fluorite structure [33], shown in Figure 3a. When a fraction of tetravalent Ce^{4+} ions are replaced by trivalent dopant ions, such as Sm^{3+} or Gd^{3+} , oxygen vacancies are created to maintain the charge balance, as illustrated in Figure 3b. The vacancies can move in the lattice, allowing O^{2-} ion –based charge transfer. Typical molar percentage of the dopant ion is between 10 and 20. This doping percentage is low enough to maintain the cubic fluorite structure with vacancies [33,34]. If the doping percentage is increased further, the lattice structure changes and the vacancies are no longer free to move [33,34]. The mobility of the oxygen vacancies, and thus the ionic conductivity of the doped ceria electrolytes, depends strongly on the temperature and thus the ionic conductivity of the electrolyte is often the limiting factor preventing to lower the operational temperature [5].

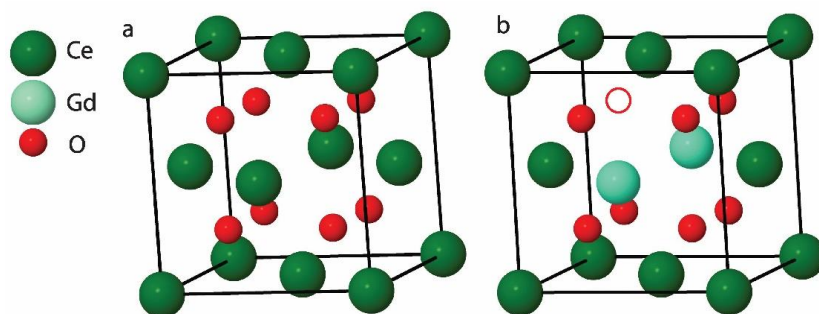


Figure 3. Cubic fluorite structure of CeO_2 : Ce^{4+} -ions are placed at the corners and the centers of the faces of the cube, whereas O^{2-} -ions form a smaller cube inside the unit cell (a). When a fraction of Ce^{4+} -ions are replaced with Gd^{3+} -ions, oxygen vacancies (hollow red circle) are created, allowing O^{2-} -ion conduction through the lattice (b).

The main benefit of CNFCs over SOFCs results from the composite electrolyte properties. Below the melting temperature of the carbonate mixture, the ion conduction is done only through the oxide phase, just as in SOFCs. But when the carbonates are melted, new conduction channels are opened. It is suggested that, besides the oxide phase, the conduction can be done through the molten phase, through the interfaces between the molten and oxide phases and through combinations of these mechanisms [35]. Besides O^{2-} ions, also negative CO_3^{2-} and positive H^+ and alkali metal (e.g. Li^+ and Na^+) ions can contribute to the charge transfer [16,17,35,36]. As a result, the ionic conductivity is improved rapidly near the melting point of the carbonate mixture (conductivity of doped ceria increases exponentially when inverted temperature is decreased [17], whereas doped ceria – alkali carbonate mixture shows a sudden increase by several orders of magnitude in a small temperature range around the melting point [17], Publications II&III), allowing to lower the operational temperature compared to SOFCs giving that the electrode materials have a suitable catalytic activity at the new operation temperature. This phenomenon is studied more in Subchapter 5.1. State-of-the-art CNFCs are presented in more detail in Subchapter 3.1.1.

2.3 Single-layer fuel cell

Replacing the traditional three-layer structure with a single functional layer can solve several challenges for fuel cells. Polarization losses at the interfaces of the different layers and the requirement for matching TECs will disappear in the single-layer structure. Moreover, the manufacturing procedure for the fuel cell can be simplified when only one layer is manufactured instead of three.

These devices are known as single-layer fuel cells (SLFCs) [16,17]. In the literature, also other abbreviations have been used, e.g. SCFC (single component fuel cell) and EFFC (electrolyte free fuel cell). These abbreviations are not synonyms: e.g. a fuel cell consisting of multiple layers, none of which is electrolyte, is an EFFC but not a SLFC. For consistency, the abbreviation SLFC is used in this Thesis whenever it is suitable to describe the device.

The material of the single-layer has to support both half-reactions at the edges of the cell and allow ion transportation through the cell, meanwhile also preventing short-circuiting and direct gas mixing. Typical single-layer materials are composites, consisting of an electronic or semiconductor (e.g. lithium nickel zinc oxide, LNZ) and an ionic conductor (e.g. doped ceria). The development in the CNFC field can be applied to SLFCs as well, by using composite electrolytes described in Subchapter 2.2 as ionic conductors for SLFCs.

Since SLFCs are a recent innovation, the amount of scientific knowledge in the SLFC field is still lower compared to e.g. SOFCs. Even the exact working principles of the SLFCs are still under debate. Since the SLFC composite includes a material that can conduct electrons, there has to be a mechanism that prevents the short-circuiting. Several candidates have been suggested, e.g. Schottky junctions [37-40] and the formation of electron barriers or depletion zones due to p-n junctions [40-43] between the edges of the cell. State-of-the-art SLFCs and their suggested working principles are presented in detail in Subchapter 3.1.2.

3. Literature review

This Chapter summarizes the scientific knowledge available through the literature in research fields that are relevant for the scope of this Thesis. The first Subchapter is dedicated to present the state-of-the-art situation for relevant fuel cell technologies: ceramic nanocomposite fuel cells (CNFCs) and single-layer fuel cells (SLFCs). The second Subchapter focuses on applying microscopic techniques to fuel cell research, based on Publication I. Finally, the key challenges and gaps in the CNFC and SLFC research are discussed.

3.1 State-of-the-art of fuel cells

Reducing the ohmic resistance due to limited ion conduction through the solid oxide fuel cell (SOFC) electrolyte can be done e.g. by reducing the thickness of the electrolyte layer and/or resistivity of the electrolyte material. Screen-printing is a cost-effective method that has been able to produce electrolyte layers with thicknesses around 2.5 – 20 μm [44-48]. Lee et al. reported of a SOFC based on 5 μm thick GDC electrolyte layer prepared by dip-coating that achieved a power density of 1970 mW/cm^2 at 550 $^{\circ}\text{C}$ [49]. A 5 μm thick YSZ electrolyte prepared by spin-coating has been reported as well [50].

The latter approach, reducing the resistivity of the electrolyte layer material, has led to the development of CNFCs that are based on composite electrolyte layers. The following Subchapter summarizes the state-of-the-art results from the CNFC field.

3.1.1 Ceramic nanocomposite fuel cell

The CNFC electrolyte is a composite material consisting of a solid oxide and a salt, typically doped ceria and alkali carbonate [22-32]. When a carbonate mixture is mixed with doped ceria, the resulting nanopowder has been shown to form a core-shell structure with ceria cores surrounded by carbonate shells [24]. When the fuel cells are prepared and heated above the melting temperature of the carbonate, the electrolyte has a dual-phase structure, consisting of a solid oxide and molten carbonate phases [30]. This opens new channels for the ion conduction and, besides O^{2-} , also CO_3^{2-} , H^+ and alkali metal (e.g. Na^+) ions can contribute to the charge transfer. This multi-ion conduction has been confirmed experimentally [22,26,29]. H^+ have been shown to dominate the conduction over O^{2-} in CNFC operational conditions by 1-2 orders of magnitude with SDC-NC (4:1 by weight) electrolyte via four-probe conductivity measurements [22].

In another experiment similar conclusions were made with SDC-NLC by observing the water formation in anode and cathode gas outlets, although with low (< 20 w-%) carbonate content also the contribution of O^{2-} was significant [26]. For NLKC, the native (alkali metal and CO_3^{2-} ions) have been shown to dominate over the foreign (O^{2-} , OH^-) ions by approximately two orders of magnitude in charge transfer, although the effect of H_2 was not included in the particular study [36].

CNFCs based on doped ceria – alkali carbonate mixture composite electrolytes have been applied widely in the literature with impressive performance. The most commonly highlighted performance indicator in CNFC (and SLFC) literature for the single cells is the maximum power density, so it was chosen as the main indicator for comparing different cells in this Thesis, although some other indicators, such as open circuit voltage (OCV, V_{OC}) and area-specific resistance are relevant as well. Some noteworthy results include 1100 mW/cm² at 550 °C with SDC-NLKC [31], 1060 mW/cm² at 550 °C with GDC-NLC [25], 730 mW/cm² at 550 °C with SDC-NC [23], 900 mW/cm² at 580 °C with strontium-samarium co-doped ceria (SSDC) – NC [24], 1704 mW/cm² at 650 °C with SDC-NLC [27] and 1085 mW/cm² at 600 °C [26] with SDC-NLC. Electrode materials of the cells mentioned above are shown in Table 1. More comprehensive reviews on CNFCs based on ceria-carbonate mixtures can be found e.g. from [15-17,51].

Although the nanocomposite electrolyte is the key component in CNFCs, research focused on electrode materials is also important. Tan et al. studied a variety of different cathodes based on modified lithiated nickel oxides [52]. Patakangas et al. showed that the lithium nickel cobalt zinc oxide (LNCZ) anodes prepared via slurry method had smaller particle size, larger surface area and higher porosity compared to LNCZ anodes prepared via solid route, resulting as a lower polarization resistance (0.21 vs. 0.31 $\Omega \cdot cm^2$ at 550 °C) [32].

To make a commercial success, the long-term stability of CNFCs has to reach a suitable level, providing a lifetime of even tens of thousands of hours. Due to complexity of these devices and a large variety of materials, multiple degradation mechanisms need to be halted to meet this target. Besides the fundamental degradation mechanisms of SOFCs, summarized in [9,10], also degradation mechanisms typical to molten carbonate fuel cells (MCFCs) [21,53] may occur in CNFCs.

Stability of CNFCs has not been researched as intensively as e.g. potential material candidates to improve the power density, although a few scientific articles about the issue exists. A CNFC with SDC-NLC electrolyte, NiO anode and CuO cathode operated stably for 200 h in typical MCFC conditions, although the power density was relatively low (around 110 mW/cm²) [54]. In another experiment, a performance of ceria-carbonate based cell actually improved for the first three months, although it should be noted that the cell was operated only 2-3 h per week [14]. A stable conductivity at 600 °C in air have been reported for 6000 h for GDC-NLC [55] and for 3 days for GDC-KLC [56], but since H_2 was not present, these conditions do not represent actual operational conditions. In another study, a conductivity decrease from 0.26 to 0.21 S/cm was observed

for Y, Gd co-doped ceria (YGDC) - NLC electrolyte during 135 h aging test in air at 550 °C [57].

The working principle and material candidates for CNFCs have been researched intensively, as discussed above. However, the stability issues clearly require more comprehensive and systematic studies.

3.1.2 Single-layer fuel cell

Although the concept of SLFC has been proved already in year 2000 with $\text{La}_{0.9}\text{Sr}_{0.1}\text{InO}_{3-8}$ [58], the breakthrough for SLFC technology occurred in year 2011. Zhu et al. reported of a SLFC consisting of lithium nickel oxide (LN) mixed with GDC that achieved 450 mW/cm² at 550 °C [18] and soon after that several other SLFCs that consisted of two core materials, modified LN, e.g. LiNiZnO (LNZ) or LiNiCuZn(Fe)O (LNCZF), and an ionic conductor (doped ceria or a mixture of a doped ceria and an alkali carbonate) were reported [41,43,59,60]. LNCZF-(SDC-NC) composite achieved 700 mW/cm² at 550 °C [60], being superior to a three-layer fuel cell utilizing the same materials.

The high electrochemical performance of SLFCs raised questions about the working principles of these devices. In the traditional three-layer fuel cells, the electrolyte is gas-tight and electronic insulator, preventing both gas mixing through the cell and short-circuiting. SLFCs do not have a separate electrolyte layer, but obviously the cells are not short-circuiting: in Zhu's early work equal OCVs of 1.0 V were reported with SLFCs [18,41,43,59,60] and traditional three-layer FCs [18,41,59,60] utilizing same materials. Zhu et al. proposed that p-n junctions are formed in the semiconductor phase of the single layer, e.g. between NiO (p-type semiconductor) and ZnO (n-type), allowing the charge separation [41,43,59] similarly to solar cells. This idea was developed further by explaining the SLFC performance by nano-scale redox reactions [61]. Schottky barriers, i.e. contacts between metals and semiconductors, have been reported as well in SLFCs [37-40]. A model developed by Liu et al. showed that the reaction depths for H₂ and O₂ are 1-2 orders of magnitude lower than the typical SLFC thickness, explaining why the gas mixing is not occurring even in porous SLFCs [42]. A more detailed discussion about the working principles of SLFCs is reported elsewhere [16,17].

Besides LN, LNZ and LNCZF, also other semiconductors based on modified LN have been reported as SLFC materials, including LiNiFeO (LNF) [62], LiNiCuSrO (LNCS) [63,64], LiNiMnSrO (LNMS) [64], LiNiCoSrO (LNCoS) [64] and LiNiCuZnO (LNCZ) [65]. A 2:3 weight ratio between the semiconductor and ionic conductor was found to be optimal for both LNCS-SDC [63] and LNCZ-(SDC-NC) [65] materials. For LNCZ-(SDC-NC), 1.1 mm thick pellets showed the best performance [65]. Hu et al. found a tradeoff between performance and stability: at 550 °C the power densities were in order LNMS-SDC > LNCoS-SDC > LNCS-SDC, but the thermal gravimetric analysis revealed that LNMS was the most unstable of these materials [64].

Multiple alternatives for LN-based oxides have been reported in the literature, including $\text{Sm}_{0.5}\text{Sr}_{0.5}\text{CoO}_3$ (SSC) [66], $\text{Ni}_{0.8}\text{Co}_{0.15}\text{Al}_{0.05}\text{LiO}_2$ (NCAL) [40,67-69], $\text{La}_{0.6}\text{Sr}_{0.4}\text{Co}_{0.2}\text{Fe}_{0.8}\text{O}_{3-8}$ (LSCF) [70-73], $\text{Ba}_{0.5}\text{Sr}_{0.5}\text{Co}_{0.2}\text{Fe}_{0.8}\text{O}_{3-8}$ (BSCF) [37],

$\text{Sr}_2\text{Fe}_{1.5}\text{Mo}_{0.5}\text{O}_{6-\delta}$ (SFM) [39,74] and $\text{Pr}_{0.4}\text{Sr}_{0.6}\text{Co}_{0.2}\text{Fe}_{0.7}\text{Nb}_{0.1}\text{O}_{3-\delta}$ (PSCFN) [40]. Besides mixing with carbonates, the properties of the doped ceria has been modified by co-doping (e.g. Ca, Sm co-doped ceria (CSDC) [69,70,72,73], La, Pr co-doped ceria (LPDC) [71] and La, Pr, Nd co-doped ceria (LPNDC) [67]), and mixing it with KZnAlO (KAZ) [75] or MnZnO (MZ) [76].

The SLFCs with an ionic conductor consisting of co-doped ceria or a ceria – alkali carbonate mixture have shown power densities exceeding 1 W/cm^2 : 1187 mW/cm^2 with NCAL-LPNDC [67], 1080 mW/cm^2 with LSCF-CSDC [72] and 1072 mW/cm^2 with NCAL-(SDC-NC) [68] have been reported at 550°C . Slightly lower power densities have been reported with single-doped ceria: 841 mW/cm^2 with SFM-SDC [39], 760 mW/cm^2 with LNF-SDC [62] and 741 mW/cm^2 with SSC-SDC [66] at 550°C .

When the components of the single-layer composite are varied, also the optimal weight ratio may change. With SSC-SDC [66], LSCF-LPDC [71] and NCAL-(SDC-NC) [68], the 2:3 weight ratio was found to be optimal, identically to LNCS-SDC [63] and LNCZ-(SDC-NC) [65], whereas NCAL-LPNDC [67], SFM-(SDC-NC) [74] and NCAL-CSDC [69] showed the peak performance with a weight ratio of 3:7. Also 1:1 weight ratio between LSCF and CSDC has been reported, although optimizing the weight ratio was not included to the particular study [73].

The role of NCAL in SLFCs is an interesting matter. Besides as a component of the single-layer composite, it has been used as a current collector, typically painted on a Ni-foam [37,69,71,73]. However, NCAL current collectors can affect the cell performance e.g. by boosting the electrode reactions, or even acting as an electrode due to the catalytic activity of NCAL [37,73]. On the fuel side, the NCAL is at least partly reduced to Ni-Co alloys [37,71] and thus forming a Schottky junction with the semiconductor component of the single layer. This is one offered explanation for the efficient charge separation in SLFCs.

Considering from commercial point of view, upscaling the active area and improving the stability of the SLFCs is a crucial factor. Hu et al. have reported of $6 \times 6 \text{ cm}$ SLFCs with an active area of 25 cm^2 prepared from LNCS-(MZ-SDC) [76] and LiMgZnO (LMZ) – SDC [77] that reached power densities of 371 and 512 mW/cm^2 at 600°C respectively. In [76], also a small LNCS-(MZ-SDC) cell (active area 0.64 cm^2) was prepared and it achieved 600 mW/cm^2 at 650°C . Upscaling the active area of the cell seems to decrease significantly the power density, at least in that particular study.

The large LMZ-SDC cell reported in [77] showed a stable performance over 120 h operation. LSCF-LPDC [71], NCAL-(SDC-NC) [68] and PSCFN-(SDC-NLC) [40] cells have shown stability for 14 h, 10 h and 48 h respectively. However, since the lifetime of commercially viable fuel cells should be in range of tens of thousands of hours, a suitability for commercial production cannot be claimed based on these experiments.

To sum up, the SLFCs are a recent innovation building on SOFCs and CNFCs that has been studied intensively during the last decade. Although the field is developing rapidly, several challenges still remain. More information can be found e.g. from review articles [16,17,78].

Table 1. A summary of noteworthy power densities achieved in the literature with FC technologies relevant for this Thesis. In Material-column the syntax is [anode – electrolyte – cathode] for the SOFC and CNFCs and [electronic/semiconductor–ionic conductor] for the SLFCs.

FC type	Material	Power density (mW/cm ²)	Temperature (°C)	OCV (V)	Gas flow rates (ml/min)	Ref.
SOFC	(NiO-GDC) – GDC – (BSCF-GDC)	1970	550	0.92	H ₂ : 80 Air: 300	[49]
CNFC	(LNCZ-SDC-NC) – (SDC-NC) – (LNCZ-SDC-NC)	730	550	1.03	H ₂ : 80-110 Air: 80-110	[23]
CNFC	(LNCZ-SSDC-NC) – (SSDC-NC) – (LNCZ-SSDC-NC)	900	580	1.00	H ₂ : 100 Air: N/A	[24]
CNFC	(NiO-GDC-NLC) – (GDC-NLC) – (LSFC-GDC-NLC)	1060	550	1.19	H ₂ : N/A Air: N/A	[25]
CNFC	(NiO-SDC-NLC) – (SDC-NLC) – (LN-SDC-NLC)	1085	600	0.95	H ₂ : 40-100 Air: 40-100	[26]
CNFC	(NiO-SDC-NLC) – (SDC-NLC) – (LN-SDC-NLC)	1704	650	1.13	H ₂ : 100 CO ₂ /O ₂ (1:1): 100	[27]
CNFC	(NiO-SDC-NLKC) – (SDC-NLKC) – (LSFC-SDC-NLKC)	1100	550	1.20	H ₂ : N/A Air/CO ₂ : N/A	[31]
SLFC	SFC-SDC	841	550	1.10	H ₂ : 80-120 Air: 150-200	[39]
SLFC	LNF-SDC	760	550	1.03	H ₂ : 80-120 Air: 150	[62]
SLFC	SSC-SDC	741	550	1.08	H ₂ : 80-120 Air: 150-200	[66]
SLFC	NCAL-LPND	1187	550	1.07	H ₂ : 120 Air: 120-150	[67]
SLFC	NCAL-(SDC-NC)	1072	550	0.97	H ₂ : 80-120 Air: 150-200	[68]
SLFC	LSCF-CSDC	1080	550	1.06	H ₂ : 100 Air: N/A	[72]

3.1.3 Summary

Both CNFCs and SLFCs are promising FC technologies that have been researched intensively during the last decade, building on the knowledge acquired from the SOFC field. The focus of the research has been on the material selection and optimizing the power density. However, there is only a very limited amount of scientific literature about up-scaling and long-term stability of CNFCs and SLFCs that are crucial factors for commercialization. Table 1 summarizes the high power densities achieved in the literature, presented previously in this Chapter. It should be noted that Table 1 presents the high-end of power densities reported in the literature.

3.2 Microstructural analysis of fuel cells (Publication I, RQ1)

Since ceramic fuel cells, both single- and three-layer fuel cells, are complex structures in micro- and nano-scale, characterizing the nanolevel properties of the fuel cells and the materials that are used to manufacture them is crucial to understand their working mechanisms and explain macroscopic observations. This Subchapter is dedicated to present how spectroscopy and microscopy have been used in the existing fuel cell literature and to explain the working principles of the respective techniques. The focus is on five different methods: X-ray

diffraction spectroscopy (XRD), scanning electron microscopy (SEM), transmission electron microscopy (TEM), focused ion beam – scanning electron microscopy (FIB-SEM) and X-ray nanotomography. The Subchapter is based, but not limited, to the review originally presented in Publication I.

3.2.1 X-ray diffraction spectroscopy

XRD is a spectroscopic technique that is based on constructive interference of X-rays reflected from a crystalline lattice. This allows to identify the crystalline structure of the sample and to analyze its properties, such as average particle size and lattice constant. XRD can be performed on both nanosized powders and the complete fuel cell pellets.

When a collimated beam of monochromatic X-rays interacts with a sample (e.g. nanopowder) in an angle that follows the Bragg's law

$$n \cdot \lambda = d \cdot \sin\theta, \quad (4.1)$$

where n is an integer, λ the wavelength of incident X-rays, d distance between two lattice planes and θ the incident angle of the X-rays, a constructive interference is occurred. When the XRD-spectrum (i.e. number observed X-rays as a function of 2θ) is measured over a wide range of 2θ , the constructive interferences can be seen as peaks for the respective angles.

The identity and the crystalline orientation of each component of the studied sample can be determined from the location of the peaks by using a suitable data library (e.g. International Crystalline Diffraction Database, ICDD). A more detailed analysis of the peak width and shape allows to calculate the lattice constant of the respective structure and the average particle sizes, based on the Scherrer equation [79,80]. Since the sample is likely to cause several peaks, the accuracy of e.g. particle size determination can be improved by averaging the particle sizes calculated independently from different peaks.

For CNFCs, the crystalline structure of doped ceria [24,31] and perovskite-structured cathodes (such as LSM, LSC, LSF and LSCF) [25] can be identified by XRD. Besides identifying the materials, XRD allows to calculate the average particle sizes (from Scherrer equation) [24,31] and the lattice parameters [24] of the studied material. Carbonates have typically a low crystalline orientation and thus the XRD peaks originated from carbonates are small compared to crystalline structures [25,31], or even non-existing [24].

In the SLFC field, XRD is a typical characterization tool for the single layer composite and its individual components. The doped cerias have been observed to show the cubic fluoride structure of pure CeO_2 [63,64,66,68,69,71,73,76], with a small angle shift due to properties of the dopant ion, assuming that the doping process has succeeded. Perovskite-structured semiconductor components, such as SSC [66], LNCS [63,64,76], LNMS [64], LNCOS [64], LSCF [71] and NCAL [68,69] show spectra respective to their structure. Composite samples consisting of an ionic conductor and a semiconductor show peaks from both phases [63,66,68,69,71,76]. XRD can be used to confirm that the material synthesis has succeeded and that there are no unwanted crystalline phases.

Performing XRD-measurements over a wide range of temperatures reveal information about the thermal properties of the studied material. This is called as high-temperature XRD (HT-XRD). Typically, when temperature is increased, a peak shift towards lower angles is observed due to the lattice expansion [81-84]. The change in the shape of the peak can indicate about structural changes in the material [81], whereas similar shape of peaks over the measured temperature range indicates about structural stability [82-84].

XRD have been found to be a useful tool to characterize CNFC and SLFC nanopowders with a simple and quick measurement. XRD allows e.g. identifying crystalline phases and determining average particle sizes, but a more detailed nanoscale characterization requires electron microscopy.

3.2.2 2D microscopy

Electron microscopy is based on observing interactions between a high energy beam of primary electrons (PEs) and the sample. SEM observes the interactions near the surface of the sample, thus providing a good surface view. TEM is based on electrons that go through the sample, setting a criteria for electron transparency. Elemental mapping is possible with both techniques, by using energy-dispersive X-ray spectroscopy (EDX) or electron energy loss spectroscopy (EELS, TEM only).

Working principle of electron microscopes

The high-energy PE beam is generated by using a high-voltage electron gun and it is directed on the sample with suitable optics. When a PE hits the surface of a sample, several interactions may occur. A summary of the possible interactions is shown in Figure 4. Different electron microscopy techniques are focused on observing these interactions and utilizing this information to construct a high-resolution image of the sample.

Secondary electron (SE) is created when the incident PE knocks out an electron bound to sample. SEs have low energy (< 50 keV, typically < 2 keV [85,86]), so the SEs generated deep in the sample are likely to be absorbed by the sample itself. If a SE is created close to the sample's surface, however, it may be able to escape the sample and to be detected. SE-imaging is a typical SEM technique that allows to build a topographic contrast of the samples surface, to a depth of a few dozen nanometers [85,86].

If the incident electron interacts with a nucleus, it is scattered elastically in a high angle. These electrons are known as backscattered electrons (BSEs). Since the cross-sectional area of a nucleus (and thus its ability to backscatter electrons) depends strongly on its size, BSE-imaging allows to build a clear contrast between light and heavy elements. Since BSEs are actually elastically scattered PEs, they have a high energy and thus they can escape deeper from the sample than SEs [86]. The information depth of BSEs varies strongly depending e.g. from the energy of the PE beam and the diameter of the studied nanoparticles, but it is usually in range of hundreds of nanometers [87].

When an inner shell electron is knocked out from an atom (e.g. as result from interaction with a high-energy PE), it is replaced by an electron from outer shell

due to nature's tendency to form energetically favourable structures. During the process, the atom emits an X-ray which energy equals to the energy difference between the electrons in the outer and the inner shells. Since the energies of the electron shells, and thus the energy differences between electrons in different shells, are individual for each element, observing these characteristic X-rays allows to identify the elements the sample consists of. This technique is called energy dispersive X-ray spectroscopy (EDX) and it can be used with both SEM and TEM.

Whereas SEM is a useful technique to study the interactions near the sample's surface, TEM is focused on observing the PEs that go through the sample. This causes the most significant limitation for TEM: it can be applied only on samples that are thin enough to allow electron transparency. The main benefit over SEM is the improved resolution: modern TEMs can separate objects which distances are in Ångström ($1 \text{ \AA} = 0.1 \text{ nm}$) range, allowing to see individual atoms and crystalline orientations in TEM images.

The most straightforward TEM application is observing the PEs that have gone through the sample without interacting with it. This is known as bright field (BF) imaging. In a BF image, the areas with high electron transparency (i.e. from none to few particles that can interact with PEs) appear bright, whereas the areas with a lot of interaction (i.e. a lot of particles) appear dark.

In dark field (DF) imaging mode, the detector is adjusted so that it is in a certain angle compared to the initial PE beam. Thus, only those electrons that interact with the sample by scattering to this particular angle can be detected and the areas where such interactions occur appear bright in a DF image. This allows efficient detection of certain crystalline structures from the studied sample.

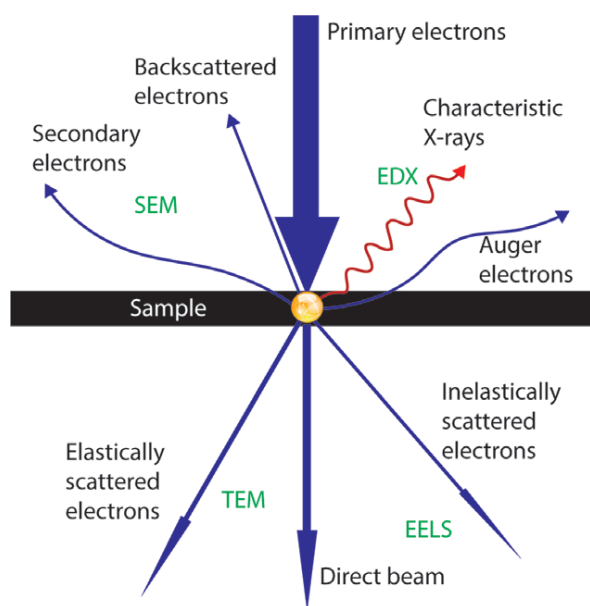


Figure 4. Interactions that may occur when a high-energy electron interacts with a sample that is imaged by an electron microscopy method. SEM is focused on interactions near the surface and TEM on the transmitted electrons. Reproduced from Publication I with permission, © Wiley.

Elemental analysis is possible in TEM imaging by two different approaches. EDX can be done similarly than in SEM imaging. Another approach is known as electron energy loss spectroscopy (EELS). If a PE interacts with sample by exciting an electron from inner to outer shell, a part of its energy, corresponding to the energy difference between the base state and excited state, is transferred to the excited electron. This interaction is known as inelastic scattering. EELS is based on observing inelastically scattered electrons and determining their energy. Since the initial energy of the PEs is known (based on the accelerating voltage), the energy loss occurred in inelastic scattering can be calculated from the difference between the initial and the final energy of the PE. This allows the identification of the element from which the PE has scattered, since the energies required for the electron excitation are individual for each element.

Applications on solid oxide fuel cells

Both SEM and TEM have been applied widely in SOFC literature. A simple cross-sectional image by SEM allows to identify different layers and the existence of cracks in a fuel cell [49,88-92], whereas a surface image allows to observe the structure, the phase distribution and the porosity of the particular fuel cell surface layer [49,89-91,93,94].

Detailed properties of a certain layer and interface can be studied as well by SEM. For the anode, the redox stability of Ni-YSZ composite have been studied [89,93]. Thyden et al. developed a method to improve contrast between Ni and YSZ by using low-voltage SEM [95]. Fine-structured anodes were observed to coarse due to redox cycling, whereas coarse-structured anodes did not [93]. Yan et al. observed that applying SDC interlayer between lanthanum strontium gadolinium magnesium oxide (LSGM) electrolyte and NiO anode prevented unwanted reactions between NiO and LSGM [90]. Sintering procedure have been observed to correlate with the microstructure of YSZ [96] and GDC [97] electrolytes. LSCF-SDC [98] and LSCF-GDC [99,100] cathodes have been studied and coarsening of LSCF during annealing reported [100]. Lee et al. observed a core-shell structure in BSCF-GDC cathodes [49].

TEM allows high-resolution imaging of a fuel cell material nanoparticles [49,89,91,94,99,101] and studying the crystalline orientations via electron diffraction patterns [49,91,99,101]. Elemental mapping has been used to show that GDC interlayer prevents Sr diffusion from LSCF cathode to YSZ electrolyte [88], to study the elemental distribution at LSFC-GDC interface [99], to show that Sn is enriched at the edges of Sn/Ni alloys [94] and to study Si-poisoning [102] and strontium zirconia oxide formation [92] in LSCF cathodes.

Applications on ceramic nanocomposite fuel cells

Due to similarities between SOFCs and CNFCs, many of the microscopy usages mentioned above, such as cross-sectional and surface imaging, are useful in CNFC characterization as well. The composite nature of CNFC electrolytes can be revealed with SEM: SDC-NLKC [31], SDC-NLC [30], GDC-NLC [103] and GDC-KLC [103] all showed separate phases for doped ceria and carbonates. Tang et al. showed that the preparation method of the composite SDC-NLC elec-

trolyte affects to the particle size and shape, partly explaining the electrochemical performance of the particular electrolytes [30]. Asghar et al. compared different cathode materials and observed that LSM-NLC had smaller particle size than LSC-NLC, LSF-NLC and LSCF-NLC [25]. Moreover, fibre-like structures existing in CNFCs have been observed by SEM analysis [25,31]. Origin of these structures is unknown, but they are speculated to be some kind of hydroxides.

Using TEM to analyse nanoparticles of CNFC powders have been reported. Asghar et al. imaged different cathode materials that were aged in CO₂ atmosphere and observed that LSM-NLC cathode showed significant enrichment of Mn at some points characterized with EDX [25]. Rafique et al. imaged SSDC-NC nanoparticles and observed a core-shell structure with ceria cores and carbonate shells [24].

Applications on single-layer fuel cells

For SLFCs, using SEM to get cross-sectional [64-66,68,69] and surface images [63-66,71] have been widely reported. Analyzing the particle size distribution of CSDC [73] and comparing air and fuel sides of LNCZ-SDC-NLC [65] and NCAL-CSDC [69] pellets after characterization have been done with SEM as well. Homogenous distribution of both phases in sub-micron scale has been observed for SSC-SDC [66], LNCS-SDC [63,64], LNMS-SDC [64], LNCoS-SDC [64], LNCS-MZSDC [76], NCAL-SDC-NC [68] and NCAL-CSDC [69] by SEM/EDX.

TEM have been used to image nanoparticles of SLFC materials [61,63,70,71,73]. Zhu et al. studied the interfaces between semiconductor and ionic conductor particles for nickel zinc oxide (NZ) – SDC [61] and LSCF-CSDC [70]. NZ-SDC was shown to consist from larger SDC and smaller NZ particles that formed bulk heterojunctions, whereas for LSCF-CSDC the role of interfacial region between LSCF and CSDC particles for O-movement was highlighted. Wang et al. determined electron diffraction pattern and atomic structure of LSFC-CSDC [73].

Summary

2D-microscopical methods, especially SEM and TEM have been widely applied to characterize SOFCs, CNFCs and SLFCs. The information required by these techniques is crucial to understand the nanoscale properties of these devices and explain their macroscopic performance.

However, both SEM and TEM are limited to two dimensions. Since the fuel cells listed above are complex 3D-structures down in nanolevel, this sets limitations to utilizing these techniques.

3.2.3 3D microscopy

With 2D microscopical methods, such as SEM and TEM, the result is always a 2D projection of a 3D structure. Ability to reconstruct the actual 3D structure can provide more information about e.g. phase distribution, porosity and tortuosity of the studied sample. For SOFCs, two different microscopic techniques,

FIB-SEM and X-ray tomography, have been applied to make 3D-reconstructions. These methods have been shown to be consistent with each other with a good accuracy [104].

FIB-SEM

SEM can be used to image the surface of the sample. In FIB-SEM imaging, the surface is first imaged by SEM and then a thin layer is cut off with FIB. This procedure is repeated until the whole sample is imaged, resulting as a series of 2D images that can be used to reconstruct the initial 3D-structure. FIB-SEM can achieve good resolution: voxel sizes down to 10 nm have been reported [104,105], but it is destructive for the sample.

Wilson et al. demonstrated the power of FIB-SEM in fuel cell research by making a 3D reconstruction of Ni-YSZ anode, shown in Figure 5, and calculating phase fractions, surface areas, triple phase boundary (TPB) density, phase connectivity and tortuosity [106]. Vivet et al. studied the effect of Ni-content to the Ni-YSZ anode microstructure and concluded that 44 % solid volume fraction of Ni was optimal (i.e. it maximized active TPB density) [105]. Iwai et al. investigated different calculation methods (random walk calculation and lattice Boltzmann method) for reconstruction and found them to be consistent [107]. Annealed Ni-YSZ electrodes showed lower TPB-density than fresh ones due to coarsened microstructure [108,109], indicating that reduced TPB is a major factor causing degradation. Kishimoto et al. studied Ni-GDC anodes prepared by Ni-infiltration and powder pressing and observed that infiltrated anodes had eight times larger active TPB density [110].

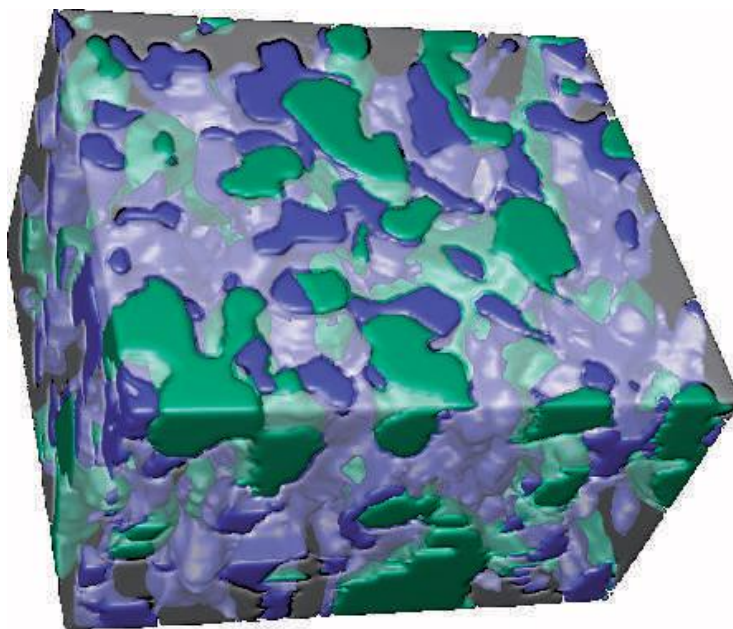


Figure 5. A 3D reconstruction of a Ni-YSZ anode, showing Ni as green, YSZ as translucent or grey and pores as blue. Reproduced from [106] with permission, © Nature Publishing Group.

The key microstructural parameters can be determined for the cathodes similarly to the anodes [104,111]. Smith et al. studied the effect of sintering temperature of LSM-YSZ cathodes to the microstructure and the polarization resistance, and found a connection explaining the electrochemically observed resistances by microstructural differences [112]. Yakal-Kremski et al. showed that under-firing (i.e. sintering at lower temperature) of LSM-YSZ cathodes decreased their vulnerability to degradation [109].

X-ray nanotomography

An X-ray image of a sample provides a 2D-projection in a plane parallel to the direction of the X-ray beam. When a large amount of such images are taken from different angles, a 3D-reconstruction of the sample can be computed. The main benefit of X-ray nanotomography over FIB-SEM is the non-destructivity: same sample can be measured several times. On the other hand, the resolution is lower: voxel sizes of 22-25 nm have been achieved in X-ray nanotomography reconstructions [113-115].

Three-dimensional reconstructions of Ni-YSZ anode [113-117] and LSM-YSZ cathode [104] have been successfully constructed with X-ray nanotomography. Chen-Wiegart et al. showed that the modelled anode polarization resistance based on 3D-reconstruction was consistent with electrochemical measurements [116]. Laurencin et al. found that a minimum volume of $35 \times 35 \times 35 \mu\text{m}^3$ had to be reconstructed to be statistically representative from the whole sample [117]. Shearing et al. utilized the non-destructive nature of X-ray nanotomography and studied the effect of redox cycling to the microstructure [115].

Since SOFCs are operated at high temperatures, the microstructure reconstructed at room temperature may not present the respective structure at operational temperature. Shearing et al. developed an experimental setup allowing to complete X-ray nanotomography for a LSFC cathode at operational temperature (695 °C) [118]. Their experimental setup is presented in Figure 6. They observed a decrease in porosity and an increase in tortuosity when comparing the high-temperature data to the room temperature data.

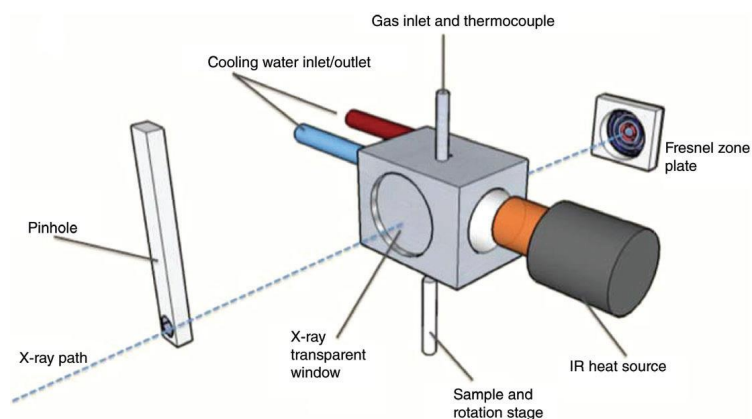


Figure 6. The experimental setup used by Shearing et al. to perform X-ray nanotomography measurements in FC operational conditions. Reproduced from [118] with permission, © ECS.

Summary

3D tomography, utilizing FIB-SEM and X-ray nanotomography methods, provides a unique insight to the SOFC electrode properties, allowing to reconstruct the actual 3D microstructure. Accurate determining of e.g. TPB density, porosity and tortuosity and linking the macroscopic performance to microstructure by using 3D tomography have been reported for SOFC electrodes.

However, since the fuel cells are operated at high temperatures, the room temperature characterization may not be presentative for microstructure in actual operational temperature. Thus advanced setups allowing in-situ characterization of fuel cell materials and even complete fuel cells are required to push the limits of microstructural analysis even further.

3.3 Challenges and gaps in fuel cell research

The previous Subchapters provide a state-of-the-art view on the existing literature and scientific knowledge on CNFCs, SLFCs and methods that can be used to characterize the microstructure of ceramic fuel cells. Although these topics have been studied intensively and the researchers have solved many challenges, there are still significant holes in the scientific knowledge from these fields. Following discussion about the existing gaps in the literature and the challenges that need to be solved concludes this Chapter.

SOFCs are an established research topic that has been an interest of the fuel cell community for decades. This results as a vast number of scientific articles and books handling the topic from different perspectives, providing a good insight to the topic and allowing to identify established manufacturing and characterizations procedures developed during decades, as well as the fundamental limitations for SOFCs.

CNFCs, however, are a more recent innovation. The early work in the CNFC field was published around year 2000, but most of the scientific literature about CNFCs cited in this Thesis is published since 2010. CNFCs are based on SOFC technology and some of the scientific knowledge about SOFCs can be used in CNFC research, but as the SOFC materials are at least partly replaced by new ones and some fundamental mechanisms change (e.g. new ions start to contribute to the charge transfer), new studies are needed to replace the out-of-date knowledge. Characterizing new composite electrolytes that are based on multi-ion conduction instead of just O^{2-} and developing new optimized material compositions and manufacturing methods are crucial to push the CNFCs beyond current state-of-the-art. This observed gap is addressed in Publications II&III.

SLFCs are even more recent innovation that has been researched by the fuel cell community only for a decade. The first SLFC publication that the author is aware of is from 2000 [58] and the major breakthrough occurred in 2011 when Zhu et al. presented their composite material LN-GDC [18]. This highlights the need of basic studies about suitable materials, their characterization and the working mechanisms of SLFCs even more than in case of CNFCs. Publications IV&V are aimed to fill part of this gap. Since the amount of publications in SLFC field is yet relatively low, systematicity and repeatability of the experiments is

a factor requiring attention. Many SLFC publications show data only from a single cell, leaving out any statistical analysis and discussion about repeatability of the experiments. Publication VII is focusing on this issue by a systematic study involving larger number of individual cells, supported by the cells reported in Publication VI.

As the fuel cells are energy conversion devices, commercialization of these technologies, or showing that it is impossible, can be considered as a goal for research. In laboratory-scale experiments, the main factor of interest has been the power density of single small cells. However, from commercial point of view, e.g. fuel efficiency, stability and the potential to up-scale fuel cell power output from mW- and W-level to kW- or even MW-level by using larger cells and cell stacks are also just as important factors. Research focused on these factors needs to be vastly increased to drive these technologies towards commercialization. Especially established procedures for the long-term stability studies of CNFCs and SLFCs are needed to drive them towards commercialization.

2D microscopic methods, as well as XRD, have been widely and successfully applied to the CNFC and SLFC fields. However, 3D tomography of these devices by FIB-SEM and X-ray nanotomography technologies is lacking. Based on the literature review presented in this Chapter, no obvious fundamental reason why 3D tomography could not be applied to CNFCs and SLFCs is detected. However, since FIB-SEM and X-ray nanotomography are advanced and highly sophisticated characterization techniques, performing experiments and analyzing the results requires specialization in these fields. The most likely explanation to why the 3D tomography for CNFCs and SLFCs is missing is the lack of scientists who have enough knowledge on both sides. Filling this gap by making and utilizing 3D reconstructions has potential to improve the properties of CNFCs and SLFCs.

Another issue related to microstructural characterization is the vast difference between microscopic characterization temperature, typically room temperature, and the actual operational temperature of CNFCs and SLFCs, typically 500–600 °C. This raises concerns about how well the room temperature microstructure corresponds to the operational temperature microstructure. Advanced in-situ measurement setups allowing microstructural characterization at the operational temperature can help to fill this gap.

To sum up, the state-of-the-art ceramic fuel cells, starting from SOFCs and advancing to CNFCs and SLFCs have been studied intensively and shown a great potential as clean energy sources, provided that the remaining challenges can be solved. Due to nanoscale complexity of these devices, accurate microstructural characterization is identified as a key method to understand these devices and push them towards commercialization. Several obvious research gaps exist in this field, as discussed in this Subchapter. This Thesis address to some of these gaps, providing scientific knowledge to create base for future work.

4. Materials and methods

This Chapter presents the materials and the experimental methods used in this Thesis. The Chapter is divided into two Subchapters. The first Subchapter focuces on raw materials, material synthesis and mixing and fuel cell manufacturing methods. The second Subchapter presents the experimental techniques and research equipments that were used to characterize fuel cells and nanopowders.

4.1 Materials, synthesis and fuel cell manufacturing

The methods that were used to manufacture complete fuel cells starting from chemicals purchased from commercial sources are presented here. These methods include synthesizing new materials, mixing two or more existing materials and pressing powders into fuel cell pellets.

For some of the presented methods, exact experimental parameters (e.g. sintering temperature and time) have been varied between different Publications (and in some cases even within a single Publication). In this Subchapter, only the principles and general description of the methods are presented. For the exact experimental procedure of a certain experiment, the reader is always referred to the Experimental section of the particular Publication.

4.1.1 Commercial chemicals

The chemicals bought from commercial sources for the experiments reported in this Thesis are presented in Table 2. The chemicals were bought from Sigma-Aldrich. The table presents the name of the chemical, its abbreviation, to what purpose it was used in this Thesis and in which Publication(s) it was used. For consistency, only one logical abbreviation is used for each material in this Thesis. Thus the same chemical may have been mentioned in the literature with different abbreviation.

4.1.2 Material synthesis and mixing

Several methods were used to synthesize new chemicals from the commercially bought raw materials presented in Table 2 and to mix two or more existing chemicals to form a suitable mixture. The descriptions of the synthesis and mixing methods are presented here.

Table 2. The chemicals bought from commercial sources. Name of the chemical, its abbreviation, useage and Publications were it was used are presented. The chemicals were bought from Sigma-Aldrich and used as received unless otherwise stated in the respective Publication. The most commonly used solvents (acetone, ethanol, distilled water) are excluded from the Table.

Chemical name	Abb.	Purpose	Publication(s)
Calcium nitrate tetrahydrate	CNT	Synthesis	III
Cerium nitrate hexahydrate	CNH	Synthesis	III, V
Cerium oxide, gadolinium-doped, 10 mol-%	GDC	Electrolyte, SLFC	II, IV, VI, VII
Cerium oxide, samarium-doped, 15 mol-%	SDC	SLFC	VII
Citric acid	CA	Synthesis	III, V
Copper carbonate basic	CCB	Synthesis	III
Copper iron oxide	CFO	SLFC	V
Ethyl cellulose	EC	Pore former	II, III, VII
Gadolinium nitrate hexahydrate	GNH	Synthesis	V
Glycerol	-	Precursor	IV, VII
Potassium carbonate	KC	Electrolyte	III, VI
Lanthanum strontium cobalt ferrite	LSCF	Cathode	II, III
Lithium carbonate	LC	Electrolyte, synthesis	II, III, IV, VI, VII
Lithium nickel cobalt aluminium oxide	NCAL	Current collector	IV, VII
Lithium nitrate	LN	Synthesis	III
Nickel carbonate basic hydrate	NCBH	Synthesis	III, IV, VI, VII
Nickel oxide	NiO	Anode	II
Polyethylene glycol	PEG	Synthesis	V
Polyvinyl alcohol	PVA	Pore former	II, III
Samarium nitrate hexahydrate	SNH	Synthesis	III, V
Sodium carbonate	NC	Electrolyte, synthesis	II, III, VI, VII
Zinc carbonate basic	ZCB	Synthesis	III
Zinc nitrate hexahydrate	ZNH	Synthesis	IV, VI, VII

Calcination is a general description for a high-temperature treatment of a nano-sized powder. Calcination is done by placing the powder to a suitable container and heating it in the oven to a given temperature. Calcination can be used as a step in synthesis procedure and to purify ready powders. Calcination was used in Publications II-VII.

Grinding is a quick and simple method to mix chemicals that are in powder form. The chemicals are simply put to mortaring bowl, grinded with a pestle for a given time and collected. Grinding was used in Publications II-VII.

Planetary ball milling machine can be used to mix the powders and to reduce the particle size. The powders to be mixed are put to a milling jar either as solids or as mixed to a certain media (e.g. acetone or ethanol) with zirconia milling balls (typically 10:1 weight ratio between milling balls and powder). Then the jar is put to the ball milling machine set to given angular velocity (expressed as RPM, rounds per minute) for given time. If a liquid media is used, the resulting mixture is dried and usually grinded before collecting. Ball milling was used in Publications II-VI.

Solid-route method can be used in both synthesizing and mixing of materials. The raw materials are simply mixed with grinding or ball milling, followed typically by a heat treatment. Solid-route method was used in Publications II-VII.

Co-precipitation is done by dissolving the raw materials to de-ionized water. Then a solution of NC in de-ionized water is added dropwise and the mixture is stirred. The resulting product is a precipitation, which is filtered, washed and dried at low temperature (<100 °C). After drying a high-temperature calcination is applied. Finally the resulting powder is grinded and collected. Co-precipitation was used in Publication III.

Table 3. The chemicals prepared in-house with different synthesis procedures. The solvents and reactants needed for each procedure are excluded from the Table.

Chemical name	Abb.	Method	Raw materials	Publication(s)
Ca, Sm co-doped ceria	CSDC	Co-precipitation	CNH, CNT, SNH	III
Gd, Sm co-doped ceria	GSDC	Sol-gel	CNH, GNH, SNH	V
Lithium nickel copper zinc oxide	LNCZ	Slurry	CCB, LN, NCBH, ZCB	III
Lithium nickel zinc oxide	LNZ	Solid-route	LC, NCBH, ZNH	IV, VI, VII

In slurry method the raw materials are first mixed with CA and de-ionized water, e.g. by ball milling. The mixture is put to a hot plate and stirred, until it forms a slurry. Then a heat treatment and new mixing are applied. Slurry method was used in Publication III.

Synthesizing materials via sol-gel method starts by dissolving the raw materials to de-ionized water. Then CA and PEG in aqueous solution are added slowly and the resulting mixture is stirred until it forms a colorless gel. The gel is dried and grinded. Sol-gel method was used in Publication V.

A summary of the materials synthesized in-house in this Thesis work is presented in Table 3. All nanopowders that were used for fabricating fuel cells are either commercially bought materials (Table 2), in-house synthesized materials (Table 3) or composites that have been prepared by mixing at least two of the materials presented in Table 2 and Table 3 by ball milling and/or grinding. Exact details of the material manufacturing processes for each experiment are presented in the Experimental sections of the respective Publications.

4.1.3 Fuel cell fabrication

The fuel cells reported in the Publications included to this Thesis were fabricated by pressing the nanopowders into pellets by using powder press method once the respective powders were obtained. The general experimental procedure of the powder press method is described below. For details of a certain experiment, the reader is referred to the Experimental section of the respective Publication.

- (i) A metallic die (diameter 13 mm) is assembled.
- (ii) Given amount of powder is weighted and put to die on a small metal cylinder, possibly with e.g. Ni-foam.
- (iii) The powder surface is smoothened by pressing and rotating from above with a large metal cylinder.
- (iv) For multi-layer pellets, the steps (ii) and (iii) are repeated for each layer.
- (v) A high pressure (typically a few hundred MPa) is applied on the die by using a mechanical press.
- (vi) The die is disassembled and the pellet removed.

After pressing, the pellets were densified and strengthened by sintering at high temperature. The exact details of the sintering process were varied between different Publications. Examples of the fuel cell materials during different steps of the manufacturing procedure of a LNZ-GDC SLFC are presented in Figure 7.



Figure 7. LNZ powder before (a) and after (b) calcination. LNZ-GDC pellets (c). The pellet at the bottom right corner is unsintered.

Three different current collectors were used in this Thesis: gold paste, Ni-foam and NCAL-coated Ni-foam. Gold paste was deposited on the pellet surfaces by using a brush, followed by sintering. Since gold paste layer is thin and porous (Publication IV), it is unlikely to have a large effect to the gas diffusion properties. Ni-foams were cut from a larger sheet to match the cell dimensions and pressed with mechanical press before use. NCAL precursor was prepared by adding NCAL to 1:1 by weight mixture of ethanol and glycerol. After the precursor was properly mixed, the resulting paste was painted on Ni-foams, followed by sintering. The exact details on preparing and applying the current collectors for certain experiments can be found from the Experimental sections of the respective Publications.

4.2 Characterization

This Subchapter presents the experimental methods that have been used to characterize the fuel cells and the nanopowders of the fuel cell materials that have been reported in this Thesis. These techniques are divided to microstructural and electrochemical methods.

It should be noted that the Publications included in this Thesis are utilizing some experimental methods that are excluded from this Thesis and thus are not presented here. When information obtained by such methods is utilized, it is always justified by a reference to the respective Publication.

4.2.1 Microstructural characterization

Since both CNFCs and SLFCs reported in this Thesis are consisting of pressed nanopowders, understanding the fine nanostructure and nanoscale properties of both the fuel cells and the powders is important to explain the macroscopically observed performance. A large variety of such techniques have been reported in the literature. In this Thesis, three methods, X-ray diffraction spectroscopy (XRD), scanning electron microscopy (SEM) and transmission electron microscopy (TEM) have been utilized. Moreover, both SEM and TEM have been combined with energy-dispersive X-ray spectroscopy (EDX) to perform an elemental analysis. Detailed descriptions of the working mechanisms of these techniques are presented in Subchapter 3.2.2.

XRD was used in this Thesis to identify the crystalline structure (or the lack of it) of the fuel cell materials and to confirm the success of the material synthesis process. Moreover, HT-XRD was used to study the thermal stability of the nanopowders. XRD measurements reported in Chapter 5 were performed with Rigaku Smarta PAN-alytical X'pert PRO MPD (Publications II, III, IV & V) and Rigaku SmartLab X-ray Diffractometer (Publications VI&VII).

In this Thesis, SEM was a basic tool for characterizing the microstructure of fuel cell pellets. Surface imaging done via SEM was used to study the phase structure and porosity of the pellet surfaces. Another application of SEM was to take cross-sectional images from the pellets to confirm that there are no continuous pores going through the cell and thus allowing direct gas mixing. SEM characterization reported in Chapter 5 was done with the following models: JEOL JEM-7500FS (Publication II), JEOL JSM-7500FA (0.6 nm resolution, Publication II) and Zeiss Sigma VP (Publications III, IV, V, VI & VII).

TEM was applied to image the nanosized powders that were used to press complete fuel cells as described in Subchapter 4.1.3. The particle sizes, crystalline structures and elemental distributions inside a particle cluster are determined and discussed. All TEM images shown in Chapter 5 (originally reported in Publications IV-VII) were taken with high-resolution TEM, model JEOL JEM-2800 (0.1 nm resolution).

Access to Rigaku SmartLab X-ray Diffractometer (XRD), JEOL JEM-7500FS (SEM), Zeiss Sigma VP (SEM) and JEOL JEM-2800 (TEM) was provided by Aalto University Nanomicroscopy Center (Aalto-NMC).

4.2.2 Electrochemical characterization

Since the purpose of the fuel cells in commercial use is to produce electricity, it is relevant to compare different fuel cells to each other by comparing parameters describing their electrochemical performance, especially the power density that is the fraction of the maximum power output and the active area of the cell, i.e.

$$P_d = \frac{P_{out,max}}{A_{cell}}, \quad (4.1.)$$

where P_d is the power density, $P_{out,max}$ the maximum power output and A_{cell} the active surface area of the fuel cell. Besides P_d , also other electrochemical parameters, such as open circuit voltage (V_{oc}) and the internal resistance of the cell at the operational temperature are important factors that describe the performance of the fuel cell. The methods used for electrochemical characterization of the fuel cells in this Thesis are described below.

Experimental setups

Since both CNFCs and SLFCs are operated at relatively high temperatures, the first requirement for the successful electrochemical characterization of these devices is an experimental setup that allows heating to the operational temperature (between 500 and 600 °C for most of the fuel cells reported in this Thesis) and applying the suitable gas atmosphere, typically H_2 on one side and air on the other. This requires an oven, a chamber for the fuel cell, separate gas lines

for H_2 and air (and gas insulation between them) and suitable electrical contacts from the fuel cell to the measurement device. Three different experimental setups have been used in the Publications included in this Thesis. A description of the setups is given in the Experimental sections of the respective Publications. A four-point connection for characterization devices was used in each setup.

The active areas of the cells varied between 0.50 and 0.64 cm^2 . The active area was determined by observing the area exposed to gases after experiment (Publications II-V) or by using the experimental setup to limit the gas flows to certain areas (Publications VI&VII).

Current – voltage characterization

Current - voltage (IV) characterization is a simple but powerful tool that gives access to several important electrochemical parameters of a fuel cell with quick measurement and analysis. A single datapoint of IV-curve is measured by applying an external voltage to the cell and measuring the resulting current or vice versa: applying current and measuring voltage. The former approach is called potentiostatic and the latter galvanostatic. This is repeated over a range of voltages (or currents) with a certain step size. Typically the range of the IV-curve is chosen so that at least V_{OC} and the maximum power point (MPP) are included in the measurement. Very high current densities are sometimes avoided since they may damage the cell or the measurement setup, but in this case direct determination of the short-circuit current (I_{SC}) is not possible. IV-curve can be measured also outside $V_{OC} - I_{SC}$ range, but in this case the device is not operating as a fuel cell. However, such measurements can be useful when studying the fundamental electrochemical properties of the FC materials.

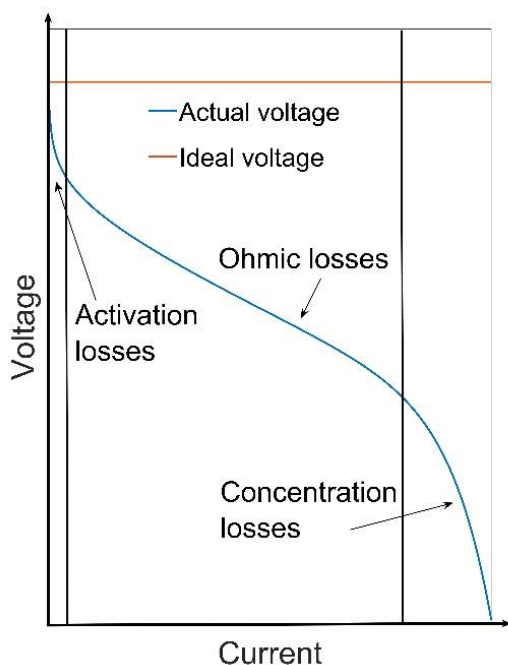


Figure 8. A theoretical IV-curve of the fuel cell. The curve is divided into three sections based on the dominating loss factor: activation, ohmic and concentration.

An example of IV-curve of a fuel cell is presented in Figure 8 (as illustration). The theoretical maximum voltage depends on the total FC reaction potential that can be calculated from thermodynamics, but the actual V_{OC} is slightly lower due to irreversible losses [3]. When the current is drawn from the cell, there is a rapid initial voltage drop, related to electrode reaction kinetics (activation losses). In the middle region, the curve is rather flat since the only major current-depending voltage loss factor is the ohmic loss (mainly due to limited ionic conductivity). At very high currents, the voltage drops to zero rapidly due to concentration losses. This can be caused by e.g. depletion of the fuel or oxidant gas. The loss mechanisms are described in more detail in [3].

The shape of an IV-curve of a certain FC strongly depends on what of the loss mechanisms described above are dominating. For example, if the ohmic losses of the cell are large enough to reduce the voltage to zero so that the concentration losses are still insignificant at I_{SC} , the concentration loss region shown in Figure 8 cannot be observed from the IV-curve.

V_{OC} and I_{SC} can be seen directly from the IV-curve (assuming that they are included in the measurement range), whereas its shape allows to qualitatively analyze which loss mechanisms are limiting the fuel cell performance. The power output of the cell can be determined by calculating power output for each datapoint and plotting the result as current – power (IP) curve. The total resistance of the fuel cell at a certain voltage can be calculated from the slope of the IV-curve at that point. The active area of the cell can be taken into account by replacing the current with the current density in the plots, allowing to compare fuel cells with different active areas to each other.

In this Thesis, the IV-data is measured with potentiostatic mode. The main justification for that is that the V_{OC} :s of the studied fuel cells are in the same range (around 1 V) but the supported currents differ significantly. Thus, potentiostatic mode allows measuring different FCs with equal experimental settings (e.g. voltage range, slew rate). The data is presented by plotting both voltage and power density as a function of current density, that is a common way to present IV- and IP-data in fuel cell literature. This plotting format allows to easily read power density and V_{OC} from the plot and to perform comparison if data from multiple IV-measurements is presented in a single plot.

All IV-measurements reported in this Thesis were performed with Zahner Zennium potentiostat.

Electrochemical impedance spectroscopy

Electrochemical impedance spectroscopy (EIS) is a sophisticated characterization technique that allows to break down the total resistance of a fuel cell to its individual components. This helps to identify which loss mechanisms are the most crucial ones for the cell performance.

EIS is done by applying a voltage that consist of direct and alternating components (V_{DC} and V_{AC} respectively) and by measuring the cell response, impedance (Z) [3,119]. In this Thesis, the EIS-spectra were measured in open circuit condition, i.e. $V_{DC} = V_{OC}$, that is a typical procedure in CNFC and SLFC literature. Typical amplitude for V_{AC} was 20 mV. The spectra were measured over a wide range of V_{AC} frequenciens, typically from 100 kHz to 100 mHz.

There are several ways to present EIS-data. In this Thesis, all EIS-data is presented as Nyquist plots, where the real part of the impedance (resistance) is plotted on x-axis and the negation of the imaginary part of the impedance (reactance) on y-axis. Before plotting, the values are converted from impedance to area-specific impedance (i.e. from Ω to $\Omega\cdot\text{cm}^2$). In this plot, the intersection of the spectrum and the x-axis at the high-frequency end (left end) determines the ohmic resistance (that can be considered to result from ion conduction if the current collectors are working properly), whereas the polarization resistance appears as semicircles that are typically at least partly melted to each other [3,119].

An example of (ideal) EIS-spectrum is presented in Figure 9a and an equivalent circuit that can be used to fit the EIS-data for a CNFC in Figure 9b. The total measured impedance is divided into four components: R_o is the ohmic resistance of the cell (due to ion conduction through the electrolyte) and each of parallel connected resistor (R) / capacitor (C) pairs represents impedance occurring from a mass or charge transfer process (e.g. electrode polarization loss). Together these R/C pairs form the polarization resistance of the cell. In this ideal case it is assumed that there are no other factors (such as inductance from the measurement setup) that affects to the EIS-spectrum.

The impedance of parallel R/C pair is:

$$Z = \left(\frac{1}{R} + j\omega C \right)^{-1} \quad (4.2)$$

where $\omega = 2\pi f$ is the angular velocity and j is the imaginary unit [3]. From Eq. (4.2) it can be concluded that at limit $\omega \rightarrow 0$, $Z \rightarrow R$ and at the limit $\omega \rightarrow \infty$, $Z \rightarrow 0$. Between the two extremes, the R/C pair has both resistance and reactance. In Nyquist plot this appears as a semicircle with a diameter R and the peak located at the frequency corresponding to the time constant of the element. For a R/C pair, time constant $\tau = RC$ [120] and the corresponding frequency $\omega = 1/(RC) = 1/\tau$ [3]. If different loss processes have different enough characteristic frequencies, the respective semicircles appear separately, allowing to determine individual resistances by fitting the parameters presented in the equivalent circuit to the measured data. Identifying the loss mechanism that a semicircle is related can be done by using literature (if the time constants are reported) or experimentally, e.g. by changing one parameter in the cell manufacturing procedure and studying its effect on the EIS-spectrum.

From the ideal EIS-spectrum (Figure 9a) the values for the resistances presented in Figure 9b can be read directly: $R_o = 1 \Omega\cdot\text{cm}^2$, $R_1 = 0.5 \Omega\cdot\text{cm}^2$, $R_2 = 1 \Omega\cdot\text{cm}^2$ and $R_3 = 0.5 \Omega\cdot\text{cm}^2$. The capacitances could be determined based on the respective resistance and the frequency of the semicircle peak if this frequency is known.

In real world experiments, ideal capacitors are often not the best possible components to describe the modelled device. Thus constant phase elements (CPEs), that are imperfect capacitors, are often used in equivalent circuits (Figure 9c). Moreover, the polarization part of EIS-spectrum typically consists of semicircles that are melt together partly or completely. In this case, the total polarization resistance is smaller than the sum of its individual components. For partly

melted semicircles, a suitable software can be used to separate different resistor values. For completely melted semicircles separation requires advanced computational methods, such as distribution of relaxation times (DRT). In DRT analysis, the EIS-spectrum is modelled (theoretically) with a circuit consisting of ohmic resistance and an infinite number of R/C pairs with a continuous distribution of τ :s (in practical applications a large number of R/C pairs with τ :s close to each other is used instead). By plotting the obtained distribution of relaxation times as a function of τ the characteristic frequencies of the loss processes can be identified. More detailed descriptions of DRT analysis and its applications in the FC field are given in [120-122].

All EIS-measurements reported in this Thesis were performed with Zahner Zennium potentiostat.

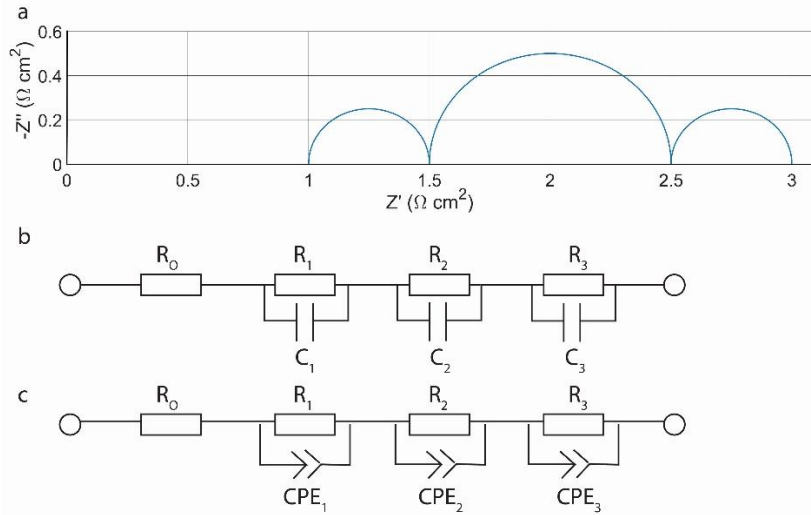


Figure 9. An ideal EIS-spectrum (a) and a respective an equivalent circuit (b) for a fuel cell. R_0 is the ohmic resistance and each of R_n / C_n ($n = 1, 2, 3$) pairs represents an impedance loss occurring from charge transfer or mass transfer process. In reality, CPEs are often used instead of ideal capacitors to get a more realistic model of the actual device.

5. Results

This Chapter summarizes the most important results from the Publications included in this Thesis. The first Subchapter is focusing on three-component CNFCs, based on Publications II&III and RQ2. The second Subchapter analyzes the working principles of SLFCs, initially reported in Publications IV&V focusing on RQ3. The third Subchapter studies systematically the factors affecting to the SLFC performance (Publications VI&VII, RQ4). In all three Subchapters both electrochemical (IV, EIS) and microstructural (XRD, SEM, TEM) methods are reported. Detailed description of these characterization techniques is given in the previous Chapter.

The focus of the experimental work reported in this Thesis was to determine the maximum power outputs of the studied cells and to investigate the links between electrochemical performance and cell microstructure. Thus some relevant research topics, most importantly the long-term stability and fuel efficiency of the studied cells, were left for future work.

5.1 High-performance three-layer fuel cells with composite electrolyte (Publications II&III, RQ2)

Lowering the operational temperature of SOFCs helps to solve challenges related to cell degradation and widens the field of applications. In traditional SOFCs, the ionic conductivity of the electrolyte is the critical factor for operational temperature: if the cell is operated at too low temperature, the ohmic losses are too high for sufficient electrochemical performance [5,6]. Thus, developing new electrolyte materials that have a sufficient ionic conductivity at lower temperatures have been under intensive research [16,17].

One approach is to mix doped ceria with alkali carbonates to create composite electrolytes that have multiple ion conduction channels above the melting point of the carbonate mixture. The effect of this multi-ion conduction is shown in Figure 10 that shows Arrhenius plot (logarithm of conductivity as a function of inverted temperature) of an electrolyte pellet consisting of GDC and NLC (3:1 by weight). The plot shows three separate regions. At low temperatures, the plot is linear since the NLC is in solid state and thus the only ion conduction mechanism is the O^{2-} -ion conduction through the GDC phase that is improved when the temperature is increased. Around 500 °C, the conductivity shows a major improvement. This results from the melting of NLC that creates new parallel ion conduction channels. At high temperatures the plot is again linear.

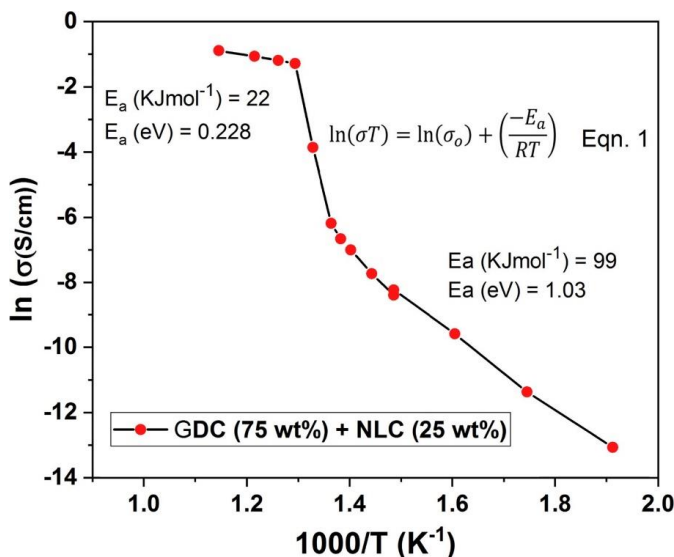


Figure 10. Arrhenius plot showing the natural logarithm of the ionic conductivity of GDC-NLC electrolyte as a function of inverted temperature. The non-linear change around 500°C can be explained by the melting of NLC and transferring from single-ion to multi-ion conduction. Reproduced from Publication II by using author rights, © Elsevier.

The effect shown in Figure 10 allows developing high-performing CNFCs with an operational temperature range of $500 - 600^\circ\text{C}$ by using a doped ceria – alkali carbonate mixture nanocomposite electrolyte. This approach was used successfully in Publications II&III with two different electrolyte compositions. In Publication II, the composite electrolyte consisted of a single-doped ceria and a binary carbonate (GDC-NLC). NiO and LSCF were used as anode and cathode material respectively. In Publication III a co-doped (Ca, Sm) ceria was mixed with a ternary carbonate (CSDC-NLKC). LNCZ and LSCF were used as anode and cathode materials. The melting points for the carbonate mixtures have been determined via differential scanning calorimetry (DSC): 497°C for NLC (Publication II) and 393°C for NLKC [31].

The maximum power density at 550°C determined from IV-measurements was almost similar for both NiO-(GDC-NLC)-LSFC and LNCZ-(CSDC-NLKC)-LSCF cells, slightly over 1 W/cm^2 (Figure 11a-b). Also the ohmic resistances determined from the EIS plots (Figure 11c-d) were very similar: $0.23 \Omega\text{-cm}^2$ and $0.24 \Omega\text{-cm}^2$ for the NiO-(GDC-NLC)-LSFC and LNCZ-(CSDC-NLKC)-LSCF cells respectively. These values are so close to each other that the two cells can be considered as equals in terms of power output and ohmic resistance with a good accuracy. Also, the IV-curves are rather linear, indicating that the ohmic losses are the dominating loss factor.

The sum of polarization resistances determined from the EIS-plots was significantly higher for the NiO-(GDC-NLC)-LSFC cell. Interestingly, this does not lead to lower overall performance. It should be noted that the EIS-curve is measured under open circuit condition, i.e. the total resistance determined from the EIS-spectrum tells the slope of the IV-curve at V_{oc} and the slope can change significantly as a function of current (Figure 8). If there exists e.g. activation

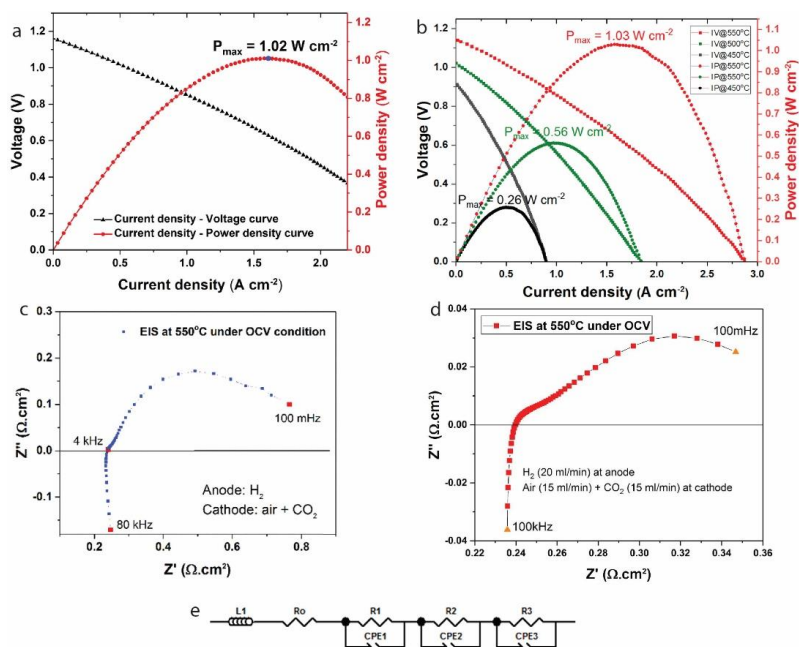


Figure 11. IV- and PV-curve of the NiO-(GDC-NLC)-LSCF cell at 550 °C (a) and the LNCZ-(CSDC-NLKC)-LSFC cell at 450 – 550 °C (b). Respective EIS-plots at 550 °C under open circuit condition (c&d) and the equivalent circuit that was used to fit the EIS-data (e). Reproduced from Publications II (a&c) and III (b&d) by using author rights, © Elsevier.

losses that are relevant only very close (few mV) to the V_{OC} , that would explain the EIS-spectrum in Figure 11c. With the LNCZ-(CSDC-NLKC)-LSCF cell this phenomenon is not observed and the total resistance of the cell determined from the EIS-data at V_{OC} represents well the slope of the IV-curve near maximum power point within a reasonable accuracy.

LNCZ-(CSDC-NLKC)-LSCF cell was characterized at three different temperatures (450, 500 and 550 °C) and it was observed that the V_{OC} of the cell increased significantly when temperature was increased (Figure 11b). The theoretical reversible voltage, calculated based on the Nernst equation, decreases slightly when the temperature is increased [3]. Thus it can be concluded that at lower temperatures some other factor, e.g. insufficient electrode activity, causes significant voltage losses.

XRD was used to determine the crystalline properties of the nanocomposite GDC-NLC (3:1 by weight) nanopowder. The XRD spectrum is presented in Figure 12. The peaks resulting from the crystalline GDC lattice are clearly visible in the figure, indicating a clear and well-formed crystal structure without any significant impurities. Respective Miller indices are given in parentheses. The NLC-peaks can barely be seen from the figure as the signal is extremely weak compared to the background noise. This indicates that the alkali carbonates are mostly in amorphous state instead of a crystal lattice.

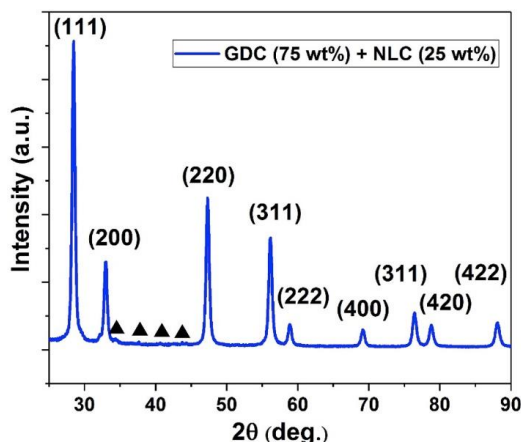


Figure 12. XRD-spectrum of nanocomposite electrolyte powder GDC-NLC. GDC-peaks are indexed, NLC-peaks marked with black triangle. Reproduced from Publication II by using author rights, © Elsevier.

SEM was used to study the fuel cell pellets by imaging the pellet surface and the cross-sectional view. SEM images from LNCZ electrode and CSDC-NLKC electrolyte pellet are presented in Figure 13. The electrode (Figure 13a) shows a clear crystal phase with significant amount of pores that are necessary for proper electrode performance. The electrolyte (Figure 13b) shows a dense dual-phase structure: crystalline CSDC and amorphous NLKC. This is consistent with the XRD-results obtained from the composite GDC-NLC electrolyte powder in Publication II. Similar dual-phase electrolyte structure was revealed by SEM-analysis also in Publication II.

Mixing alkali carbonates to doped ceria was successfully completed in two different configurations. Improved conductivity of the composite electrolyte allowed to manufacture CNFCs that yielded power densities of about 1 W/cm^2 at 550°C . Microstructural analysis confirmed porous electrode and dense dual-phase electrolyte structures.

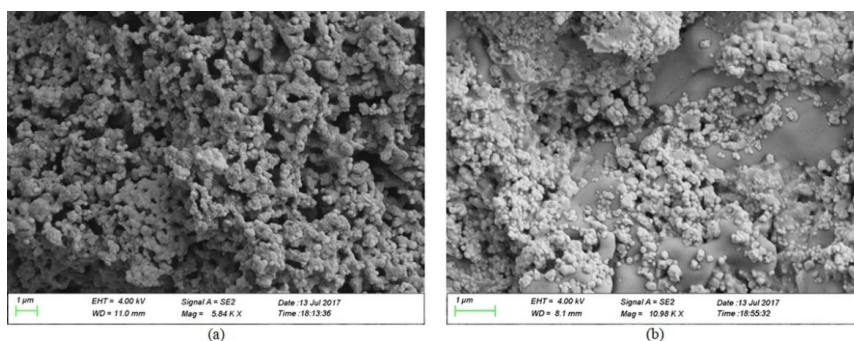


Figure 13. Surface image of LNCZ electrode (a) and CSDC-NLKC electrolyte pellet (b). Scale bar length is $1 \mu\text{m}$. Reproduced from Publication III by using author rights, © Elsevier.

5.2 Single-layer fuel cells based on lithium nickel zinc oxide, copper iron oxide and doped ceria (Publications IV&V, RQ3)

In SLFCs, the traditional three-layer structure of a fuel cell is replaced with a single functional layer that supports both electrode reactions and allows ion transportation through the cell. This eliminates the need of matching thermal expansion coefficients and allows to simplify the manufacturing process. Typically this single-layer material is a composite consisting of electronic or semiconductor and ionic conductor [16,17]. Understanding the working principles and material requirements for SLFCs is crucial for further development of these devices in terms of power density and long-term stability.

The contribution of H^+ and O^{2-} ions to the charge transfer process in LNZ-GDC based SLFCs was studied in Publication IV by measuring IV-curves of the cells in a large voltage range (from 4 V to -4 V) under different atmospheres. The large voltage range was chosen to be able to determine if there exists non-linearity at high voltages, indicating formation of p-n or Schottky-junctions [38]. In normal fuel cell operational conditions (H_2 on one side, air on other) both of these ions participate to the charge transfer and the device acts as a fuel cell when voltage is between 0 V and V_{OC} . Outside this voltage range the FC is behaving like a resistor. The total resistance of the cell, consisting of the ion transport through the cell and the polarization resistance due to electrode reactions can be read from the slope of the IV-curve. When either H_2 or air is replaced by N_2 atmosphere, the respective ion is no longer available and the charge transfer is done via single-ion conduction (assuming that H^+ and O^{2-} are the only ions participating to charge transfer in fuel cell operation conditions). Figure 14a-c shows the IV-curves under H_2 /air, H_2 / N_2 and air/ N_2 atmospheres, respectively. The total resistances of the cells determined from the slopes of the IV-curves are much higher in air/ N_2 atmosphere than in H_2 / N_2 atmosphere, indicating that the H^+ ion is the dominating charge carrier through the cell. However, since the effect of the electrode reactions is not separated, this analysis is only qualitative. When the thickness of the cell is increased, the resistance increases, but not always lineary, as can be seen from Figure 14a-c. This highlights that, besides ionic conductivity, there are also other factors that have significant contribution to the slopes of the presented IV-curves.

Figure 14e shows the effect of current collector to the LNZ-GDC cell performance. The best cell characterized with passive Au as current collector yielded a power density of 360 mW/cm² at 550 °C, but when the current collector was changed to NCAL-coated Ni-foam, the power density for the best device jumped to 800 mW/cm². Since Au has been widely used as current collector in high power density fuel cells, it seems unlikely that this improvement can be explained by improved current collection only.

A more likely explanation to the performance improvement originates from the pellet microstructure. The SLFC pellets have to be dense to prevent the direct gas mixing through the cell. This limits the amount of potential reaction sites at the edges of the pellets due to insufficient porosity. As a catalytically passive material, Au current collector does not provide any extra reaction sites for the electrode processes. However, when catalytically active NCAL, that has

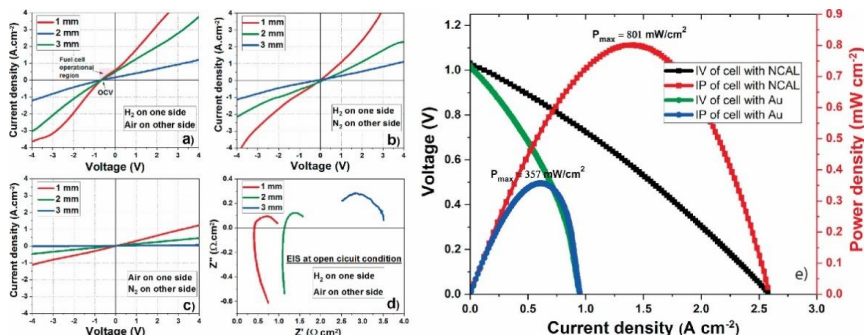


Figure 14. IV-curves of 1 mm, 2 mm and 3 mm thick LNZ-GDC SLFCs under different atmospheres from 4 V to -4 V (a-c). EIS-spectrum under open circuit condition (d). IV- and PV-curves of the best devices with Au and NCAL current collectors (e). Reproduced from Publication IV by using author rights, © Elsevier.

been used as the electrode component in the single-layer composite material [69,71], deposited on porous Ni-foams is used as current collector, the electrode reactions may occur also in the current collector layer or at the interface of the current collector and the cell. In this case the NCAL-coated Ni-foams are acting as electrodes and the single-layer LNZ-GDC as an electrolyte. Similar conclusions has been made in [37,73].

This explanation is supported by the shape of the IV-curves in Figure 14e. With Au current collectors, there is a steep drop in the voltage at high current densities, indicating that there exists significant concentration losses. With Ni-NCAL current collector, the IV-curve is rather linear (although it is slightly curving down at high current densities), indicating that the concentration losses are negligible. If the amount of potential reaction sites is indeed the performance-limiting bottleneck in for the LNZ-GDC cell with Au current collector and this issue is solved by replacing Au with Ni-NCAL that would explain the shapes of the IV-curves of the respective cells.

SLFCs based on copper iron oxide (CFO) and Gd, Sm co-doped ceria (GSDC) were fabricated and characterized in Publication V. Here the focus was especially on studying the effect of sintering temperature to the cell performance. Identical CFO-GSDC cells were sintered at five different temperatures: 600, 700, 800, 900 and 1000 °C.

Figure 15a shows the IV- and IP-curves of the cells sintered at different temperatures. The cell sintered at 600 °C suffers from low OCV and high resistance. Based on this data it seems that 600 °C is too low sintering temperature for proper densification of the cell. If the cell is too porous after sintering, it may, to some extent, lead to direct gas mixing through the cell that will result in low voltage.

The cell sintered at 700 °C showed the highest power density, 340 mW/cm². The EIS-spectrum revealed reasonable ohmic resistance (around 0.4 Ω·cm²) and low polarization resistance (less than 0.2 Ω·cm²). The EIS-data is shown in Figure 15b. When the sintering temperature was increased even further, the power density dropped from the value achieved with 700 °C sintering. However, the cells sintered at 800, 900 and 1000 °C performed significantly better than the cell sintered at 600 °C.

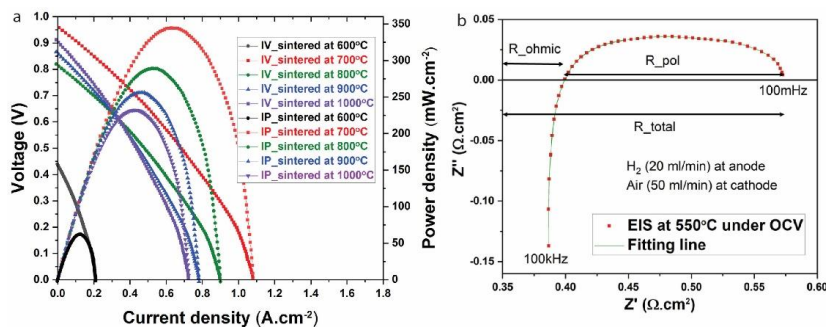


Figure 15. IV- and IP-curves of five CFO-GSDC cells sintered at different temperatures at 550 °C (a). The EIS-spectrum of the best cell (sintered at 700 °C) under OCV (b). Reproduced from Publication V by using author rights, © Elsevier.

In all studied cells, the IV-curve is first linear and shows a rapid drop at the high-current end. This indicates that concentration losses are occurring. When comparing the cells sintered at 700-1000 °C, the rapid drop in voltage occurs at lower current densities in cells that were sintered at higher temperatures. This further supports the claim that too high sintering temperature causes too high densification and thus is reducing the cell performance.

Based on this analysis 700 °C is identified as the optimal sintering temperature for CFO-GSDC cells. This temperature is high enough to support proper sintering process and densification of the cell, but not too high to cause unwanted changes to the cell microstructure, such as too dense structure and low porosity, that may result as weaker cell performance.

The XRD-spectrum of GSDC is presented in Figure 16. The spectrum is very similar than the one presented in Figure 12 for GDC-NLC: the peaks resulting from doped ceria are at the same places.

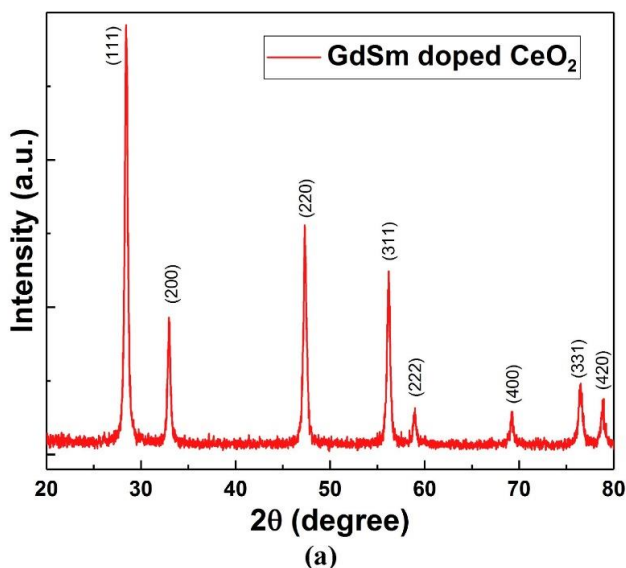


Figure 16. XRD-spectrum of GSDC sample. Reproduced from Publication V by using author rights, © Elsevier.

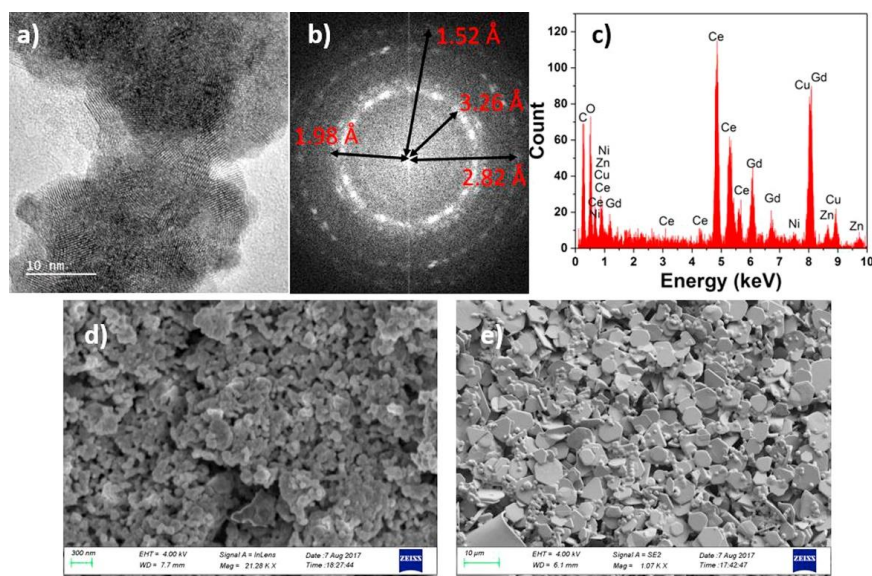


Figure 17. Microscopic analysis of LNZ-GDC. A HR-TEM image of the powder (a), its fast Fourier transform (b) and elemental analysis (c). A surface image of LNZ-GDC pellet before (d) and after (e) applying Au current collector. Reproduced from Publication IV by using author rights, © Elsevier.

Figure 17 presents SEM, TEM and EDX analysis done to the LNZ-GDC sample. TEM imaging (Figure 17a&b) shows the crystalline orientations and lattice spacing's of the sample. EDX (Figure 17c) confirmed the existence of expected elements. SEM showed rather dense structure of SLFC pellet (Figure 17d) and the porosity of the Au current collector (Figure 17e).

Figure 18 shows SEM and TEM images of the CFO-GSDC pellet (a) and CFO nanopowder (b) respectively. The figure reveals that the CFO powder consists of round nanoparticles which diameters are in range of dozens of nanometers. The particles tend to form clusters that appear black in the figure since they are too thick for electron transparency. When pressed into pellet, the CFO-GSDC forms a dense structure with varying particle and particle cluster sizes.

Two different material combinations, LNZ-GDC and CFO-CSDC, were successfully used to fabricate SLFCs. The key findings include that in the LNZ-GDC configuration, the H^+ ion was observed to dominate the charge transfer process over O^{2-} ion at 550 °C. Using NCAL-coated Ni-foams as current collectors more than doubled the cell performance. This is likely due to catalytic activity of NCAL and porosity of the Ni-foams: the porous current collectors start to work as electrodes and it is assumed that the electrode reactions occur at least partly in the current collector. Although the performance is increased, it is questionable are these devices really SLFCs, since all fuel cell reactions are not occurring in the single-layer.

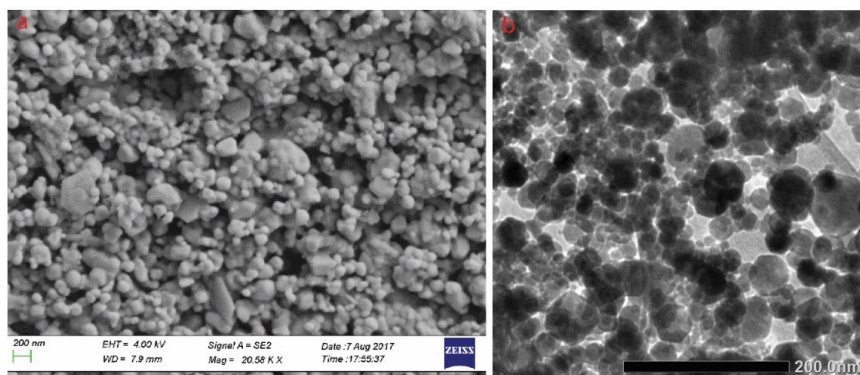


Figure 18. SEM image of CFO-GSDC pellet (a), showing a dense surface structure and various particle sizes. TEM image of CFO nanopowder (b), showing the circular shape of CFO particles and a large variation in particle size. Reproduced from Publication V by using author rights, © Elsevier.

For CFO-GSDC cells, the sintering temperature of the pellets was observed to have huge effect to the cell performance. This can be explained by the effect of sintering to the cell microstructure: the material is densified during the sintering and this effect is stronger at higher temperature. Thus too low sintering temperature can result as a gas leakage through the cell, whereas too high sintering temperature can reduce the amount of reaction sites at the edges of the cell. 700 °C was observed to be the best sintering temperature for CFO-GSDC material.

5.3 Factors affecting power output of LNZ-based single layer fuel cells (Publications VI&VII, RQ4)

Since SLFCs are a rather recent innovation, the amount of systematic studies attempting to link the manufacturing and characterization details to the cell properties is relatively low. The experiments presented here aimed to analyze systematically how ionic conductor composition, porosity, current collector material and mass ratio of semiconductor and ionic conductor affect the power output of the LNZ-based single layer fuel cells.

Figure 19 shows the electrochemical data from eight different LNZ-based SLCFs. The varied parameters were the dopant of ceria (10 mol-% Gd vs. 15 mol-% Sm), the current collector material (Ni-foam vs. NCAL-coated Ni-foam, marked with tag “-NCAL”) and the ionic conductor composition (pure doped ceria vs. 3:1 by weight mixture of doped ceria and NLC, noted with tag “-NLC”). All cells were characterized at 500, 550 and 600 °C under two different gas flow rates. The best IV-curve and respective EIS-spectrum are shown for each cell.

The reference cells (LNZ-SDC and LNZ-GDC) show weak electrochemical performance (Figure 19a) due to high ohmic resistance (Figure 19c). However, when a composite ionic conductor including NLC is applied, the cell performance increases dramatically, mainly due to a reduction by a factor of five in the ohmic resistance (Figure 19b). Applying NLC obviously improves the ionic conductivity of the cells, leading to a major performance improvement.

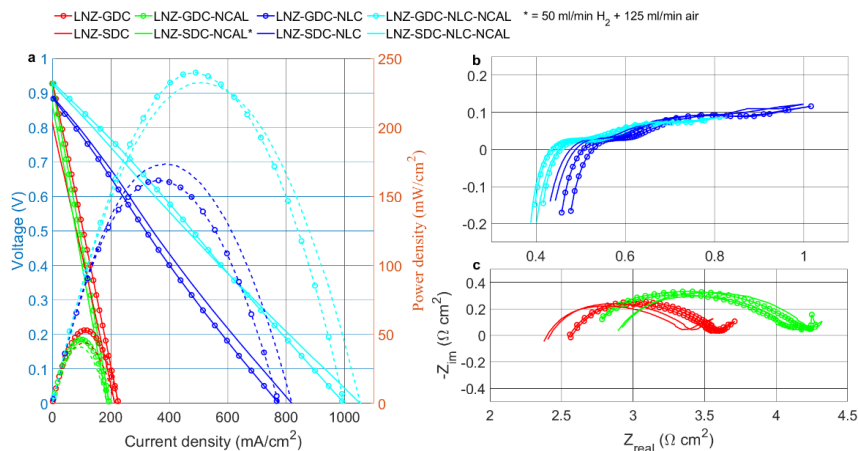


Figure 19. IV- and IP-curves of eight LNZ-(varying ionic conductor) cells (a) and respective EIS-spectra (b-c). The best IV-curve and EIS-spectrum with similar conditions was chosen for each cell. The temperature is 550 °C for NLC-containing cells and 600 °C for non-NLC cells. Gas flow rates: 100 ml/min H₂ and air unless otherwise stated. Reproduced from Publication VII by using author rights, © Elsevier.

Applying NCAL to current collector gave different results depending on whether the cell contained NLC or not. For NLC-containing cells, the performance was improved significantly (e.g. with LNZ-(SDC-NLC) adding NCAL improved performance from 170 mW/cm² to 230 mW/cm²). Qualitative analysis of the EIS-plot (Figure 19b) showed that this is likely due to a reduction of polarization losses. This is consistent with the hypothesis that NCAL-coated Ni-foams can indeed act as electrodes.

However, with non-NLC cells the performance actually decreased slightly when NCAL was applied. EIS-plot (Figure 19c) shows a small increase in both ohmic and polarization losses. It appears that due to high ohmic resistance of the reference devices the benefit of applying NCAL to improve electrode reactions cannot be utilized. There is no obvious explanation to why the performance decreased slightly.

The cells where only difference was the identity of the ceria dopant were observed to behave almost identically. In all four cases the performance differences were very small and no systematic behaviour in favour of either Sm or Gd was observed. This was expected since Sm³⁺ and Gd³⁺ ions have equal charges and their sizes are close to each other. It should be noted that the dopant level was 10 mol-% for GDC and 15 mol-% for SDC, but this difference does not seem to be significant for the cell performance either.

The mass ratio between the semiconductor and ionic conductor is an important factor for the SLFC performance. Sufficient amount of ionic conductor is required to have continuous and relatively straight ion conduction pathways through the cell, whereas the semiconducting material with electrode properties is important to support electrode reactions at the edges of the cell. A typical mass ratio used in the literature is 40 weight-% semiconductor and 60 weight-% ionic conductor [63,65,66,68,71]. However, also 3:7 mass ratio have been reported to be optimal with some material combinations [67,69,74].

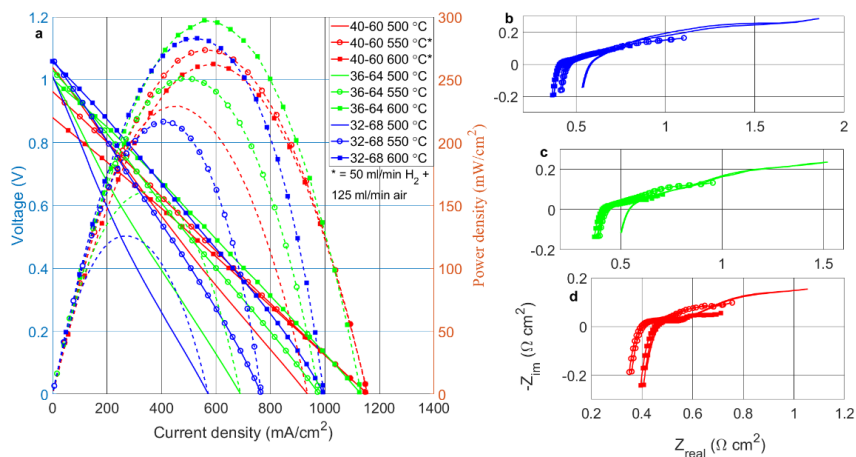


Figure 20. IV- and IP-curves of three LNZ-(SDC-NLC) cells with NCAL-coated Ni-foams as current collectors (a) and respective EIS-spectra (b-d). The best IV-curve and EIS-spectrum with similar conditions was chosen for each cell. Gas flow rates: 100 ml/min H_2 and air unless otherwise stated. Reproduced from Publication VII by using author rights, © Elsevier.

Since the NCAL-coated Ni-foam that was used as a current collector in the best cells presented in Figure 19 is a catalytically active material that boosts the electrode reactions and can even act as an electrode, optimal mass ratio between LNZ and ionic conductor may differ from the literature standard in this experiment. Three cells with LNZ semiconductor, SDC-NLC ionic conductor and NCAL-coated Ni-foams as current collectors were fabricated and analyzed to study how the mass ratio between LNZ and SDC-NLC effects the performance of the cell at different temperatures. The electrochemical data is presented in Figure 20.

At 500 °C, the traditional 40-60 (40 weight-% LNZ and 60 weight-% SDC-NLC) has superior performance, most likely due to insufficient electrode reaction rates of the 36-64 and 32-68 cells, indicated by the long tails of the respective EIS-plots (Figure 20b-d). At 550 °C, the 40-60 cell is still the best one, but the performance differences are significantly smaller than at 500 °C due to a larger relative improvement in the 36-64 and 32-68 cells than in the 40-60 cell. At 600 °C, the highest power density (300 mW/cm²) is achieved with the 36-64 cell (power densities of the 32-68 and 40-60 cells at 600 °C were 280 and 260 mW/cm² respectively). It should be noted that with the 40-60 cell shown in Figure 20 and the NLC-containing cells shown in Figure 19 the top performance was reached at 550 °C, whereas with the 36-64 and 32-68 cells presented in Figure 20 the power density improved from 550 °C to 600 °C.

Besides the factors analyzed in Figure 19 and Figure 20, the effect of implementing an external pore former (ethyl cellulose, EC, 5 weight-%) to the LNZ-SDC and LNZ-(SDC-NLC) powders was studied. This was expected to increase the porosity of the pellets due to evaporation of EC during the sintering process. Increasing porosity should increase the surface area of the pellet and thus improve the electrode reaction rates. Since the entire pellet is consisting of a single-layer, the increased porosity should also increase the ohmic resistance (due

to twisting of ion conduction pathways as the share of ionic conductor in the nanocomposite mixture is decreased).

The cell performance was observed to drop by 15 – 24 % when EC was applied in all four studied cases. With the best-performing combination (LNZ-SDC-NLC-NCAL) the maximum power density achieved decreased from 230 mW/cm² to 190 mW/cm². This was shown via EIS-measurements to be due to increase in ohmic resistance when EC was applied. No evidence of improved electrode performance or gas mixing due to EC was found. The IV- and IP-curves of the respective cells can be found from Supplementary Information of Publication VII.

In another experiment two LNZ - (nanocomposite ionic conductor) cells were fabricated and characterized. Two different ionic conductors were used: GDC-NLKC (7:3 by weight) and GDC-NLC (3:1 by weight). Au paste was used as current collector for both cells. The mass ratio of the single-layer powder was 40 weight-% LNZ and 60 weight-% ionic conductor. The resulting electrochemical data is presented in Figure 21.

As the data shows, there is a large difference in the cell performance in favour of the ternary carbonate (Figure 21a&c). The top performance of the LNZ-(GDC-NLKC) cell was 580 mW/cm² at 600 °C, whereas the LNZ-(GDC-NLC) cell yielded 240 mW/cm². The large difference can be explained by the lower ohmic resistance of the LNZ-(GDC-NLKC) cell when compared to the LNZ-(GDC-NLC) cell (Figure 21b&d). This results from two factors. Due to the lower melting temperature (393 °C for NLKC [31] vs. 497 °C for NLC (Publication II)) and higher carbonate content in the respective ionic conductors (30 weight-% NLKC vs. 25 weight-% NLC), the ionic conductivity per unit length was higher for the LNZ-(GDC-NLKC) cell. Also, the LNZ-(GDC-NLKC) cell was only 1 mm thick, whereas the thickness of the LNZ-(GDC-NLC) cell was 1.5 mm. As a result the ohmic resistance of the the LNZ-(GDC-NLKC) cell at 600 °C was approximately one third of the respective value for the LNZ-(GDC-NLC) cell.

The OCVs of the cells reported here were at maximum 0.9 V at 600 °C and even lower at 550 and 500 °C. These values are lower than in e.g. Figure 20. This supports further the claim that NCAL-based current collectors used in Figure 20 are catalytically active, resulting as higher OCV than with passive Au current collectors shown in Figure 21.

Another interesting observation is that all IV-curves presented in Figure 19, Figure 20 and Figure 21 were linear. This means that the voltage loss of the cell when current was increased was caused by their ohmic resistance, resulting from the ion conduction through the cell. This further highlights the conclusion that the ohmic losses are indeed the performance-limiting factor for the SLFCs presented in this Subchapter.

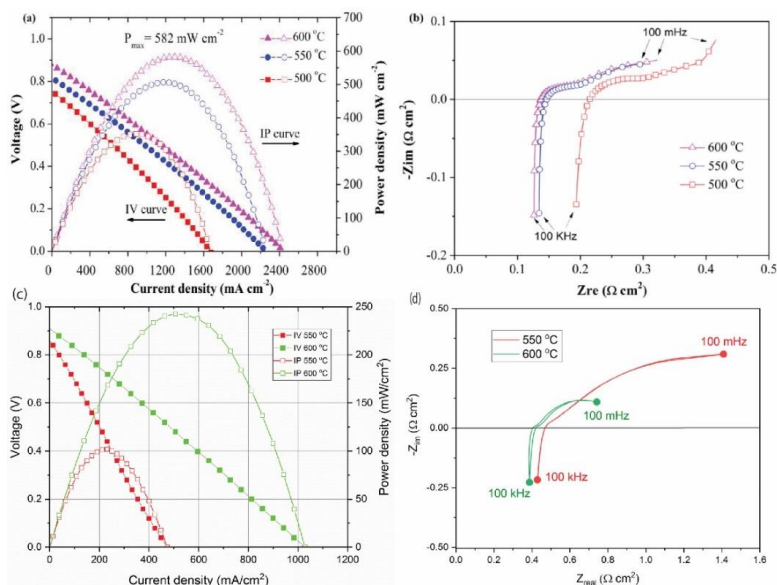


Figure 21. IV- and IP-curves of LNZ-(GDC-NLKC) (a) and LNZ-(GDC-NLC) (b) cells at different temperatures. The respective EIS-spectra (b&d). The figure is from Publication VI (preprint).

High-temperature XRD (HT-XRD) analysis of the LNZ-SDC and the LNZ-SDC-NLC nanopowders is shown in Figure 22. Both samples were characterized with the following thermal cycle: room temperature (RT) \rightarrow 450 °C (below the melting point of NLC) \rightarrow 550 °C (above the melting point of NLC) \rightarrow 450 °C \rightarrow RT. At RT a large number of peaks resulting from SDC, LiNiO and LiZnO can be observed. No additional peaks are seen with the LNZ-SDC-NLC powder, indicating that the carbonates are in amorphous state and thus invisible in XRD-spectrum. When temperature is increased, a clear peak shift towards lower angles is seen, as demonstrated in Figure 22b. This results from lattice expansion of the crystal structures. The shift is smaller for the LiZnO peaks than for LiNiO and SDC peaks.

A detailed analysis of the XRD-data shown in Figure 22 shows that the average particle sizes of different materials have significant differences: SDC (36 nm diameter) and LiNiO (45 nm) particles are much smaller than LiZnO (70 nm) particles. The lattice expansion coefficients calculated from the data were 1.0044, 1.0056 and 1.0027 for SDC, LiNiO and LiZnO respectively. This is consistent with the observed peak shifts: due to smaller lattice expansion also the peak position change observed in Figure 22b was smaller for LiZnO.

Peak splitting, indicating a phase change [81], is not observed, showing the thermal stability for LiNiO, LiZnO and SDC. Since the XRD-signal from the NLC was too weak to be detected, the melting of the NLC can not be observed via XRD. The room temperature measurements done before and after HT-XRD are similar, indicating that no permanent crystalline changes happened during the thermal cycling. However, it should be noted that a high temperature calcining was included to the preparation procedure of the powders and it may have resulted as a crystalline change.

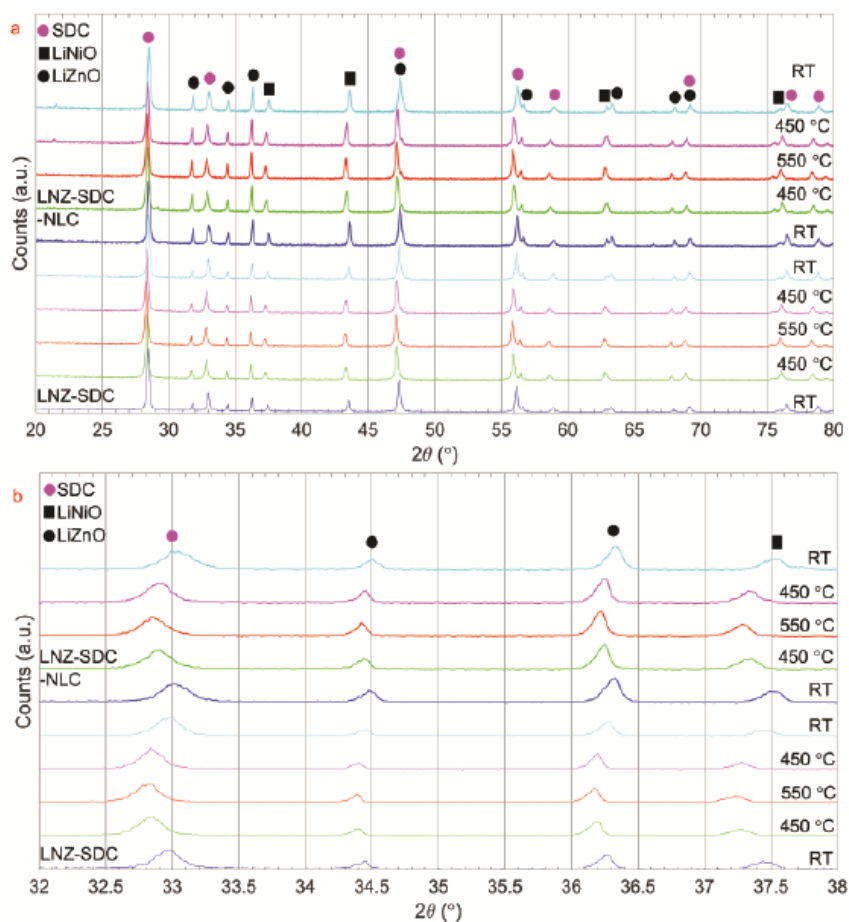


Figure 22. HT-XRD spectra of LNZ-SDC and LNZ-(SDC-NLC) nanopowders from 20° to 80° measured with the following thermal cycle: room temperature (RT, blue) → 450 °C (green) → 550 °C (red) → 450 °C (purple) → RT (cyan) (a). Zoom-in of Figure 2a in range 32°–38° (b). Reproduced from Publication VII by using author rights, © Elsevier.

Figure 23 shows cross-sectional and surface images of a LNZ-GDC-NLKC single-layer fuel cell pellet. The dual-phase structure of crystalline nanoparticles and amorphous carbonates discussed above can be seen from Figure 23 as well. A significant difference in the porosity of the surfaces can be observed when comparing the SLFC pellet surface (Figure 23b) to the three-layer fuel cell pellet surface (Figure 13a). In three-layer fuel cells the electrodes are porous to allow maximum amount of reaction sites (Subchapter 5.1, Figure 13a), but in the single-layer structure the layer has to be dense to prevent direct mixing of fuel and oxidant through the cell. This limits the amount of reaction sites at the edges of the cell, possibly limiting the cell performance.

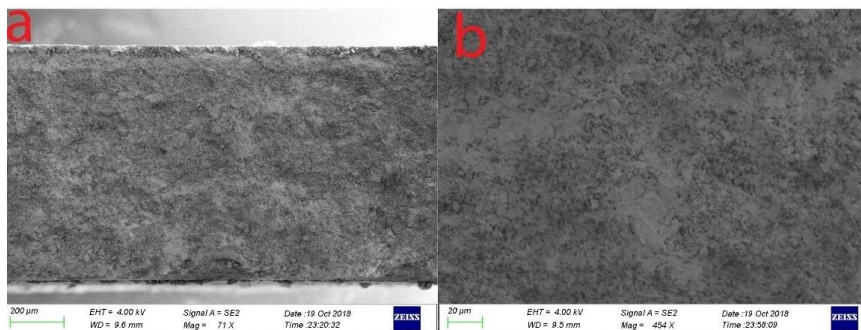


Figure 23. Cross-sectional (a) and surface (b) image of a LNZ-GDC-NLKC pellet. Dense structure with LNZ and GDC crystalline nanoparticles and amorphous NLKC is clearly visible. The figure is from Publication VI (preprint).

Figure 24 presents SEM surface images of two LNZ-SDC (a&b) and two LNZ-(SDC-NLC) (c&d) fuel cells after electrochemical measurements. All cells show a dense surface structure. For carbonate-containing cells, the two-phase structure with crystalline doped ceria and amorphous carbonate phases can be observed. The cells prepared with EC as external pore former (b&d) showed some small holes in the surface. Based on these images, the surface porosity is very low, especially with LNZ-SDC cells, even when EC is applied. This may well be one of the major performance-limiting factors for these cells.

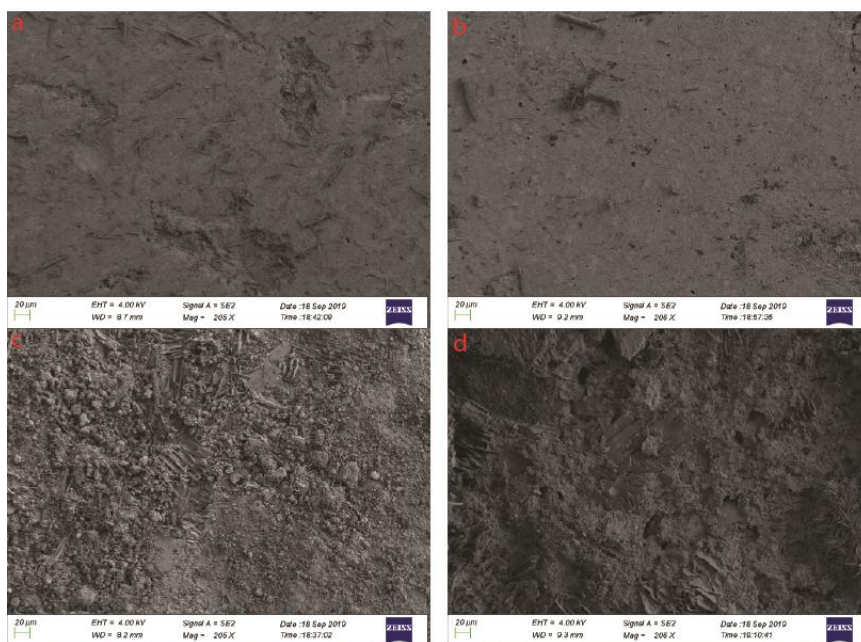


Figure 24. Surface images of LNZ-SDC fuel cells prepared without (a) and with (b) external pore former (EC). Respective images of LNZ-(SDC-NLC) fuel cells without (c) and with (d) EC. The cells were imaged after electrochemical measurements from the side that was exposed to H₂. Scale bar length is 20 µm. Reproduced from Supplementary information of Publication VII by using author rights, © Elsevier.

Figure 25 presents a comprehensive TEM analysis of LNZ-SDC and LNZ-SDC-NLC nanopowders, originally presented in Publication VII. Figure 25a-b show particle clusters consisting of nanoparticles of various sizes, whereas Figure 25c shows a high-resolution image of few individual particles and their crystalline structure. Based on the XRD-analysis of the particular powders, the smallest particles are likely to be SDC, medium-sized LiNiO and the largest ones LiZnO. However, since the particle sizes revealed by XRD are only averages, exact identification of an individual particle based on only its size is not possible.

Using elemental analysis techniques allows to study the distribution of different particles based on their composition. Here energy-dispersive X-ray spectroscopy (EDX) is used to study the particle cluster shown as a bright field image in Figure 25d. Elemental maps (Figure 25e-j) show that the clustered particles can be indeed identified as SDC and LNZ (further divided into LiNiO and LiZnO) based on the respective elemental maps. The elemental map for Na (Figure 25i) show that NLC is spread all over the cluster and appear both with SDC and LNZ. The fact that LNZ and SDC appear as separate particles that are clustered together in the nanopowder indicates that the pellets made from these powders contain both phase boundaries and continuous phases through the cell. Especially the junctions, both p-n junctions between NiO and ZnO and bulk heterojunctions between semiconductor and doped ceria, are playing a key role in charge separation and preventing the short-circuiting through the single layer.

Single-layer fuel cells made by mixing the LNZ semiconductor and doped ceria – alkali carbonate based ionic conductors with varying compositions were successfully fabricated and characterized. The role of the carbonates (NLC and NLKC) in improving the ionic conductivity of the cell was identified as the most important performance-increasing factor. Catalytically active NCAL used as a current collector improved the performance even further for NLC-containing cells. Optimizing the mass ratio of semiconductor and ionic conductor was shown to have a minor contribution to the cell performance as well. Increasing the porosity by using a small amount of EC in the fuel cell powder was observed to decrease the performance due to increased ohmic resistance. No significant difference was found between Gd (10 mol-%) and Sm (15 mol-%) dopants for the ceria.

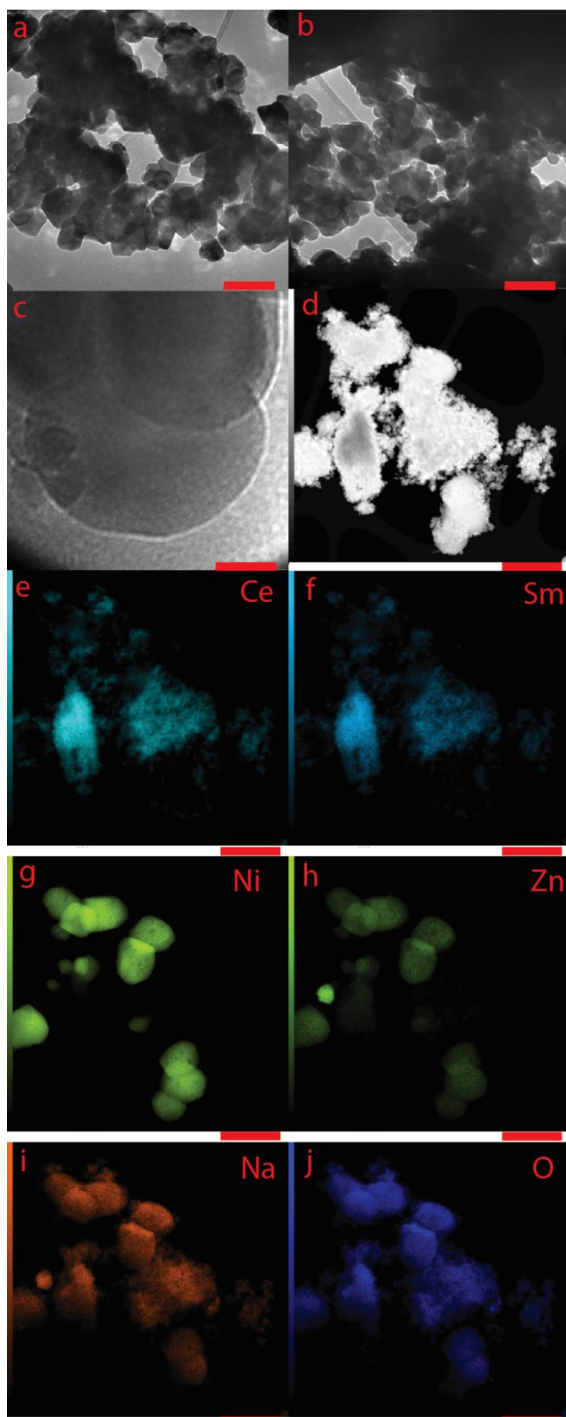


Figure 25. LNZ-SDC (a) and LNZ-(SDC-NLC) (b) nanopowders in TEM images. A high-resolution TEM image of (likely) SDC particle (c). A bright field TEM image of LNZ-(SDC-NLC) nanoparticle cluster (d) and corresponding elemental maps for Ce, Sm, Ni, Zn, Na and O (e-j). Scale bar lengths: 100 nm for (a-b), 10 nm for (c) and 200 nm for (d-j). Reproduced from Publication VII by using author rights, © Elsevier.

6. Discussion

The previous Chapters have presented the state-of-the-art results from the existing literature and from the studies included in this Thesis in the ceramic nanocomposite fuel cell (CNFC) and single-layer fuel cell (SLFC) fields. In this Chapter, the aim is to wrap up the meaning and impact of the results presented in this Thesis. Moreover, the Chapter discusses about the gaps existing in the literature (including the impact of this Thesis) and the future of the fuel cell research overall.

6.1 Ceramic nanocomposite fuel cell

CNFCs with two different material configurations, NiO-(GDC-NLC) anode – (GDC-NLC) electrolyte – LSCF-(GDC-NLC) cathode and LNCZ-(CSDC-NLKC) anode – (CSDC-NLKC) electrolyte – LSCF-(CSDC-NLKC) cathode, were fabricated and characterized in Publications II&III respectively. The key electrochemical and microstructural results are presented in Subchapter 5.1.

Although the cell compositions had significant differences, both achieved almost identical power densities, slightly above 1 W/cm² at 550 °C. The key to the high electrochemical performance was the behaviour of the electrolyte's ionic conductivity as a function of temperature: both electrolytes showed a major improvement in the conductivity near the melting point of the carbonate mixture, around 500 °C for NLC and around 400 °C for NLKC. This effect was shown in Arrhenius plots of the respective electrolyte pellets, shown in Figure 10 for GDC-NLC and in Publication III for CSDC-NLKC. This effect can be explained by opening of new ion conduction channels. Below the melting point of the carbonate mixture, the conduction is done through the solid phase. Above the melting point, besides the solid phase, the conduction can be done through the molten phase, the interfaces between the solid and molten phases and combinations of the mechanisms described above.

Due to this multi-channel conduction, the ohmic area-specific resistances of the both CNFCs reported in Subchapter 5.1 at 550 °C, above the melting point of both carbonate mixtures, were low: 0.23 Ω·cm² and 0.24 Ω·cm² for NiO-(GDC-NLC)-LSFC and LNCZ-(CSDC-NLKC)-LSCF cells respectively. The total polarization resistance calculated from the EIS data showed interestingly a significant difference: 0.63 Ω·cm² and 0.12 Ω·cm² for NiO-(GDC-NLC)-LSFC and LNCZ-(CSDC-NLKC)-LSCF respectively. This was unexpected, since the total cell resistances based on IV-curves (Figure 11) are rather similar. As discussed in Subchapter 5.1, the total resistance of a cell calculated from EIS data at V_{oc} is

corresponding to the slope of the IV-curve at V_{OC} . If there exists activation losses that are significant very close to V_{OC} , this slope may differ significantly from the slope averaged over a larger range of voltages, providing a possible explanation for these observations. This highlights the need of different characterization techniques and their comparison with each other to obtain trustworthy data from CNFCs.

XRD results showed that the GDC-NLC nanocomposite electrolyte (Publication II, Figure 12) consisted of crystalline GDC that was observed clearly with XRD and mostly amorphous NLC with a very weak XRD signal. This was expected, since the carbonate mixture was assumed to be in amorphous state. In Publication III, the successful synthesis of CSDC and LNCZ were confirmed with XRD analysis.

The structures of both anode and electrolyte materials used in Publication III were studied further with SEM (Figure 13). A dual-phase structure with the crystalline doped ceria and amorphous carbonate phases was clearly observed in SEM images, being consistent with the XRD-data from Publication II. For the anode, a suitable porosity to support hydrogen oxidation reaction was observed.

Although CNFCs reported in Publications II&III showed promising power densities, their stability is a matter of concern. As discussed in Subsection 3.1.1, the stability issues of CNFCs have been researched only little compared to e.g. improving the power density. Especially stability studies aiming to determine the potential degradation during a lifetime of a commercial device, i.e. tens of thousands of hours of operation with some maintenance breaks in between, are lacking. However, executing such studies is challenging due to extremely long measurement times, so some reliable method to accelerate the cell degradation and scale the results to actual operational conditions is necessary to complete such tests.

6.2 Single-layer fuel cell

Four different studies on the SLFC field were included in this Thesis. In all studies, the SLFC material was created by mixing a semiconductor, lithium nickel zinc oxide (LNZ) or copper iron oxide (CFO), and an ionic conductor (doped ceria or a mixture of doped ceria and alkali carbonates). These material compositions provided working SLFCs with power outputs varying from a few dozen to a several hundred mW/cm².

The working mechanisms of SLFCs have been under debate in the literature. Especially the mechanisms that prevent short-circuiting and direct gas mixing through the cell have raised discussion. For the former, especially depletion zones created by different junctions have been proposed to allow efficient charge separation. Electron blocking by the heterojunctions between different band-gap materials and the catalytic activity of the wide band-gap oxides was suggested as the working principle of LNZ-GDC SLFC in Publication IV. For the latter, sufficient density of the single layer can naturally prevent the gas crossover. Also, it is suggested that even in a porous SLFC the reaction depths for hydrogen oxidation reaction (HOR) and oxygen reduction reaction (ORR) are

much lower than a typical SLFC thickness and thus the gases are consumed before they can mix.

The existence of the p-n junctions was observed experimentally in Publication VII by microscopic analysis shown in Figure 25. Both LNZ-SDC and LNZ-(SDC-NLC) nanopowders were observed to consist of nanoparticles and particle clusters of various sizes. An elemental analysis completed to an area with several clusters of LNZ-(SDC-NLC) (total diameter around 1 μm) showed that the crystalline structures are divided into LiNiO, LiZnO and SDC, that was consistent with the XRD-data of the respective powders (Figure 22). Carbonates were distributed rather evenly all over the clusters. This phase distribution allows contacts between n-type LiNiO and p-type LiZnO, i.e. p-n junctions. Moreover, both of these semiconductors can form junctions with the ionic conductors (SDC and NLC). In actual FC operational conditions both LiNiO and LiZnO are reduced to metals on the side, where H_2 is supplied. This leads to the formation of Schottky junctions between the metals and the semiconductors. Another factor leading to formation of the Schottky junctions is the metallic nature of the current collectors: if e.g. NCAL is reduced to metals on the H_2 side and it can form a contact with non-reduced LNZ, a Schottky junction is formed. These junctions can generate depletion zones that block the electron movement through the cell and thus explain why electronic short-circuit is prevented in LNZ-based cells.

Measuring the IV-curves of LNZ-GDC cell in long range (from 4 to -4 V) under different atmospheres provided an intriguing insight on how the charge transfer is distributed between different ions. Although GDC is a typical SOFC electrolyte material supporting O^{2-} ion conduction, the experimental results presented in Subchapter 5.2 showed that the H^+ ion conduction is the dominating charge transfer process. Similar conclusions have been made also in the literature for a SDC-NC electrolyte used in a CNFC [22].

To improve the performance of LNZ-based SLFCs, adding alkali carbonates to the doped ceria was observed to be a key factor to improve the ionic conductivity through the cell. Also, using catalytically active NCAL current collector was observed to vastly improve the performance. However, since the NCAL-coated Ni-foams are likely to act, at least to some extent, as electrodes, it is questionable are the SLFCs based on a single layer sandwiched between Ni-NCAL current collectors truly single-layer devices or are they traditional three-layer devices with removable electrodes.

With CFO-GSDC cells, the sintering temperature had a significant effect to the cell performance. Especially the lowest studied sintering temperature, 600 $^{\circ}\text{C}$, resulted as a low OCV and overall performance. One likely explanation for this is that the sintering temperature was too low to achieve a suitable densification and there might have been a minor amount of gas crossover through the cell. This would explain the low OCV, and also the direct combustion reaction may have damaged the cell, explaining the high ohmic resistance. For the CFO-GSDC cells sintered at higher temperatures (800 – 1000 $^{\circ}\text{C}$), the densification was too high, limiting the amount of reaction sites at the edges of the pellets. 700 $^{\circ}\text{C}$ was observed to be an optimal sintering temperature, providing a densification that

is high enough to provide good OCV but not too high to limit the electrode reactions unnecessarily.

Since the amount of scientific publications in the SLFC field is relatively low and many publications report data from only one single cell, repeatability of the results is a key question. This is further highlighted with the work reported in this Thesis. In Subchapter 5.3, it was observed that even similar cells provided different power outputs. Dramatic difference is observed between LNZ-GDC cells reported in Publication IV (Subchapter 5.2) and Publication VII (Subchapter 5.3). The cells from Publication VII had power densities around 40 – 50 mW/cm² with Ni and NCAL-Ni current collectors, whereas in Publication IV the cell with NCAL current collector produced 800 mW/cm². This difference is way too large to be explained by random variation, especially taking into account that in Publication VII several cells with LNZ - (SDC or GDC) material combinations produced results that were relatively close to each other.

When comparing catalytically passive (Au, Publication VI) and active (Ni, NCAL-Ni, Publication VII), there is a significant difference in V_{OC} in favour of the active current collectors, as expected. However, in Publication IV, both Au and Ni-NCAL reach rather similar V_{OC} . This highlights the variation between different cells even though the manufacturing procedures are similar.

Besides repeatability, another major issue in the SLFC field needing urgent attention is the long-term stability. Hu et al. performed a 15-day stability study to a large-area LMZ-SDC cell at 600 °C with a daily 8 h operation time and observed that after a small initial performance drop the cell remained stable [77]. However, since the total operational time was only 120 h, the stability over a reasonable device lifetime cannot be claimed. Elsewhere in the literature, the stability is not studied at all in most of the SLFC articles and when it is, the degradation or stability is only reported for a short time, typically in range of hours or days [40,68,71].

This highlights the urgent need to perform more degradation studies for typical SLFC compositions with longer measurement times, possibly with accelerated aging conditions. To perform such experiment safely, an experimental setup with high level of automatization, reliable problem detection and independent emergency shutdown properties is required, increasing the infrastructure requirements and the costs when compared to a performance measurement that can be completed during a single workday. This limits the amount of research groups that can perform such experiments safely. However, since the low amount of long-term stability tests is one of the main research gaps with both CNFCs and SLFCs, investments on this issue should be considered by the research groups working with these topics.

6.3 Future of microstructural characterization of CNFCs and SLFCs

Different microscopic and spectroscopic methods have been used widely to characterize the microstructure of fuel cells in the literature (Subchapter 3.2)

and in experimental work presented in this Thesis (Chapter 5). Since the macroscopically observed properties of CNFCs and SLFCs originate from their nanoscale microstructure, accurate microstructural characterization of both fuel cells and the nanopowders used in fuel cell fabrication is identified as a key method to understand the reasons behind the macroscopic properties. This helps to identify the key challenges of the current state-of-the-art fuel cells.

Traditional microscopic and spectroscopic techniques, such as XRD, SEM and TEM, have been widely applied in CNFCs and SLFCs studies. For 3D tomography, the situation is different. 3D tomography is a powerful tool that allows building 3D reconstructions from the sample and thus determining directly some key microstructural parameters, such as phase fractions, porosity and tortuosity. Both FIB-SEM and X-ray nanotomography technologies have been applied to make such reconstructions from SOFC components (Subchapter 3.2.3), but there is an obvious gap in scientific literature when it comes to utilizing these technologies in CNFC and SLFC studies. Filling this gap by e.g. reconstructing SLFC layer with 3D tomography can provide information needed to further study e.g. gas diffusion and electrode reaction kinetics.

Another development step in microstructural characterization is increasing amount of studies performed in-situ, i.e. in actual operational conditions. For XRD, in-situ characterization has been widely applied and some literature exist also about in-situ microscopy. However, developing more accurate in-situ measurement setups allowing multiple characterization techniques at same time would help to obtain data that allows to explain not only how but why microstructural changes are happening in an operating fuel cell.

6.4 Summary

Both CNFCs and SLFCs are electricity conversion technologies that have the potential to be an important part of the future's clean energy system. In this Thesis, an excellent ionic conductivity for CNFC electrolyte was achieved by mixing doped ceria and alkali carbonates. For SLFCs, the working principles, especially ion conduction and the effect of cell densification were studied. A systematic study was made to determine how a SLFC can be optimized, e.g. by changing the composition of the ionic conductor and using external current collector.

The key challenges that still need to be solved to allow commercialization of these devices include improving long-term stability and, especially for SLFCs, improving the consistency and repeatability of the fabrication process. Understanding the underlying nanoscale properties behind the macroscopic performance, and how they change during the cell operation, is crucial to achieve this goal. Advanced microscopic techniques and in-situ measurements can play a key role to forge a link between the microstructure and the macroscopic performance, allowing to manufacture efficient and stable fuel cells.

7. Conclusions

The aim of this Thesis was to produce scientific knowledge on the CNFC and SLFC fields and thus fill the gaps observed in the literature. Microscopic methods that have been used to characterize the microstructure of SOFCs, CNFCs and SLFCs were first reviewed and discussed. The experimental part of this Thesis can be divided into three sections: fabricating high-performance CNFCs based on doped ceria – alkali carbonate mixture electrolytes, studying the fundamental working mechanisms of SLFCs and analysing systematically the factors affecting the macroscopic SLFC performance.

Microscopy is identified as an important tool in CNFC and SLFC analysis. These devices are fabricated from nanopowders and thus understanding the nanolevel properties is necessary to explain the macroscopic behaviour. SEM and TEM are typical microscopic methods used in these fields, as well as a spectroscopic technique XRD. These methods have been successfully used to characterize the structure of both nanopowders and complete fuel cells. However, since SEM and TEM can provide only 2D projections of the actual 3D structures, their applications are strictly limited. Utilizing advanced 3D techniques to reconstruct the initial samples opens new possibilities to CNFC and SLFC characterization. Two such techniques, FIB-SEM and X-ray nanotomography, have been used to study SOFC components and are likely to be suitable for CNFC and SLFC research as well. Another way to develop the microstructural analysis is to move the focus from ex-situ towards in-situ techniques.

Two CNFCs with different anode and electrolyte materials were fabricated and characterized. Both devices achieved excellent power density, slightly exceeding 1 W/cm^2 . The key behind the high performance was the doped ceria – alkali carbonate electrolyte. Above the melting point of the carbonate mixture, the dual-phase electrolyte allowed several parallel ion conduction channels. This resulted as superior ionic conductivity and lower ohmic losses when compared to the pure solid oxide electrolyte, where the ion conduction is based on oxygen vacancies only. Although CNFCs fabricated here showed excellent performance, their long-term stability is questionable, since stability studies were not included to the experimental procedure.

The ionic conduction in a LNZ-GDC SLFC exposed to a voltage within the operational (i.e. power production) region was observed to be dominated by H^+ , whereas O^{2-} played only a minor role. When passive Au current collector was replaced by catalytically active NCAL, the power density of the cell is more than doubled. A likely explanation for this is that the NCAL that was deposited on a

porous Ni-foam actually acts as an electrode and thus improves vastly the electrode reaction kinetics compared to the cell with passive Au, where all reactions are actually happening in the single LNZ-GDC layer. For another SLFC configuration, CFO-CSDC, the sintering temperature was observed to have a huge effect to power density and OCV of the cell. The densification effect strengthens as the temperature is increased, so it is concluded that optimized cell densification is a crucial factor to optimize the SLFC performance.

A systematic study of LNZ-based SLFC revealed that adding carbonates to the ionic conductor composite and using a catalytically active NCAL current collector have a strong positive effect to the cell performance. No significant difference was observed between SDC and GDC. Also, the optimal mass ratio was observed to differ from the literature standard with the NCAL current collectors.

The work done with SLFCs revealed new information on their working mechanisms and showed their potential in electricity generation. However, the consistency of the results was questioned since SLFCs with same composition showed significant differences in performance. Moreover, neither up-scaling nor long-term stability was included to the SLFC studies.

7.1 Recommendations for future work

Fuel cells are devices designed for energy production and the motivation for scientific research of fuel cells, besides the science itself, is to create new, clean energy sources for the future's power production portfolio. Thus, in applied fuel cell research, pushing the studied technologies towards commercialization is an important goal when planning new studies.

This Thesis has focused on studying the working mechanisms and improving the power density of the CNFCs and SLFCs. Understanding the device properties and achieving a suitable power output are necessary for the commercial production. However, besides high power output, commercial fuel cells need to operate stably for tens of thousands of hours and produce a suitable output power and voltage for the particular application. This highlights the need of scientific research about up-scaling and performing accelerated aging tests for both CNFCs and SLFCs. Currently, the amount of scientific literature about these issues is low and addressing these gaps can be recommended as a research topic.

Another issue requiring more research is applying advanced microscopic methods, especially 3D tomography and in-situ microscopy, to the CNFC and SLFC fields. This is partly overlapping with the previous suggestion: advanced microscopy can be a powerful tool to get insight about the degradation mechanisms occurring in a fuel cell, thus supporting research aiming for the long-term stability. In optimal case, linking the nanolevel microstructure to the macroscopic performance allows to fabricate effective and stable CNFCs and SLFCs in the future.

References

- [1] V. Masson-Delmotte, P. Zhai, H.-O. Pörtner, D. Roberts, J. Skea, P. Shukla, A. Pirani, W. Moufouma-Okia, C. Pean, R. Pidcock, S. Connors, J. Matthews, Y. Chen, X. Zhou, M. Gomis, E. Lonnoy, T. Maycock, M. Tignor and T. Waterfield, "Summary for Policymakers," in *Global Warming of 1.5 °C: An IPCC Special Report on the impacts of global warming of 1.5°C above pre-industrial levels and related global greenhouse gas emission pathways, in the context of strengthening the global response to the threat of climate change*, 2018.
- [2] International Energy Agency, Key World Energy Statistics 2019, 2019.
- [3] R. O'Hayre, S.-W. Cha, W. Colella and F. B. Prinz, Fuel cell fundamentals, New York: John Wiley & sons, 2006.
- [4] A. Kirubakaran, S. Jain and R. Nema, "A review on fuel cell technologies and power electronic interface," *Renewable and Sustainable Energy Reviews*, vol. 13, pp. 2430-2440, 2009.
- [5] N. Mahato, A. Banerjee, A. Gupta, S. Omar and K. Balani, "Progress in material selection for solid oxide fuel cell technology: A review," *Progress in Material Science*, vol. 72, pp. 141-337, 2015.
- [6] R. M. Ormerod, "Solid oxide fuel cells," *Chemical Society Reviews*, vol. 32, pp. 17-28, 2003.
- [7] B. Zhu, "Solid oxide fuel cell (SOFC) technical challenges and solutions from nano-aspects," *International Journal of Energy Research*, vol. 33, pp. 1126-1137, 2009.
- [8] L. Fan, B. Zhu, P.-C. Su and C. He, "Nanomaterials and technologies for low temperature solid oxide fuel cells: Recent advances, challenges and opportunities," *Nano Energy*, vol. 45, pp. 148-176, 2018.
- [9] H. Yokokawa, H. Tu, B. Iwanschitz and A. Mai, "Fundamental mechanisms limiting solid oxide fuel cell durability," *Journal of Power Sources*, vol. 182, pp. 400-412, 2008.

- [10] S. Badwal, "Stability of solid oxide fuel cell components," *Solid State Ionics*, vol. 143, pp. 39-46, 2001.
- [11] B. Zhu, "Next generation fuel cell R&D," *International Journal of Energy Research*, vol. 30, pp. 895-903, 2006.
- [12] B. Zhu, "Proton and oxygen ion-mixed-conducting ceramic composites and fuel cells," *Solid State ionics*, vol. 145, pp. 371-380, 2001.
- [13] B. Zhu, "Functional ceria-salt-composite materials for advanced ITSOFC applications," *Journal of Power Sources*, vol. 114, pp. 1-9, 2003.
- [14] B. Zhu, X. Yang, J. Xu, Z. Zhu, S. Ji, M. Sun and J. Sun, "Innovative low temperature SOFCs and advanced materials," *Journal of Power Sources*, vol. 118, pp. 47-53, 2003.
- [15] J. Patakangas, Y. Ma, Y. Jing and P. D. Lund, "Review and analysis of characterization methods and ionic conductivities for low-temperature solid oxide fuel cells (LT-SOFC)," *Journal of Power Sources*, vol. 263, pp. 315-331, 2014.
- [16] B. Zhu, L. Fan and P. Lund, "Breakthrough fuel cell technology using ceria-based multi-functional nanocomposites," *Applied Energy*, vol. 106, pp. 163-175, 2013.
- [17] L. Fan, C. Wang, M. Chen and B. Zhu, "Recent development of ceria-based (nano)composite materials for low temperature ceramic fuel cells and electrolyte-free fuel cells," *Journal of Power Sources*, vol. 234, pp. 154-174, 2013.
- [18] B. Zhu, Y. Ma, X. Wang, R. Raza, H. Qin and L. Fan, "A fuel cell with a single component functioning simultaneously as the electrodes and the electrolyte," *Electrochemistry Communications*, vol. 13, pp. 225-227, 2011.
- [19] Y. Wang, K. Chen, J. Mishler, S. Cho and X. Adroher, "A review of polymer electrolyte membrane fuel cells: Technology, applications, and needs of fundamental research," *Applied Energy*, vol. 88, pp. 981-1007, 2011.
- [20] G. McLean, T. Niet, S. Prince-Richard and N. Djilali, "An assesment of alkaline fuel cell technology," *International Journal of Hydrogen Energy*, vol. 27, pp. 507-526, 2002.
- [21] E. Antolini, "The stability of molten carbonate fuel cell electrodes: A review of recent improvements," *Applied Energy*, vol. 88, pp. 4274-4293, 2011.
- [22] X. Wang, Y. Ma, S. Li, A.-H. Kashyout, B. Zhu and M. Muhammed, "Ceria-based nanocomposite with simultaneous proton and oxygen ion conductivity for

- low-temperature solid oxide fuel cells," *Journal of Power Sources*, vol. 196, pp. 2754-2758, 2011.
- [23] Y. Zhao, D.-B. Xiong, H. Qin, F. Gao, H. Inui and B. Zhu, "Nanocomposite electrode materials for low temperature solid oxide fuel cells using the ceria-carbonate composite electrolytes," *International Journal of Hydrogen Energy*, vol. 37, pp. 19351-19356, 2012.
- [24] A. Rafique, R. Raza, N. Akram, M. K. Ullah, A. Ali, M. Irshad, K. Siraj, M. A. Khan, B. Zhu and R. Dawson, "Significance enhancement in the conductivity of core shell nanocomposite electrolytes," *RSC Advances*, vol. 5, pp. 86322-86329, 2015.
- [25] M. I. Asghar, S. Lepikko, J. Patakangas, J. Halme and P. D. Lund, "Comparative analysis of ceramic-carbonate nanocomposite fuel cells using composite GDC/NLC electrolyte with different perovskite structured cathode materials," *Frontiers of Chemical Science and Engineering*, vol. 12, pp. 162-173, 2018.
- [26] J. Huang, Z. Mao, Z. Liu and C. Wang, "Development of novel low-temperature SOFCs with co-ionic conducting SDC-carbonate composite electrolytes," *Electrochemistry Communications*, vol. 9, pp. 2601-2605, 2007.
- [27] C. Xia, Y. Li, Y. Tian, Q. Liu, Z. Wang, L. Jia, Y. Zhao and Y. Li, "Intermediate temperature fuel cell with a doped ceria-carbonate composite electrolyte," *Journal of Power Sources*, vol. 195, pp. 3149-3154, 2010.
- [28] L. Fan, C. Wang and B. Zhu, "Low temperature ceramic fuel cells using all nano composite materials," *Nano energy*, vol. 1, pp. 631-639, 2012.
- [29] J. Di, M. Chen, C. Wang, J. Zheng, L. Fan and B. Zhu, "Samarium doped ceria-(Li/Na)₂CO₃ composite electrolyte and its electrochemical properties in low temperature solid oxide fuel cell," *Journal of Power Sources*, vol. 195, pp. 4695-4699, 2010.
- [30] Z. Tang, Q. Lin, B.-E. Mellander and B. Zhu, "SDC-LiNa carbonate composite and nanocomposite electrolytes," *International Journal of Hydrogen Energy*, vol. 35, pp. 2970-2975, 2010.
- [31] M. I. Asghar, M. Heikkilä and P. D. Lund, "Advanced low-temperature ceramic nanocomposite fuel cells using ultra high ionic conductivity electrolytes synthesized through freeze-dried method and solid-route," *Materials Today Energy*, vol. 5, pp. 338-346, 2017.
- [32] J. Patakangas, Y. Jing, M. I. Asghar and P. D. Lund, "Investigation of LiNiCuZn-oxide electrodes prepared by different methods: Synthesis, characterization and properties for ceramic carbonate composite fuel cells," *International Journal of Hydrogen Energy*, vol. 41, pp. 7609-7613, 2016.

- [33] M. Mogensen, N. Sammes and G. Tompsett, "Physical, chemical and electrochemical properties of pure and doped ceria," *Solid State Ionics*, vol. 129, pp. 63-94, 2000.
- [34] C. Artini, M. Pani, M. Carnasciali, M. Buscaglia, J. Plaisier and G. Costa, "Structural Features of Sm- and Gd-Doped Ceria Studied by Synchrotron X-ray Diffraction and μ -Raman Spectroscopy," *Inorganic Chemistry*, vol. 54, pp. 4126-4137, 2015.
- [35] F. Loureiro, S. Rajesh, F. Figueiredo and F. Marques, "Stability of metal oxides against Li/Na carbonates in composite electrolytes," *RSC Advances*, vol. 4, p. 59943, 2014.
- [36] A. Evans, W. Xing and T. Norby, "Electromotive Force (emf) Determination of Transport Numbers for Native and Foreign Ions in Molten Alkali Metal Carbonates," *Journal of the Electrochemical Society*, vol. 162, pp. F1135-F1143, 2015.
- [37] M. Afzal, M. Saleemi, B. Wang, C. Xia, W. Zhang, Y. He, J. Jayasuriya and B. Zhu, "Fabrication of novel electrolyte-layer free fuel cell with semi-ionic conductor ($\text{Ba}_{0.5}\text{Sr}_{0.5}\text{Co}_{0.8}\text{Fe}_{0.2}\text{O}_{3-\delta}$ - $\text{Sm}_{0.2}\text{Ce}_{0.8}\text{O}_{1.9}$) and Schottky barrier," *Journal of Power Sources*, vol. 328, pp. 136-142, 2016.
- [38] B. Zhu, P. D. Lund, R. Raza, Y. Ma, L. Fan, M. Afzal, J. Patakangas, Y. He, Y. Zhao, W. Tan, Q.-A. Huang, J. Zhang and H. Wang, "Schottky Junction Effect on High Performance Fuel Cells Based on Nanocomposite Materials," *Advanced Energy Materials*, vol. 5, p. 1401895, 2015.
- [39] H. Deng, C. Feng, W. Zhang, Y. Mi, X. Wang, W. Dong, B. Wang and B. Zhu, "The electrolyte-layer free fuel cell using a semiconductor-ionic $\text{Sr}_2\text{Fe}_{1.5}\text{Mo}_{0.5}\text{O}_{6-\delta}$ - $\text{Ce}_{0.8}\text{Sm}_{0.2}\text{O}_{2-\delta}$ composite functional membrane," *International Journal of Hydrogen Energy*, vol. 42, pp. 25001-25007, 2017.
- [40] K. Shao, F. Li, G. Zhang, Q. Zhang, K. Malituna and L. Fan, "Approaching Durable Single-Layer Fuel Cells: Promotion of Electroactivity and Charge Separation via Nanoalloy Redox Exsolution," *ACS Applied Materials & Interfaces*, vol. 11, pp. 27924-27933, 2019.
- [41] B. Zhu, H. Qin, R. Raza, Q. Liu, L. Fan, J. Patakangas and P. Lund, "A single-component fuel cell reactor," *International Journal of Hydrogen Energy*, vol. 36, pp. 8536-8541, 2011.
- [42] Q. Liu, H. Qin, R. Raza, L. Fan, Y. Li and B. Zhu, "Advanced electrolyte-free fuel cells based on functional nanocomposites of a single porous component: analysis, modeling and validation," *RSC Advances*, vol. 2, pp. 8036-8040, 2012.

- [43] B. Zhu, R. Raza, G. Abbas and M. Singh, "An Electrolyte-Free Fuel Cell Constructued from One Homogenous Layer with Mixed Conductivity," *Advanced Functional Materials*, vol. 21, pp. 2465-2469, 2011.
- [44] S. Choi, H. An, K. Yoon, B.-K. Kim, H.-W. Lee, J.-W. Son, H. Kim, D. Shin, H.-I. Ji and J.-H. Lee, "Electrochemical analysis of high-performance protonic ceramic fuel cells based on a columnar-structured thin electrolyte," *Applied Energy*, Vols. 233-234, pp. 29-36, 2019.
- [45] J. Kupecki, R. Kluczowski, D. Papurello, A. Lanzini, M. Kawalec, M. Krauz and M. Santarelli, "Characterization of a circular 80 mm anode supported solid oxide fuel cell (AS-SOFC) with anode support produced using high-pressure injection molding (HPIM)," *International Journal of Hydrogen Energy*, vol. 44, pp. 19405-19411, 2019.
- [46] Y. Zhang, X. Huang, Z. Lu, Z. Liu, X. Ge, J. Xu, X. Xin, X. Sha and W. Su, "A screen-printed $\text{Ce}_{0.8}\text{Sm}_{0.2}\text{O}_{1.9}$ film solid oxide fuel cell with a $\text{Ba}_{0.5}\text{Sr}_{0.5}\text{Co}_{0.8}\text{Fe}_{0.2}\text{O}_{3-\delta}$ cathode," *Journal of Power Sources*, vol. 160, pp. 1217-1220, 2006.
- [47] Y. Zhang, J. Liu, X. Huang, Z. Lu and W. Su, "Low temperature solid oxide fuel cell with $\text{Ba}_{0.5}\text{Sr}_{0.5}\text{Co}_{0.8}\text{Fe}_{0.2}\text{O}_3$ cathode prepared by screen printing," *Solid State Ionics*, vol. 179, pp. 250-255, 2008.
- [48] L. Zhao, X. Huang, R. Zhu, Z. Lu, W. Sun, Y. Zhang, X. Ge, Z. Liu and W. Su, "Optimization on technical parameters for fabrication of SDC film by screen-printing used as electrolyte in IT-SOFC," *Journal of Physics and Chemistry of Solids*, vol. 69, pp. 2019-2024, 2008.
- [49] J. G. Lee, J. H. Park and Y. G. Shul, "Tailoring gadolinium-doped ceria-based solid oxide fuel cells to achieve 2 Wcm^{-2} at 550°C ," *Nature Communications*, vol. 5, p. 4045, 2014.
- [50] S. Chen, D. Gu, Y. Zheng, H. Chen and L. Guo, "Enhanced performance of NiO-3YSZ planar anode-supported SOFC with an anode functional layer," *Journal of Material Science*, vol. 55, pp. 88-98, 2020.
- [51] X. Wang, Y. Ma and B. Zhu, "State of the art ceria-carbonate composites (3C) electrolyte for advanced low temperature ceramic fuel cells (LTCFCs)," *International Journal of Hydrogen Energy*, vol. 37, pp. 19417-19425, 2012.
- [52] W. Tan, L. Fan, R. Raza, M. A. Khan and B. Zhu, "Studies of modified lithiated NiO cathode for low temperature solid oxide fuel cell with ceria-carbonate composite electrolyte," *International Journal of Hydrogen Energy*, vol. 38, pp. 370-376, 2013.

- [53] S. Terada, I. Nagashima, K. Higaki and Y. Ito, "Stability of LiAlO_2 as electrolyte matrix for molten carbonate fuel cells," *Journal of Power Sources*, vol. 75, pp. 223-229, 1998.
- [54] S. Li and J. Sun, "Electrochemical performance of NANOCOFC in MCFC environments," *International Journal of Hydrogen Energy*, vol. 35, pp. 2980-2985, 2010.
- [55] M. Benamira, A. Ringuede, L. Hildebrant, C. Lagergren, R.-N. Vannier and M. Cassir, "Gadolinia-doped ceria mixed with alkali carbonates for SOFC applications: II. An electrochemical insight," *International Journal of Hydrogen Energy*, vol. 37, pp. 19371-19379, 2012.
- [56] X. Li, G. Xiao and K. Huang, "Effective Ionic Conductivity of a Novel Intermediate-Temperature Mixed Oxide-Ion and Carbonate-Ion Conductor," *Journal of the Electrochemical Society*, vol. 158, pp. B225-B232, 2011.
- [57] L. Zhang, R. Lan, C. T. Petit and S. Tao, "Durability study of an intermediate temperature fuel cell based on an oxide-carbonate composite electrolyte," *International Journal of Hydrogen Energy*, vol. 35, pp. 6934-6940, 2010.
- [58] H. He, X. Huang and L. Chen, "Sr-doped LaInO_3 and its possible application in a single layer SOFC," *Solid State Ionics*, vol. 130, pp. 183-193, 2000.
- [59] B. Zhu, R. Raza, H. Qin, Q. Liu and L. Fan, "Fuel cells based on electrolyte and non-electrolyte separators," *Energy and Environmental Science*, vol. 4, p. 2986, 2011.
- [60] B. Zhu, R. Raza, H. Qin and L. Fan, "Single-component and three-component fuel cells," *Journal of Power Sources* 196, pp. 6362-6365, 2011.
- [61] B. Zhu, P. Lund, R. Raza, J. Patakangas, Q.-A. Huang, L. Fan and M. Singh, "A new energy conversion technology based on nano-redox and nano-device progress," *Nano Energy*, vol. 2, pp. 1179-1185, 2013.
- [62] B. Zhu, L. Fan, H. Deng, Y. He, M. Afzal, W. Dong, A. Yaqub and N. Janjua, "LiNiFe-based layered structure oxide and composite for advanced single layer fuel cells," *Journal of Power Sources*, vol. 316, pp. 37-43, 2016.
- [63] H. Hu, Q. Lin, Z. Zhu, X. Liu, M. Afzal, Y. He and B. Zhu, "Effects of composition on the electrochemical property and cell performance of single layer fuel cell," *Journal of Power Sources*, vol. 275, pp. 476-482, 2015.
- [64] H. Hu, Q. Lin, A. Muhammad and B. Zhu, "Electrochemical study of lithiated transition metal oxide composite for single layer fuel cell," *Journal of Power Sources*, vol. 286, pp. 388-393, 2015.

- [65] L. Fan, C. Wang, O. Osamudiamen, R. Raza, M. Singh and B. Zhu, "Mixed ion and electron conductive composites for single component fuel cells: I. Effects of composition and pellet thickness," *Journal of Power Sources*, vol. 217, pp. 164-169, 2012.
- [66] H. Deng, W. Zhang, X. Wang, Y. Mi, W. Dong, W. Tan and B. Zhu, "An ionic conductor $\text{Ce}_{0.8}\text{Sm}_{0.2}\text{O}_{2-6}$ (SDC) and semiconductor $\text{Sm}_{0.5}\text{Sr}_{0.5}\text{CoO}_3$ (SSC) composite for high performance electrolyte-free fuel cell," *International Journal of Hydrogen Energy*, vol. 42, pp. 22228-22234, 2017.
- [67] Y. Liu, Y. Meng, W. Zhang, B. Wang, M. Afzal, C. Xia and B. Zhu, "Industrial grade rare-earth triple-doped ceria applied for advanced low-temperature electrolyte layer-free fuel cells," *International Journal of Hydrogen Energy*, vol. 42, pp. 22273-22279, 2017.
- [68] W. Zhang, Y. Cai, B. Wang, C. Xia, W. Dong, J. Li and B. Zhu, "Mixed ionic-electronic conductor membrane based fuel cells by incorporating semiconductor $\text{Ni}_{0.8}\text{Co}_{0.15}\text{Al}_{0.05}\text{LiO}_{2-6}$ into the $\text{Ce}_{0.8}\text{Sm}_{0.2}\text{O}_{2-6}$ - Na_2CO_3 electrolyte," *International Journal of Hydrogen Energy*, vol. 41, pp. 15346-15353, 2016.
- [69] W. Zhang, Y. Cai, B. Wang, H. Deng, C. Feng, W. Dong, J. Li and B. Zhu, "The fuel cells studies from ionic electrolyte $\text{Ce}_{0.8}\text{Sm}_{0.05}\text{Ca}_{0.15}\text{O}_{2-6}$ to the mixture layers with semiconductor $\text{Ni}_{0.8}\text{Co}_{0.15}\text{Al}_{0.05}\text{LiO}_{2-6}$," *International Journal of Hydrogen Energy*, vol. 41, pp. 18761-18768, 2016.
- [70] B. Zhu, B. Wang, Y. Wang, R. Raza, W. Tan, J.-S. Kim, P. van Aken and P. D. Lund, "Charge separation and transport in $\text{La}_{0.6}\text{Sr}_{0.4}\text{Co}_{0.2}\text{Fe}_{0.8}\text{O}_{3-6}$ and ion-doping ceria heterostructure material for new generation fuel cell," *Nano Energy*, vol. 37, pp. 195-202, 2017.
- [71] C. Xia, B. Wang, Y. Ma, Y. Cai, M. Afzal, Y. Liu, Y. He, W. Zhang, W. Dong, J. Li and B. Zhu, "Industrial-grade rare-earth and perovskite oxide for high-performance electrolyte layer-free fuel cell," *Journal of Power Sources*, vol. 307, pp. 270-279, 2016.
- [72] B. Zhu, Y. Huang, L. Fan, Y. Ma, B. Wang, C. Xia, M. Afzal, B. Zhang, W. Dong, H. Wang and P. D. Lund, "Novel fuel cell with nanocomposite functional layer designed by perovskite solar cell principle," *Nano Energy* 19, pp. 156-164, 2016.
- [73] B. Wang, Y. Wang, L. Fan, Y. Cai, C. Xia, Y. Liu, R. Raza, P. van Aken, H. Wang and B. Zhu, "Preparation and characterization of Sm and Ca co-doped ceria- $\text{La}_{0.6}\text{Sr}_{0.4}\text{Co}_{0.2}\text{Fe}_{0.8}\text{O}_{3-6}$ semiconductor-ionic composites for electrolyte-layer-free fuel cells," *Journal of Materials Chemistry A*, vol. 4, pp. 15426-15436, 2016.

- [74] X. Dong, L. Tian, J. Li, Y. Zhao, Y. Tian and Y. Li, "Single layer fuel cell based on a composite of $\text{Ce}_{0.8}\text{Sm}_{0.2}\text{O}_{2-6}-\text{Na}_2\text{CO}_3$ and a mixed ionic and electronic conductor $\text{Sr}_2\text{Fe}_{1.5}\text{Mo}_{0.5}\text{O}_{6-6}$," *Journal of Power Sources*, vol. 249, pp. 270-276, 2014.
- [75] B. Zhu, L. Fan, Y. Zhao, W. Tan, D. Xiong and H. Wang, "Functional semiconductor-ionic composite GDC-KZnAl/LiNiCuZnO_x for single-component fuel cell," *RSC Advances*, vol. 4, pp. 9920-9925, 2014.
- [76] H. Hu, Q. Lin, Z. Zhu, B. Zhu and X. Liu, "Fabrication of electrolyte-free fuel cell with $\text{Mg}_{0.4}\text{Zn}_{0.6}\text{O}/\text{Ce}_{0.8}\text{Sm}_{0.2}\text{O}_{2-6}-\text{Li}_{0.3}\text{Ni}_{0.6}\text{Cu}_{0.07}\text{Sr}_{0.03}\text{O}_{2-6}$ layer," *Journal of Power Sources*, vol. 248, pp. 577-581, 2014.
- [77] H. Hu, Q. Lin, Z. Zhu, X. Liu and B. Zhu, "Time-dependent performance change of single layer fuel cell with $\text{Li}_{0.4}\text{Mg}_{0.3}\text{Zn}_{0.3}\text{O}/\text{Ce}_{0.8}\text{Sm}_{0.2}\text{O}_{2-6}$ composite," *International Journal of Hydrogen Energy*, vol. 39, pp. 10718-10723, 2014.
- [78] Y. Lu, B. Zhu, Y. Cai, J.-S. Kim, B. Wang, J. Wang, Y. Zhang and J. Li, "Progress in Electrolyte-Free Fuel Cells," *Frontiers in Energy Research*, vol. 4, 2016.
- [79] J. S. J. Hargreaves, "Some considerations related to the use of the Scherrer equation in powder X-ray diffraction as applied to heterogenous catalysts," *Catalysis, Structure & Reactivity*, vol. 2, pp. 33-37, 2016.
- [80] U. Holzwarth and N. Gibson, "The Scherrer equation versus the 'Debye-Scherrer equation'," *Nature Nanotechnology*, vol. 6, 2011.
- [81] F. Dong, M. Ni, W. He, Y. Chen, G. Yang, D. Chen and Z. Shao, "An efficient electrocatalyst as cathode material for solid oxide fuel cells: $\text{BaFe}_{0.95}\text{Sn}_{0.05}\text{O}_{3-6}$," *Journal of Power Sources*, vol. 326, pp. 459-465, 2016.
- [82] B. Qian, Y. Chen, M. Tade and Z. Shao, " $\text{BaCo}_{0.6}\text{Fe}_{0.3}\text{Sn}_{0.1}\text{O}_{3-6}$ perovskite as a new superior oxygen reduction electrode for intermediate-to-low temperature solid oxide fuel cells," *Journal of Materials Chemistry A*, vol. 2, p. 15078, 2014.
- [83] B. Molero-Sanchez, J. Prado-Gonjal, D. Avila-Brandé, M. Chen, E. Moran and V. Birss, "High performance $\text{La}_{0.3}\text{Ca}_{0.7}\text{Cr}_{0.3}\text{Fe}_{0.7}\text{O}_{3-6}$ air electrode for reversible solid oxide fuel cell applications," *International Journal of Hydrogen Energy*, vol. 40, pp. 1902-1910, 2015.
- [84] F. Dong, D. Chen, Y. Chen, Q. Zhao and Z. Shao, "La-doped BaFeO_{3-6} perovskite as a cobalt-free oxygen reduction electrode for solid oxide fuel cells with oxygen-ion conducting electrolyte," *Journal of Materials Chemistry*, vol. 22, p. 15071, 2012.

- [85] J. Cazaux, "From the physics of secondary electron emission to image contrasts in scanning electron microscopy," *Journal of Electron Microscopy*, vol. 61, pp. 261-284, 2012.
- [86] K. Vernon-Parry, "Scanning Electron Microscopy: an Introduction," *III-Vs Review*, vol. 13, pp. 40-44, 2000.
- [87] J. Österreicher, F. Grabner, A. Schiffl, S. Schwarz and G. Bourret, "Information depth in backscattered electron microscopy of nanoparticles within a solid matrix," *Materials Characterization*, vol. 138, pp. 145-153, 2018.
- [88] N. Jordan, W. Assenmacher, S. Uhlenbruk, V. Haanappel, H. Buchkremer, D. Stöver and W. Mader, " $\text{Ce}_{0.8}\text{Gd}_{0.2}\text{O}_{2-6}$ protecting layers manufactured by physical vapor deposition for IT-SOFC," *Solid State Ionics*, vol. 179, pp. 919-923, 2008.
- [89] D. Waldbillig, A. Wood and D. Ivey, "Electrochemical and microstructural characterization of the redox tolerance of solid oxide fuel cell anodes," *Journal of Power Sources*, vol. 145, pp. 206-215, 2005.
- [90] J. Yan, H. Matsumoto, M. Enoki and T. Ishihara, "High-Power SOFC Using $\text{La}_{0.9}\text{Sr}_{0.1}\text{Ga}_{0.8}\text{Mg}_{0.2}\text{O}_{3-6}/\text{Ce}_{0.8}\text{Sm}_{0.2}\text{O}_{2-6}$ Composite Film," *Electrochemical and Solid-State Letters*, vol. 8, pp. A389-A391, 2005.
- [91] H. Abe, K. Murata, T. Fukui, W.-J. Moon, K. Kaneko and M. Naito, "Microstructural control of Ni-YSZ cermet anode for planer thin-film solid oxide fuel cells," *Thin Solid Films*, vol. 496, pp. 49-52, 2006.
- [92] A. Mai, M. Becker, W. Assenmacher, F. Tietz, D. Hathiramani, E. Ivers-Tiffée, D. Stöver and W. Mader, "Time-dependent performance of mixed-conducting SOFC cathodes," *Solid State Ionics*, vol. 177, pp. 1965-1968, 2006.
- [93] J. Pusz, A. Smirnova, A. Mohammadi and N. Sammes, "Fracture strength of micro-tubular solid oxide fuel cell anode in redox cycling experiments," *Journal of Power Sources*, vol. 163, pp. 900-906, 2007.
- [94] E. Nikolla, J. Schwank and S. Linic, "Hydrocarbon steam reforming on Ni alloys at solid oxide fuel cell operating conditions," *Catalysis Today*, vol. 136, pp. 243-248, 2008.
- [95] K. Thyden, Y. Liu and J. Bilde-Sørensen, "Microstructural characterization of SOFC Ni-YSZ anode composites by low-voltage scanning electron microscopy," *Solid State Ionics*, vol. 178, pp. 1984-1989, 2008.
- [96] M. Han, X. Tang, H. Yin and S. Peng, "Fabrication, microstructure and properties of a YSZ electrolyte for SOFCs," *Journal of Power Sources*, vol. 165, pp. 757-763, 2007.

- [97] C. Xia and M. Liu, "Microstructures, conductivities, and electrochemical properties of $\text{Ce}_{0.9}\text{Gd}_{0.1}\text{O}_2$ and GDC–Ni anodes for low-temperature SOFCs," *Solid State Ionics*, Vols. 152-153, pp. 423-430, 2002.
- [98] L. Nie, M. Liu, Y. Zhang and M. Liu, " $\text{La}_{0.6}\text{Sr}_{0.4}\text{Co}_{0.2}\text{Fe}_{0.8}\text{O}_{3-\delta}$ cathodes infiltrated with samarium-doped cerium oxide for solid oxide fuel cells," *Journal of Power Sources*, vol. 195, pp. 4704-4708, 2010.
- [99] A. Soldati, L. Baque, H. Troiani, C. Cotaro, A. Schreiber, A. Caneiro and A. Serquis, "High resolution FIB-TEM and FIB-SEM characterization of electrode/electrolyte interfaces in solid oxide fuel cells materials," *International Journal of Hydrogen Energy*, vol. 36, pp. 9180-9188, 2011.
- [100] M. Shah, P. Voorhees and S. Barnett, "Time-dependent performance changes in LSCF-infiltrated SOFC cathodes: The role of nano-particle coarsening," *Solid State Ionics*, vol. 187, pp. 64-67, 2011.
- [101] H.-S. Noh, J.-S. Park, H. Lee, H.-W. Lee, J.-H. Lee and J.-W. Son, "Transmission Electron Microscopy Study on Microstructure and Interfacial Property of Thin Film Electrolyte SOFC," *Electrochemical and Solid-State Letters*, vol. 14, pp. B26-B29, 2011.
- [102] E. Bucher, C. Gspan, F. Hofer and W. Sitte, "Post-test analysis of silicon poisoning and phase decomposition in the SOFC cathode material $\text{La}_{0.58}\text{Sr}_{0.4}\text{Co}_{0.2}\text{Fe}_{0.8}\text{O}_{3-\delta}$ by transmission electron microscopy," *Solid State Ionics*, vol. 230, pp. 7-11, 2013.
- [103] M. Benamira, A. Ringuede, V. Albin, R.-N. Vannier, L. Hildebrandt, C. Lagergren and M. Cassir, "Gadolinia-doped ceria mixed with alkali carbonates for solid oxide fuel cell applications: I. A thermal, structural and morphological insight," *Journal of Power Sources*, vol. 196, pp. 5546-5554, 2011.
- [104] G. Nelson, W. Harris, J. Lombardo, J. Izzo, W. Chiu, P. Tanasini, M. Cantoni, J. Van herle, C. Comninellis, J. Andrews, Y. Liu, P. Pianetta and Y. Chu, "Comparison of SOFC cathode microstructure quantified using X-ray nanotomography and focused ion beam–scanning electron microscopy," *Electrochemistry Communications*, vol. 13, pp. 586-589, 2011.
- [105] N. Vivet, S. Cupin, E. Estrade, A. Richard, S. Bonnamy, D. Rochais and E. Bruneton, "Effect of Ni content in SOFC Ni-YSZ cermets: A three dimensional study by FIB-SEM tomography," *Journal of Power Sources*, vol. 196, pp. 9989-9997, 2011.
- [106] J. Wilson, W. Kobsiriphat, R. Mendoza, H.-Y. Chen, J. Hiller, D. Miller, K. Thornton, P. Voorhees, S. Adler and S. Barnett, "Three-dimensional reconstruction of a solid-oxide fuel-cell anode," *Nature Materials*, vol. 5, pp. 541-544, 2006.

- [107] H. Iwai, N. Shikazono, T. Matsui, H. Teshima, M. Kishimoto, R. Kishida, D. Hayashi, K. Matsuzaki, D. Kanno, M. Saito, H. Muroyama, K. Eguchi, N. Kasagi and H. Yoshida, "Quantification of SOFC anode microstructure based on dual beam FIB-SEM technique," *Journal of Power Sources*, vol. 195, pp. 955-961, 2010.
- [108] J. Wilson, J. Cronin and S. Barnett, "Linking the microstructure, performance and durability of Ni-yttria-stabilized zirconia solid oxide fuel cell anodes using three-dimensional focused ion beam scanning electron microscopy imaging," *Scripta Materialia*, vol. 65, pp. 67-72, 2011.
- [109] K. Yakal-Kremiski, J. Cronin, Y. Chen-Wiegart, J. Wang and S. Barnett, "Studies of Solid Oxide Fuel Cell Electrode Evolution Using 3D Tomography," *Fuel Cells*, vol. 13, pp. 449-454, 2013.
- [110] M. Kishimoto, M. Lomberg, E. Ruiz-Trejo and N. Brandon, "Enhanced triple-phase boundary density in infiltrated electrodes for solid oxide fuel cells demonstrated by high-resolution tomography," *Journal of Power Sources*, vol. 266, pp. 291-295, 2014.
- [111] J. Wilson, A. Duong, M. Gameiro, H.-Y. Chen, K. Thornton, D. Mumm and S. Barnett, "Quantitative three-dimensional microstructure of a solid oxide fuel cell cathode," *Electrochemistry Communications*, vol. 11, pp. 1052-1056, 2009.
- [112] J. Smith, A. Chen, D. Gostovic, D. Hickey, D. Kundinger, K. Duncan, R. DeHoff, K. Jones and E. Wachsman, "Evaluation of the relationship between cathode microstructure and electrochemical behavior for SOFCs," *Solid State Ionics*, vol. 180, pp. 90-98, 2009.
- [113] J. Villanova, J. Laurencin, P. Cloetens, P. Bleuet, G. Delette, H. Suhonen and F. Usseglio-Viretta, "3D phase mapping of solid oxide fuel cell YSZ/Ni cermet at the nanoscale by holographic X-ray nanotomography," *Journal of Power Sources*, vol. 243, pp. 841-849, 2013.
- [114] P. Shearing, J. Gelb, J. Yi, W.-K. Lee, M. Drakopoulos and N. Brandon, "Analysis of triple phase contact in Ni-YSZ microstructures using non-destructive X-ray nanotomography with synchrotron radiation," *Electrochemistry Communications*, vol. 12, pp. 1021-1024, 2010.
- [115] P. Shearing, R. Bradley, J. Gelb, F. Tariq, P. Withers and N. Brandon, "Exploring microstructural changes associated with oxidation in Ni-YSZ SOFC electrodes using high-resolution X-ray computed tomography," *Solid State Ionics*, vol. 216, pp. 69-72, 2012.
- [116] Y. Chen-Wiegart, J. Cronin, Q. Yuan, K. Yakal-Kremiski, S. Barnett and J. Wang, "3D Non-destructive morphological analysis of a solid oxide fuel cell anode

- using full-field X-ray nano-tomography," *Journal of Power Sources*, vol. 218, pp. 348-351, 2012.
- [117] J. Laurencin, R. Quey, G. Delette, H. Suhonen, P. Cloetens and P. Bleuet, "Characterization of Solid Oxide Fuel Cell Ni-8YSZ substrate by synchrotron X-ray nano-tomography: from 3D reconstruction to microstructure quantification," *Journal of Power Sources*, vol. 198, pp. 182-189, 2012.
- [118] P. Shearing, R. Bradley, J. Gelb, S. Lee, A. Atkinson, P. Withers and N. Brandon, "Using Synchrotron X-Ray Nano-CT to Characterize SOFC Electrode Microstructures in Three-Dimensions at Operating Temperature," *Electrochemical and Solid State Letters*, vol. 14, pp. B117-B120, 2011.
- [119] Q.-A. Huang, R. Hui, B. Wang and J. Zhang, "A reveiw of AC impedance modeling and validation in SOFC diagnosis," *Electrochimica Acta*, vol. 52, pp. 8144-8164, 2007.
- [120] A. Weiss, S. Schindler, S. Galbiati, M. Danzer and R. Zeis, "Distribution of Relaxation Times Analysis of High-Temperature PEM Fuel Cell Impedance Spectra," *Electrochimica Acta*, vol. 230, pp. 391-398, 2017.
- [121] Y. Zhang, Y. Chen and F. Chen, "In-situ quantification of solid oxide fuel cell electrode microstructure by electrochemical impedance spectroscopy," *Journal of Power Sources*, vol. 277, pp. 277-285, 2015.
- [122] H. Schichlein, A. Muller, M. Voigts, A. Krugel and E. Ivers-Tiffée, "Deconvolution of electrochemical impedance spectra for identification of electrode reaction mechanisms in solid oxide fuel cells," *Journal of Applied Electrochemistry*, vol. 32, pp. 875-882, 2002.



ISBN 978-952-60-3799-8 (printed)
ISBN 978-952-60-3800-1 (pdf)
ISSN 1799-4934 (printed)
ISSN 1799-4942 (pdf)

Aalto University
School of Science
Department of Applied Physics
www.aalto.fi

**BUSINESS +
ECONOMY**

**ART +
DESIGN +
ARCHITECTURE**

**SCIENCE +
TECHNOLOGY**

CROSSOVER

**DOCTORAL
DISSERTATIONS**